Alma Mater Studiorum – Università di Bologna

School of Science

Department of Industrial Chemistry "Toso Montanari"

Corso di Laurea Magistrale / Master

Advanced Spectroscopy in Chemistry

Classe LM-71 - Scienze e Tecnologia della Chimica Industriale

Outdoor bronze conservation: assessment of protective treatments by accelerated aging and of treatment removal procedures by laser cleaning

Experimental Master Thesis

CANDIDATE

Marie Cordier

TUTOR

Chiar.mo Prof. Carla Martini

CO-TUTORS

Dott.ssa Elena Bernardi

Dott. Iuri Boromei

Dott.ssa Cristina Chiavari

Dott.ssa Benina Lenza

First Session

Academic Year 2012-2013

Contents

Aim and background

Outdoor bronzes exposed to the environment form naturally a layer called patina, which may be able to protect the metallic substrate. However, since the last century, with the appearance of acid rains, a strong change in the nature and properties of the copper based patinas occurred [1]. Studies and general observations have established that bronze corrosion patinas created by acid rain are not only disfiguring in terms of loss of detail and homogeneity, but are also unstable [2]. The unstable patina is partially leached away by rainwater. This leaching is represented by green streaking on bronze monuments [3]. Because of the instability of the patina, conservation techniques are usually required.

On a bronze object exposed to the outdoor environment, there are different actions of the rainfall and other atmospheric agents as a function of the monument shape. In fact, we recognize sheltered and unsheltered areas as regards exposure to rainwater [4]. As a consequence of these different actions, two main patina types are formed on monuments exposed to the outdoor environment. These patinas have different electrochemical, morphological and compositional characteristics [1]. In the case of sheltered areas, the patina contains mainly copper products, stratified above a layer strongly enriched in insoluble Sn oxides, located at the interface with the uncorroded metal. Moreover, different colors of the patina result from the exposure geometry. The surface color may be pale green for unsheltered areas, and green and mat black for sheltered areas [4]. Thus, in real outdoor bronze monuments, the corrosion behavior is strongly influenced by the exposure geometry. This must be taken into account when designing conservation procedures, since the patina is in most cases the support on which corrosion inhibitors are applied.

Presently, for protecting outdoor bronzes against atmospheric corrosion, inhibitors and protective treatments are used. BTA and its derivatives, which are the most common inhibitors used for copper and its alloy, were found to be toxic for the environment and human health [5, 6]. Moreover, it has been demonstrated that BTA is efficient when applied on bare copper but not as efficient when applied on bare bronze [7]. Thus it was necessary to find alternative compounds. Silane-based inhibitors (already successfully tested on copper and other metallic substrates [8]), were taken into consideration as a non-toxic, environmentally friendly alternative to BTA derivatives for bronze protection.

The purpose of this thesis was based on the assessment of the efficiency of a selected compound, to protect the bronze against corrosion, which is the 3-mercapto-propyl-trimethoxy-silane (PropS-SH). It was selected thanks to the collaboration with the Corrosion Studies Centre "Aldo Daccò" at the Università di Ferrara. Since previous studies [9, 10, 11] demonstrated that the addition of nanoparticles to silane-based inhibitors leads to an increase of the protective efficiency, we also wanted to evaluate the influence of the addition of CeO_2, La_2O_3, TiO_2 nanoparticles on the protective efficiency of 3-mercapto-propyl-trimethoxy-silane, applied on pre-patinated bronze surfaces. This study is the first section of the thesis.

Since restorers have to work on patinated bronzes and not on bare metal (except for contemporary art), it is important to be able to recreate the patina, under laboratory conditions, either in sheltered or unsheltered conditions to test the coating and to obtain reliable results. Therefore, at the University of Bologna, different devices have been designed to simulate the real outdoor conditions and to create a patina which is representative of real application conditions of inhibitor or protective treatments. In particular, accelerated ageing devices by wet & dry (simulating the action of stagnant rain in sheltered areas [12]) and by dropping (simulating the leaching action of the rain in unsheltered areas [1]) tests were used.

In the present work, we used the dropping test as a method to produce pre-patinated bronze surfaces for the application of a candidate inhibitor as well as for evaluating its protective efficiency on aged bronze (unsheltered areas).

In this thesis, gilded bronzes were also studied. When they are exposed to the outside environment, a corrosion phenomenon appears which is due to the electrochemical couple gold/copper where copper is the anode. In the presence of an electrolyte, this phenomenon results in the formation of corrosion products than will cause a blistering of the gold (or a break-up and loss of the film in some cases). Moreover, because of the diffusion of the copper salts to the surface, aggregates and a greenish film will be formed on the surface of the sample [13].

By coating gilded samples with PropS-SH and PropS-SH containing nano-particles and carrying out accelerated ageing by the dropping test, a discussion is possible on the effectiveness of this coating, either with nano-particles or not, against the corrosion process. This part is the section 2 of this thesis.

Finally, a discussion about laser treatment aiming at the assessment of reversibility/re-applicability of the PropS-SH coating can be found in section 3 of this thesis. Because the protective layer loses its efficiency with time, it is necessary to find a way of removing the silane layer, before applying a new one on the "bare" patina. One request is to minimize the damages that a laser treatment would create on the patina. Therefore, different laser fluences (energy/surface) were applied on the sample surface during the treatment process in order to find the best range of fluence. In particular, we made a characterization of surfaces before and after removal of PropS-SH (applied on a naturally patinated surface, and subsequently aged by natural exposure) with laser methods. The laser removal treatment was done by the CNR Institute of Applied Physics "Nello Carrara" of Sesto Fiorentino in Florence.

In all the three sections of the thesis, a range of non-destructive spectroscopic methods (Scanning Electron Microscopy with Energy Dispersive Spectroscopy (SEM-EDS), µ-Raman spectroscopy, X-Ray diffractometry (XRD)) were used for characterizing the corroded surfaces. AAS (Atomic Absorption Spectroscopy) was used to analyze the ageing solutions from the dropping test in sections 1 and 2.

Introduction

1.1. Bronze foundry alloys

1.1.1. Composition

Bronze is a metal used for several applications, among which ornamental purposes. It is an alloy of copper which can have completely different compositions depending on the physical characteristics that we want to obtain. Compared to copper, bronze is a harder material thus it can be used when a higher strength and corrosion resistance than copper is required. Moreover, the weathering characteristics of bronze are related to its variation in proportion and elemental composition [14].

Different variations of these two parameters give rise to different kinds of bronze. For example, "true" bronze is composed of approximately 90% of copper (Cu) and 10% of tin (Sn). Moreover, three main classes or types of bronze exist [14]:

- Statuary bronze: it is composed of approximately 97% of Cu, 2% of Sn and 1% of Zn. It is the closest to the "true" bronze

- Architectural bronze: it is composed of approximately 57% of Cu, 40% of Zn and 3% of Pb. It is closer to the "leaded brass"

- Commercial bronze: it is composed of approximately 90% of Cu and 10% of Zn

These types of bronze are used in sculpture and construction. More precisely, statuary bronzes are typically used in outdoor sculptures that can take multiples forms such as human or animal figures and landscapes. On the other hand, architectural bronzes are typically used for door and window frames, door and window hardware, mail boxes, chutes, rails, ecc [14].

Copper forms alloys with a wide range of alloying elements. The best known traditional types of copper alloys are bronzes, where tin is a significant addition, and brass where zinc is used instead of tin.

Moreover, contemporary bronzes are copper alloys that contain elements such as silicon (Si), manganese (Mn), aluminium (Al), zinc (Zn) and which can contain or not tin (Sn).

The color of bare bronze is pinkish salmon. However, due to patination or corrosion processes, this color is barely seen. In fact, when bronze is exposed to the environment, these processes induce changes on the surface color that finally exhibits a color in the range from lime green to dark brown. These changes can be due to factors as the environment, the exposure geometry of the bronze, the type of protective treatment or the degree of pollution [4].

However, in the case of architectural applications, one trend is to keep the natural pinkish color of the bare bronze compared to the color of the patinated surfaces of outdoor sculptures. For that, polishing and oiling steps can be achieved on the architectural bronzes or their protection by the application of clear lacquers can be considered [14].

1.1.2.   Properties

Bronze is mainly composed of copper. When an excellent electrical conductivity is required for copper, alloying is avoided [14]. However, since copper is extremely difficult to cast, it is alloyed with other elements to improve its castability. The following elements give different properties to copper [15]:

- **Tin:** The oldest known alloying element in copper and the key alloying element in many bronzes. It is a solid-solution strengthener in copper, improves corrosion resistance, reduces the melting temperature of copper and increases the fluidity, making the alloy easier to melt and cast.

- **Zinc:** Imparts strength and hardness. This is the major alloying element for brasses.

- **Lead:** An element which is insoluble in copper. Because it solidifies last, is found at the grain boundaries or interdendritic areas. It is used to help to seal the shrinkage cavities formed toward the end of solidification of the alloy (i.e. it improves hot tearing resistance [16]). It also improves machinability.

- **Aluminium:** Improves the strength and fluidity of copper alloys, but its solubility in copper is limited.

- **Silicon:** Provides excellent fluidity to copper alloys, enabling them to be used for art and mold castings.

- **Nickel:** Provides resistance to corrosion and improves the quality, strength and creep resistance of tin bronzes.

- **Beryllium:** Increases strength by forming an interdendritic precipitate without compromising the electrical and thermal conductivity.

- **Chromium:** Increases strength with a minor loss in electrical conductivity.

- **Iron:** An element not soluble in copper. It increases the melting temperature of copper alloys.

Having excessive iron content in bronze can cause segregation and hard spots. In tin bronzes, iron increases strength and hardness but reduces ductility. Moreover, tin and

zinc increase hardness and breaking strength, while lead improves machinability and castability. However, alloying modifies the oxidation rate of copper, generally slowing it in the case of tin addition, and speeding up oxidation in the case of nickel addition [2].

1.1.3.   Microstructure

Metals can be manipulated by two manufacturing methods that are casting and working. These methods can be done in different ways that lead to different types of metal microstructure [17].

- **Casting:**

There are different types of microstructures that can be developed during the casting and cooling of a melt in a mold.

In the case of ancient metals, the metals are impure or the alloys are composed of two or more metals (for example bronze). The purity of the metal is correlated to the kind of crystal growth that will be generated. Due to their impurity, the majority of ancient castings show a dendritic structure.

Dendrites look like tiny fern leaves. They have the appearance of growths, scattered randomly throughout the metal, that grow larger until they meet each other [17].
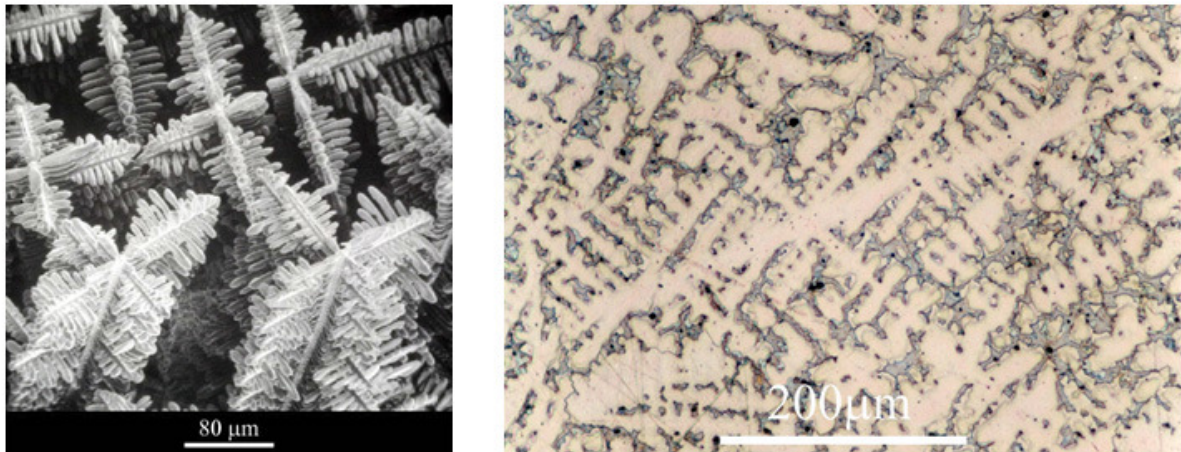
Figure 1: examples of dendrites [18]

The size of dendrites depends on the cooling rate of the metal: the higher the cooling rate, the smaller the dendrites. In the case of slow cooling, instead, the dendrites can sometimes be seen at naked eye or under a binocular bench microscope at low magnification (x10 or x20).

Dendrites are composed of different type of arms:
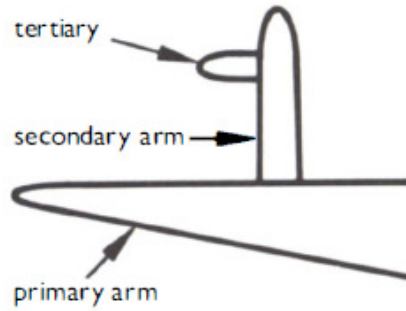
Figure 2: description of dendritic arms [17]

By measuring the space between these arms, it could be possible to find the mold or conditions used for casting the metal [17].

The dendritic growth is one of the phenomena that can appear during the casting. Usually, dendritic growth in bronzes goes together with coring, or micro-segregation, which is due to non-equilibrium solidification (i.e. cooling rate higher than equilibrium cooling rate, which should be infinitely slow) (figure 3a). If cooling is too fast, then there is not time enough for diffusion, resulting in chemical heterogeneities in the growing dendrites (i.e. the core of the dendrite, which formed first, has a different chemical composition to the outer area, which formed last). Because copper has the higher melting point, the first part of the dendrite arms which is formed is richer in copper since it solidifies first. Then the outer parts of the arms are richer in tin. It results in a compositional gradient from the inner region of a dendritic arm to the outer surface (figure 3b) [17].
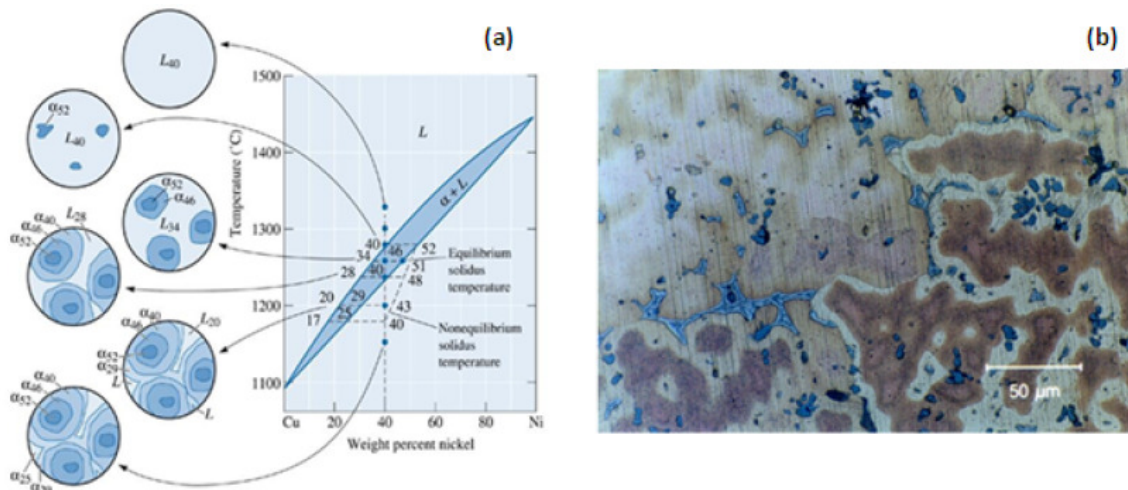
Figure 3: (a) scheme of the development of cored microstructure due to non-equilibrium solidification; (b) example of cored dendritic microstructure in bronze alloys: The Cu-rich core of dendrites is brown whilst the Sn-rich peripheral region is whitish. [19]

Pure copper can sometimes be free of impurities and, if a slow cooling is applied, no dendrites are visible and the cooling produces an equi-axial, hexagonal grain structure (figure 4, on the left). It represents an ideal model of a metallic crystal where all the grains have approximately the same size, are randomly oriented and are roughly

hexagonal in section. It is an equilibrium structure, thus having the lowest energy requirement, while the dendritic structure is a non-equilibrium one (figure 4, on the right).
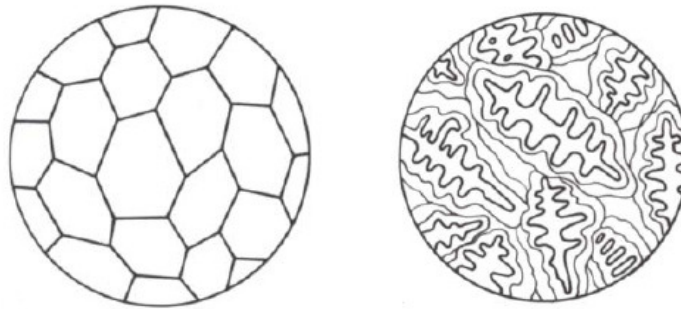
Figure 4: ideal model of a metallic crystal (left) and a dendritic structure in an alloy (right) [17]

Moreover, in cast metals, characteristic spherical holes or porosity can occur. They can be due to dissolved gases in the melt or to interdendritic holes and channels that have not been kept filled with metal during solidification. During the cooling of the metal, the dissolved gases can exsolve. This phenomenon creates reactions with the metal itself and induces the formation of oxides such as cuprous oxide (Cu_2O) or can cause gas porosity in the metal [17].

- **Working:**

This technique consists in changing the shape of a metal or an alloy by using various techniques such as hammering, turning, raising, drawing etc.

The action of hammering can deform the grains of the structure which become flattened until they are too brittle to work any further (the grains are fully work-hardened). If it is necessary to shape or hammer the metal again, its annealing (around 500-800°C for copper alloys) is needed in first place for restoring its ductility and malleability. These steps can be repeated until the final shape of the metal is achieved.

The working, and all the thermal and mechanical treatments that are induced, modifies the microstructure of bronze. Figure 5 illustrates the main modifications.

7
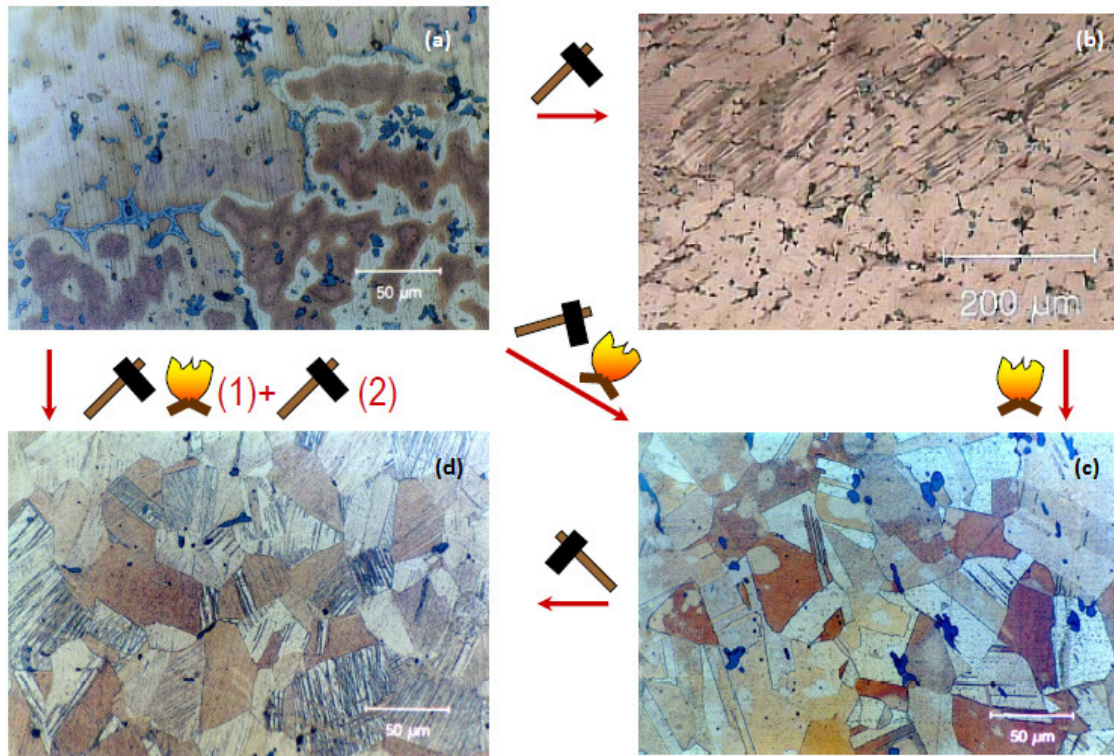
Figure 5: Micro-structural modifications induced by thermal/mechanical treatments in the bronze microstructure: As-cast dendritic structure (a), deformed dendrites with slip bands (after cold working) (b), recrystallised microstructure (after annealing) (c), recrystallised microstructure with slip bands (after annealing followed by cold working) (d). [20]

The annealing does not completely remove the segregation that occurs during the casting operation [17]. Moreover, segregation is not the only phenomenon that affects the microstructure of bronze or alloys. In fact, the presence of multiple phases has an influence on mechanical and chemical properties.

A phase is any homogeneous state of a substance that has a definite composition. In the case of ancient metals, this term is not totally true because the systems are not completely in equilibrium conditions. It means that the composition of a given alloy, and thus the proportion of each element, will not match perfectly with the values coming from the phase diagram of this alloy.

The phase diagram is a "map" that can be used to predict which phases will be present in the alloy at equilibrium. Because of the fact that these diagrams are acquired with very slowly cooled melts, they do not perfectly fit with archaeological materials for which the cooling is usually faster. Thus the phase diagrams have to be interpreted with caution in these cases.

When two (or more) metals are mixed together to form an alloy there are different possibilities regarding their mutual solubility [17]:

- Complete solid solubility of the metals (e.g. Au-Ag). In that case, the phase diagram shows only one solid phase (solid solution) present at all temperatures up to the solidus line. With the increase of the temperature, the solid alloy passes through a pasty, semisolid region in which some liquid is present in equilibrium with some solid and, finally, the entire alloy becomes a liquid melt (figure 6). During the cooling, the alloy undergoes the following transitions:

$$L \rightarrow L + \alpha \rightarrow \alpha \text{ (where L= liquid and } \alpha \text{ = solid)}$$
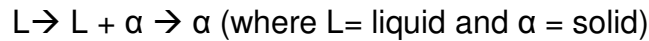
If no segregation is present, then the microstructure will be a group of equi-axial, hexagonal grains of uniform composition.
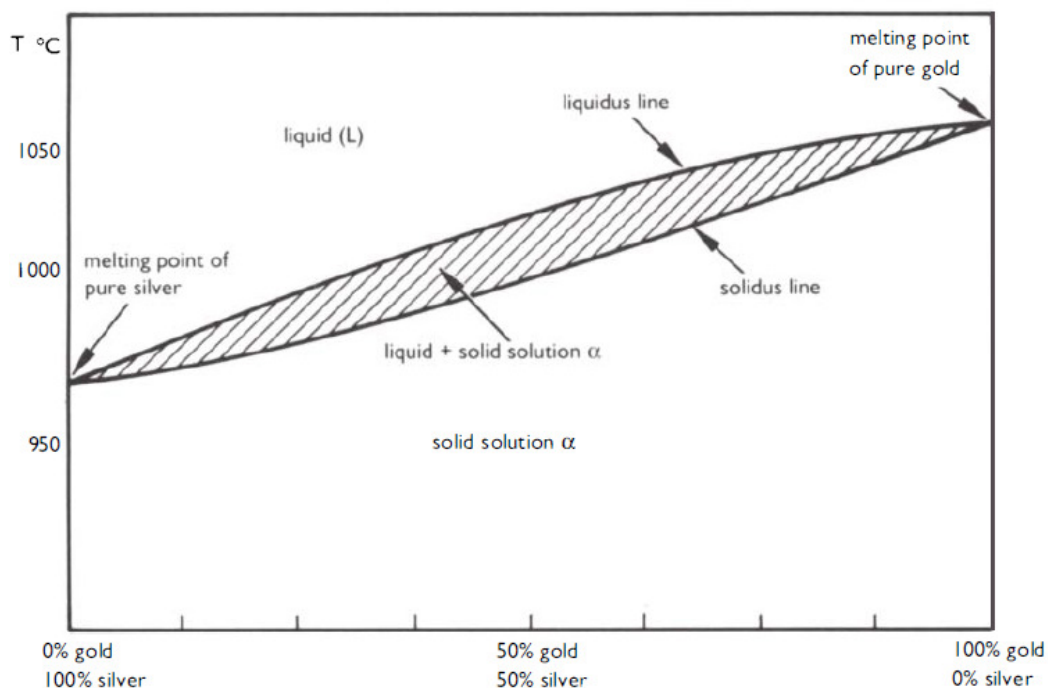
Figure 6: phase diagram of the binary Au-Ag alloy [17]

- Solid can show only partial solubility of the metals in each other. For example, it is the case of silver and copper. Three phase diagrams result from this situation: the eutectic type (the most common), the eutectoid type and the peritectoid type.

- Metals are completely immiscible in each other.

The eutectic point corresponds to the lowest temperature at which the liquid melt can directly pass to solid. It is not the same depending on the nature of the alloying constituents. Figure 7 shows the eutectic phase diagram of silver-copper alloy:
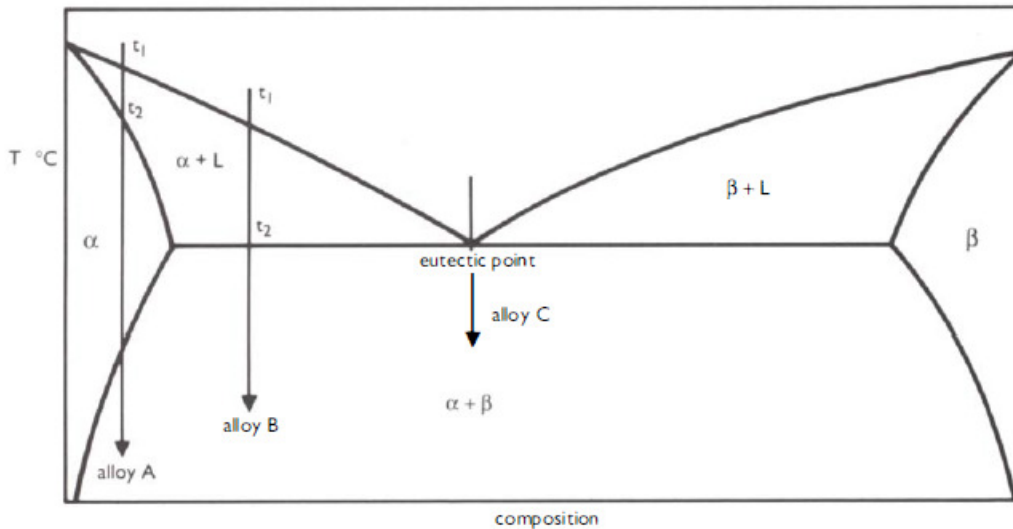
Figure 7: eutectic phase diagram of silver-copper alloy [17]

At this point, which corresponds to a particular composition and temperature, the liquid melt solidifies. The corresponding transitions (for example in the case of an alloy B (see figure 7)) are:

$$L\ (t_1) \rightarrow L\ (t_2) + \alpha$$

$$L\ (t_2) \rightarrow \alpha \rightarrow (\alpha + \beta)$$
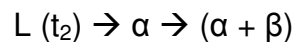
Where t = temperature

We talk about hypo-eutectic region when the composition is before the eutectic point whereas we talk about hyper-eutectic region when the composition is after the eutectic point. In that case, both alloy A and alloy B are in the hypo-eutectic region.

In this region, the final solid structure for the hypo-eutectic alloy is composed of α + (α + β). Thus the solid is a two-phased solid containing plates of primary alpha (in the shape of grains or dendrites) in a eutectic matrix (alpha and beta phases interspersed in each other (figure 8)).
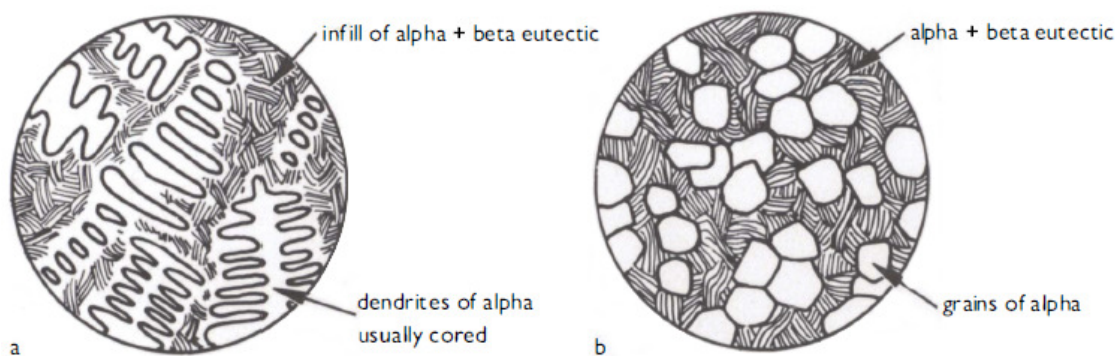
Figure 8: eutectic type microstructures (a,b) [17]

The original alpha phase is present as dendrites (figure 8: a) or as hexagonal grains (figure 8: b) depending on the cooling rate. Usually, in the case of archaeological materials, the primary alpha is dendritic and cored.

The eutectoid structure is similar to the eutectic one except that the eutectoid reaction occurs when an already existing solid solution transforms into two distinct phases. The phase diagrams corresponding to this structure are more complex because they describe series of changes in the solid as the temperature decreases. One example of eutectoid phase diagram is the tin-bronze phase diagram (figure 9):
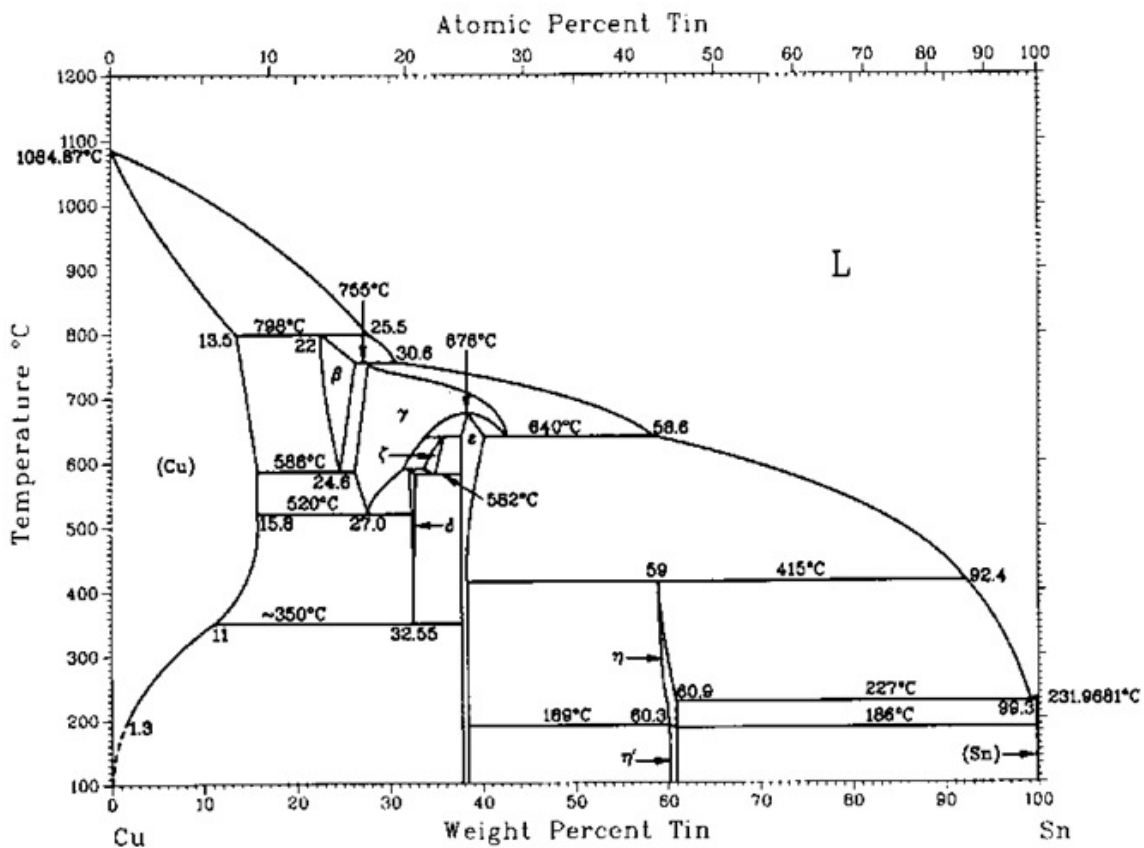
Figure 9: Cu-Sn phase diagram [20]

Tin bronzes can be divided into two regions depending on the composition of tin in the bronze: low-tin bronze and high-tin bronze. Low-tin bronze contains less than 15.8 wt% of tin which corresponds to the solvus line where the solubility limit is function of the temperature. The higher the rate of solidification, the lower the solubility of Sn in Cu. Figure 10 represents the displacement of the solvus line depending on the conditions used. The solvus line corresponds to the highest tin content in the case of the equilibrium because it corresponds to a slow cooling rate.
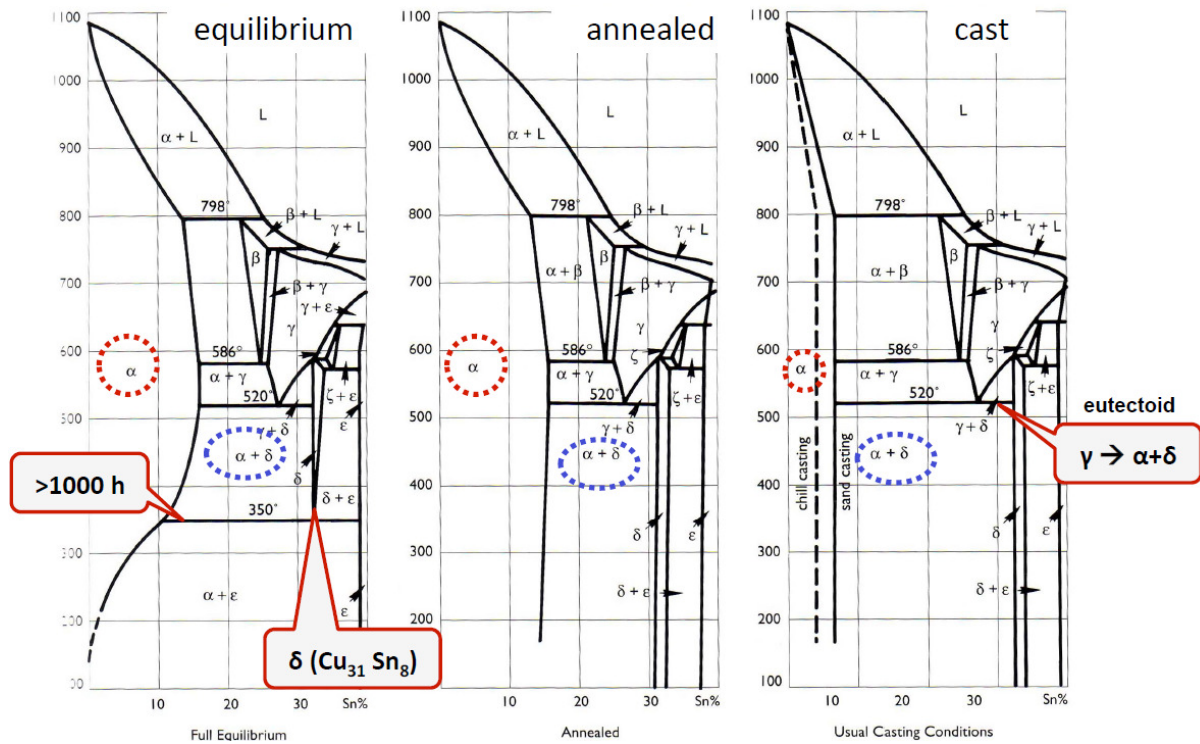
Figure 10: Cu-Sn phase diagram at equilibrium and under annealing and casting conditions [17]

One difference between those three phase diagrams is that the α + ε eutectoid is not present anymore in the annealing and casting cases. It is due to the fact that a very slow solidification rate has to be applied on the alloy to obtain this phase. Thus only the equilibrium case can permit it.

Above the solidification line, the α + δ microstructural constituent corresponds to the eutectoid morphology (figure 11).

cored alpha dendrites

light blue eutectoid where delta phase has the composition $Cu_{31}Sn_8$ (α + δ)
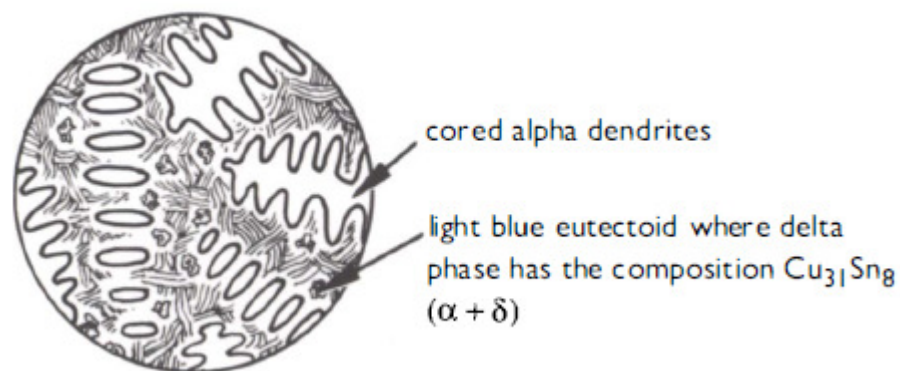
Figure 11: α and δ eutectoid in a tin-bronze alloy [17]

The α phase is the copper-rich solid solution of tin in copper whereas the δ phase is an intermetallic compound of fixed composition ($Cu_{31}Sn_8$). This phase is a light blue, hard and brittle material with a jagged appearance.

When studying a two-phase alloy like tin-bronze, two important parameters have to be considered:

12

- There is microsegregation because of the fact that different compositions are localized at different place into the microstructure

- The corrosion process is not the same depending on the kind of alloy (one phase or two phases)

1.2. Atmospheric corrosion of bronze

1.2.1. Bronze corrosion products

When a bronze is exposed to the outdoor environment, corrosion processes act on it and form the *patina* which is a layer containing several constituents.

A patina, which has developed over years, contains a number of compounds that together provide the overall appearance. This includes corrosion products and deposited material such as aerosol particles, windblown dust and soot [21].

The corrodibility of the metal surface in any environment depends upon multiple factors including the type of environment, alloy composition, manufacture and exposure conditions [2]. The effects of the exposure are less aggressive on the patina than on bare bronze.

The corrosion processes can induce drastic changes in the color of the surface and not be pleasant from an aesthetical point of view. However, the patina helps in maintaining the original appearance of the bronze surface and permits to have a change of it that occurs more slowly [14].

Depending on its chemical composition, the patina of the bronze can have a specific type of color from the "pale" green to the "mat" black [4]. This specific type of colour can be linked to a specific type of corroded surfaces. Robbiola et al [4] demonstrated that the distribution and size on the bronze outdoor of these specific corroded surfaces are in relation with the exposure to rainwater. In fact, they recognized pale green or black surfaces which were exposed to rainfall. They correspond to compounds with high tin element content. They also recognized green or mat black surfaces which were not directly submitted to the washing effect of rain. They correspond to compounds essentially made of copper corrosion products. As indicated above, other important factors influencing the corrosion process are surface inclination and environmental characteristics.

An inclined surface (face to the sun), and thus exposed to precipitation, will suffer more the variation of temperature than a vertical or downward face sample. The first one will be thus more accessible to corrodants from precipitation and from coarse particles. In that case, if a stagnation phenomenon occurs, the humidity is trapped and retained in the patina and leads to a green patina formation. On the other hand, vertical or

downward surface exhibits lower deposition rates which seem to favor cuprite formation and thus a brownish color [22].

Regarding the chemical composition of the patina, some phases are commonly found [3]:

- **Cuprite [Cu_2O]:** Insoluble in water and slightly soluble in acid.

- **Brochantite [$Cu_4(SO_4)(OH)_6$]:** Nearly always the most common component of the green patina formed after long atmospheric exposure.

- **Antlerite [$Cu_3(SO_4)(OH)_4$]:** Not uncommon as a patina constituent. It is stable in more acidic conditions than brochantite. This phase was found on the copper skin of the Statue of Liberty, and it is suggested that acid rain converts brochantite to less protective antlerite, which is more susceptible to erosion.

- **Posnjakite [$Cu_4(SO_4)(OH)_6 \cdot H_2O$]:** Just an hydrated form of brochantite. It may co-exist or undergo transformation to brochantite (figure 12).

- **Atacamite [$Cu_2Cl(OH)_3$]:** Soluble in weak acid. It has been found to be as abundant or more abundant than brochantite in patinas formed near the sea. Not found on specimens exposed for short times.

- **Paratacamite [$Cu_2Cl(OH)_3$]:** Its presence is transitory and it eventually converts to atacamite. Not found on specimens exposed for long times.

- **Atmospheric particles:** Alumina, iron oxide, silica and other components typical of wind-blown dust are frequently noted, as is soot.

- **Malachite [$Cu_2(CO_3)(OH)_2$]:** Atmosphere does not favour the formation of this carbonate, but it is sometimes unexpectedly found in practice.

- **Gerhardtite [$Cu_2NO_3(OH)_3$]:** Found just in some locations.

Some of these phases are quite similar and are connected in the sense that ones are precursors of the others [23].

Thus patinas are chemically and structurally complex. Moreover, the process of formation of patina includes repeated dissolution and precipitation, processes which are triggered by strongly varying humidity conditions resulting in a gradual accumulation of less-soluble corrosion products in the patina, whereas more easily dissolved compounds (like those of zinc) are washed away [24].

As a result, the patina will be more and more corrosion resistant and the corrosion rate is expected to gradually decrease with exposure time.

Chiavari et al. [25] reported that for outdoor bronzes which are exposed to rain events, if the surface is under stagnant rain conditions then the patina acts as a multilayer system

where a Sn-enriched layer is covered by Cu and Pb compounds and Zn dissolves completely. On the other hand, in the case of runoff conditions, the patina is a thin porous layer strongly enriched in insoluble Sn oxides across which Cu, Zn and Pb cations migrate and most of them are leached into the environment.

Figure 12 represents a scheme of bronze patina evolution proposed by Krätschmer et al. [23]. This scheme illustrates the evolution of the components of a sheltered copper patina over time and in different dominated environments (sulfate or chloride-dominated).
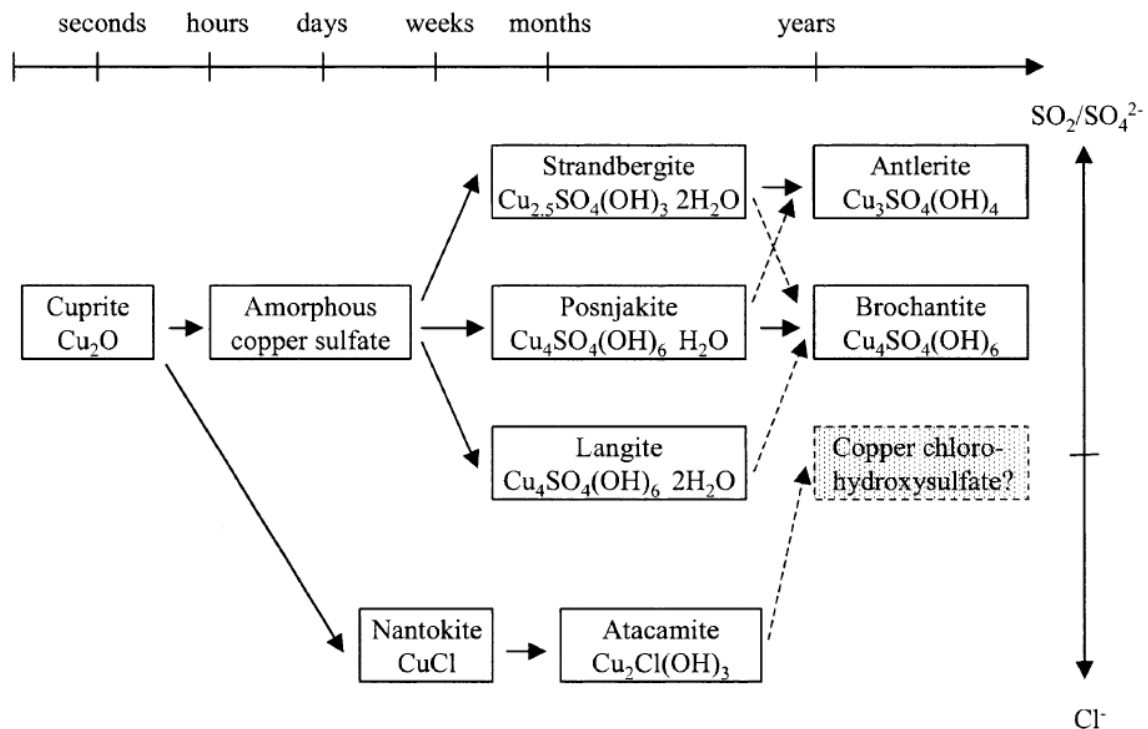
Figure 12: scheme describing the evolution of the patina, in sheltered exposure geometry of bronze, over time and different environments (sulphate or chloride dominated environments) [23]

Figure 12 shows that cuprite is the first compound formed on the patina. It appears quite instantaneously and it is followed by the formation of copper hydroxysulfates which result from amorphous copper sulfate. When copper is in an acid environment (high SO_2/SO_4^{2-} concentration), this amorphous phase transforms into strandbergite while posnjakite and langite tend to form in a less acidic environment. These compounds form in a restricted period of time (months). Years are needed if we want these precursors to transform into brochantite or antlerite. Moreover, for obtaining atacamite, a Cl^- rich environment is necessary, preceded by the formation of nantokite.

Concerning patina of unsheltered areas, Figure 13 describes the corrosion mechanism and the mass variation of the alloying elements of bronze about this specific case.
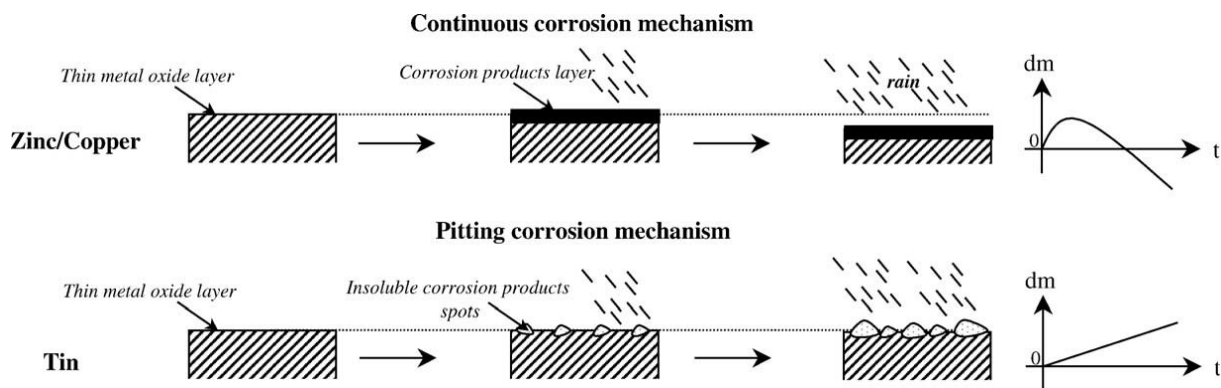
Figure 13: scheme of the mass variation (dm) of zinc, copper and tin during exposure under unsheltered conditions [26]

The corrosion behaviour of copper and zinc appears relatively similar in the unsheltered exposure [26]. We can observe a mass increase coming from the formation of a corrosion layer on the surface of the substrate. It is followed by a decreasing mass variation, which is explained by the continuous dissolution of the corrosion products because of the rain-water. Mass variations become negative after a few months [26]. The mass increase at the beginning of exposure can be explained by a difference in the rate of the formation of corrosion products and the rate of dissolution of these products: in this step, the formation of corrosion products is faster than their dissolution. After few weeks the contrary occurs resulting in a mass loss.

On the surface of copper sample, after few days of exposure, a cuprite Cu_2O layer can be identified which will be covered by a mixture of the basic copper sulphates $Cu_4SO_4(OH)_6.H_2O$ with $Cu_4SO_4(OH)_6$. With time, the proportion of hydrated form will diminish whereas the non-hydrated one will increase [26].

Concerning zinc substrate, basic zinc carbonates $Zn_5(OH)_3(CO_3)_2$ and $Zn_4CO_3(OH)_6.H_2O$ and basic zinc sulphates $Zn_4SO_4(OH)_6.xH_2O$ (especially x=5) are the main corrosion products over the surface. However, the corrosion layers formed on the zinc surface are thin because of the rainfalls that induce washing and dissolution process [26].

In the case of tin, the mass variation increases continuously throughout the exposure time. This increase is due to a localised corrosion mechanism and the growth of insoluble clusters of corrosion products on the surface. These corrosion products are a complex mixture where hydrated stannic oxide $SnO_2.xH_2O$ (not well crystallized) is the main constituent. Other forms of Sn(IV) and Sn(II) such as sulfate, carbonate and chlorides phases were detected in small amounts [26].

In general, the formation of the patina can be described in five steps [14]:

(1) **Induction**: Oxidation takes place and produces the dark brown copper oxide film, which can act as a protective barrier against future pollutants. The composition of this film depends on the type and concentration of pollutants in the atmosphere,

16

time of exposure and the relative degree and duration of wetness on the surface. This step can be dramatically affected by high concentrations of pollutants in the atmosphere which could produce a less protective or, even worst, a potentially damaging film.

Metallic copper oxidizes according to the following reaction [3]:

$$2\ Cu + \tfrac{1}{2}\ O_2 \rightarrow Cu_2O$$
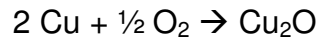
Pb exposed to the atmosphere has been reported to primarily form litharge (PbO), while Sn forms cassiterite (SnO_2) or, more probably, an amorphous hydrated oxide ($SnO_2 \cdot xH_2O$) [27].

(2) **Conversion to copper sulphate (sulphurization)**: it normally starts to occur in horizontal surfaces because they are the ones with more exposure to moisture (rain, water run-off) and deposition of particles, creating a situation where electrolytic reactions occur.

Copper ions from the cuprite are oxidized from Cu^+ to Cu^{2+} in the presence of a layer of surface water via the two partial reactions:

$$Cu^+ \rightarrow Cu^{2+} + e^-$$

$$\tfrac{1}{2}\ O_2 + H_2O + 2e^- \rightarrow 2\ OH^-$$
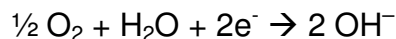
Atmospheric SO_2 is oxidised to sulphate by the reaction:

$$SO_2 + H_2O + \tfrac{1}{2}\ O_2 \rightarrow H_2SO_4$$
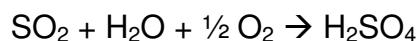
And then Cu^{2+} reacts slowly to form basic salts according to:

$$Cu_2O + SO_4^{2-} + H_2O \rightarrow Cu_x(SO_4)(OH)_y \cdot nH_2O \text{ (posnjakite, brochantite or antlerite)}$$

$$Cu_2O + Cl^- + H_2O \rightarrow Cu_2Cl(OH)_3 \text{ (paratacamite or atacamite)}$$
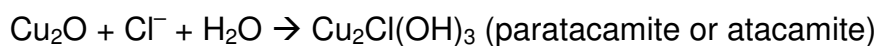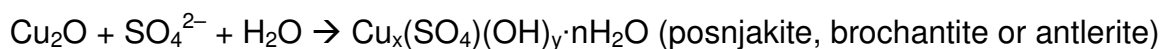
On the more exposed areas, some thin and light green patches can be observed due to the formation of brochantite (if SO_2 is present) or atacamite/paratacamite (if Cl^- is present).

PbO is known to react rapidly with SO_2 and HSO_4^-(aq) forming insoluble sulphite ($PbSO_3$) and sulphate ($PbSO_4$), respectively. Anglesite ($PbSO_4$) tends to form a protective layer. Other lead species like lanarkite (Pb_2SO_4O), PbO and minium (Pb_3O_4) have been detected [27].

SnO_2 and $SnO_2 \cdot xH_2O$ have acidic character and react slowly or not at all with SO_2 and HSO_4^-(aq). An amorphous gel of the hydrated oxide has been suggested to form on bronzes exposed in outdoor environments [27].

As for Zn, it has been reported that it reacts with SO_2 to form $ZnSO_3$, which is subsequently oxidised to soluble $ZnSO_4$ [27].

(3) **Run-off streaking and scab formation**: This step occurs at a lower rate than step 1 and step 2 but it is important in terms of consequences. Even if copper sulphates and sulphides were formed in previous stages, their degree of solubility may vary widely. In this step occurs the streaking and discoloration of the patina, which are due to differential weathering of the corrosion by-products. This step can continue until blackish areas or island like scabs are present on the surface.

Moreover, staining of the base of bronze statues can be assimilated to the loss of brochantite during runoff [3].

Figure 14 shows a monument of the French king Louis XIV in the entrance yard of the Palace of Versailles. We can observe the green streaking and discoloration of patina, which leads to commonly observed staining of the bronze statues [28].

Figure 14: green streaking and discoloration phenomenon on the statue of Louis XIV. The picture on the right shows the presence of blackish areas and island [28]

(4) **Pitting**: it is generally caused by microscopic particles of chlorides deposited from the air and coming from saline soils or salt spray near to bodies of salt water. This phenomenon can spread around the black scab formation and

spread below protective coating, patina or what appears to be a stable surface. The chlorine reacts with the copper in bronze to form copper chlorides. If the chloride concentration is very high, brochantite can react with chloride ions [3].

Copper chloride is relatively unstable and allows the corrosion of the bronze. Thus it is important to remove it by conservation techniques (which sometimes employ electrochemical methods) to avoid this continuing corrosion of the bronze.

(5) **Conversion to blue-green copper sulphate**: it is the final step of the corrosion where all exposed surfaces form a lime-green colour and matte texture, which is the familiar solid green bronze. At this step, the phase is a phase of active corrosion.

1.2.2.   Bronze corrosion morphologies

Different types of corrosion can appear on the metal surface. In this thesis, the intergranular corrosion and pitting were observed on cross-sections (section 1).

The intergranular corrosion is a localized attack along the grain boundaries (which separate the grains of the microstructure of metals or alloys) or immediately adjacent to grain boundaries, while the bulk of the grains remains largely unaffected. This form of corrosion is usually associated with high energy content.

The pitting corrosion is a localized form of corrosion by which cavities or "holes" are produced in the material. The pitting is considered to be more dangerous than uniform corrosion damage because it is more difficult to detect, predict and design against. Corrosion products often cover the pits. A small, narrow pit with minimal overall metal loss can lead to the failure of an entire engineering system. The pitting corrosion, which, for example, is almost a common denominator of all types of localized corrosion attack, may assume different shapes:
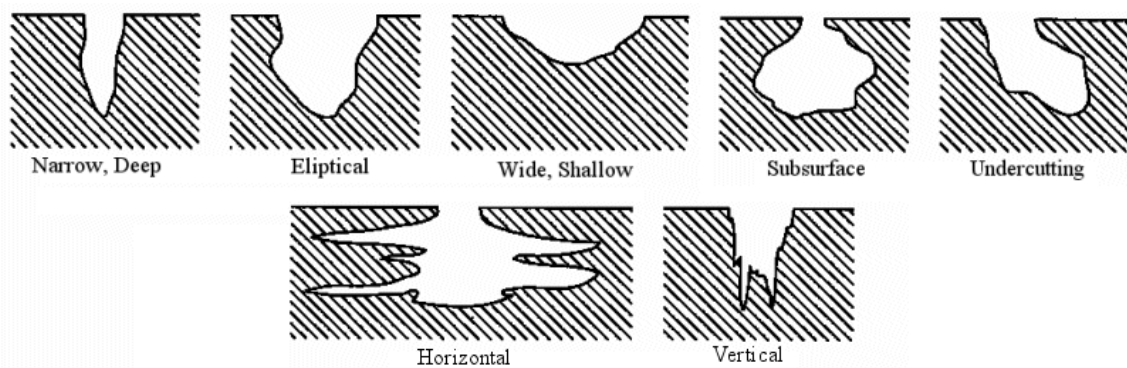
Figure 15: Different shapes of pitting corrosion [29]

1.3. Gilded bronzes

1.3.1. Gilded bronze corrosion

In the case of gilded bronzes, galvanic corrosion occurs.

Galvanic corrosion refers to corrosion damage induced when two dissimilar materials (or in some cases, the same metal) are coupled in an electrolyte. The electrolyte is most likely condensed moisture containing soluble salt impurities [13].

This kind of corrosion is due to an electrochemical potential difference. Galvanic corrosion happens if there is an anode (negatively charged area), a cathode (positively charged area) and an electrolyte (conducting medium such as rainwater, condensation, acid, alkali or a salt). The formation of an anode and a cathode can be due to the presence of impurities, difference in work hardening or local differences of oxygen concentration on the surface [14].

The gold-bronze system is one example of galvanic couple between the two different metals. In that case, copper is the anode whereas gold is the cathode. Thus copper is the metal which is the less stable one. The National Bureau of Standards (NBS) created a galvanic series to show the susceptibility of various metals to be corroded or, in other words, the different nobility.

In this series, metals were ranked from least (1) to most corrosive (12) [14].

1. Gold

2. Graphite

3. Silver

4. Stainless steels

5. Bronze, copper, brass

6. Tin

7. Lead

8. Lead-tin solders

9. Cast iron, ordinary steel

10. Aluminum

11. Zinc

12. Magnesium

Metals from 1 to 5 are noble metals whereas metals from 6 to 12 are ignoble or base metals.

In that list, we can see that gold is above bronze thus that is why, during the galvanic corrosion, bronze is corroded instead of gold.

As above mentioned, outdoor bronzes naturally form different corrosion layers, usually called *patina.* In the case of gilded bronzes, the corrosion is further stimulated by the galvanic coupling copper-gold, which increases the corrosion rate of bronze, being the less noble element of the system. In fact, the golden layer is frequently porous and discontinuous, then permeable to the humid depositions responsible for the growth of corrosion products at the bronze-gold interface.

Copper contained in the bronze starts to oxidate on contact with the gold layer. Moreover, the galvanic process is accelerated if there are conductive substances (such as cupric hydroxyl salts) accumulated at the interface between the two metals [30].

Pitting, due to chlorides, may be the first corrosion action in gilded bronze corrosion. The presence of chlorides and sulfates damages the gilded bronze [30]:

- Chlorides corrode bronze inducing micro-craters in tiny points under the gold layer

- Sulfates evolve from the micro-craters, which become more voluminous. Then blisters are created because of the crystallization pressure of these craters that deform and locally uplift the gold film. This process continues until a micro-fragment of gold detaches itself or is lost

After that, the salts, which were at the interface between the two metals, migrate to the surface where they interact with compounds from atmospheric contamination (first gypsum and then carbonic and silicate particles). It results into their crystallization and the formation of a grey-greenish crust composed of the deposited products.

Figure 16: Corrosion products migrated on the surface of the panel of the Paradise door (Florence) [31]

In Figure 17, which shows a cross-section of a gilded bronze (from the Paradise door in Florence), we can observe the corrosion that can appear on bronze substrates.
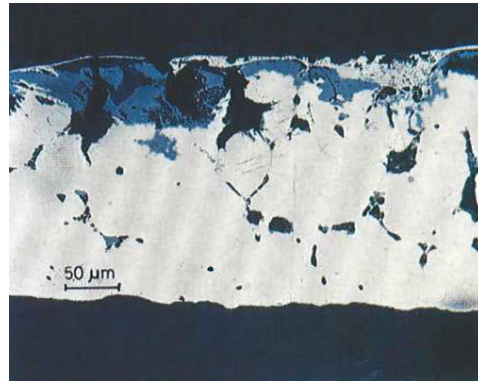
Figure 17: example of the corrosion of a gold-copper alloy (cross-section of a sample from the "Paradise Door" in Florence) [32]

1.3.2. The Paradise Door by Ghiberti

The conservation of gilded bronzes is very important and it is studied since many decades. One example is the Paradise Door on the Baptistery of Florence which was cast by Ghiberti. It is one of the major masterpieces of the Italian metallurgical art of the XIV and XV centuries [33]. This door was cast between 1429 and 1452 and it is composed of 10 panels describing scenes of the Old Testament. Each wing contains five gilded bronze panels that are inserted within a bronze framework cast [30]. The gilding procedure was made using the amalgam or fire-gilding technique.

Figure 18: Paradise Door in Florence [34]

1.3.3.   Gilding methods

The gilding of metals is used since the third millennium B.C. Through ages, different methods were discovered to gild metals. At the beginning, the gold foil was mechanically attached to the metal (it means by folding the foil around the object). Then adhesives (such as egg-white) were used to stick the gold leaf to the metal [35]. Moreover, diffusion bonding permitted to gild silver artifacts by burnishing the gold foil onto the hot substrate. This technique was not often used since the surface oxidation prevented effective bonding when copper was heated in air [35].

Fire gilding, also known as amalgam or mercury gilding, is a technique which was discovered in the 3rd century B.C in China and the 1st century B.C in Europe. It was used as an alternative to diffusion gilding and was a suitable solution for bronze artifacts. This technique was used in Europe and in the Middle East until the apparition of the electroplating method in the mid-19th century [35].

Fire gilding is the method that was used to gild the bronze samples of this section. It consists in creating a paste of gold amalgam by grinding a gold leaf in mercury (1 part of gold in 8 part of mercury, according to Benvenuto Cellini's recipe) (a). This paste is then applied on the surface of the bronze alloy (previously cleaned by nitric acid) and it is heated (b) to produce a porous gilding layer (c) due to mercury evaporation. Finally, the gold layer is burnished by a hard and smooth agate stone tool to give a smooth and reflective surface (d, e) [35].
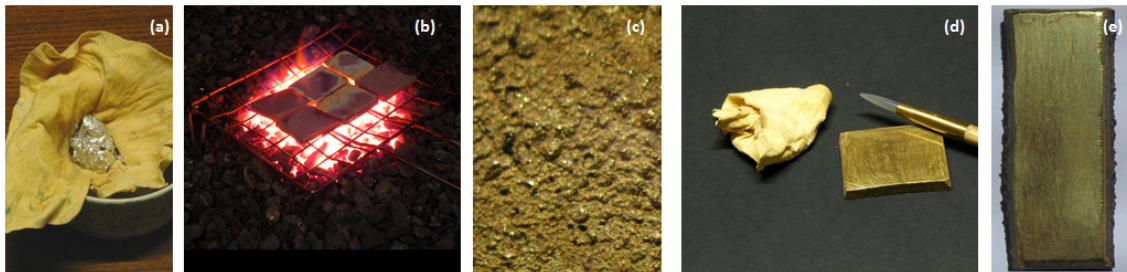
Figure 19: pictures representing the fire gilding steps

Figure 20 shows the surface of the gold layer before and after burnishing. While the surface is matte and porous before this step, it becomes smooth and brilliant after.
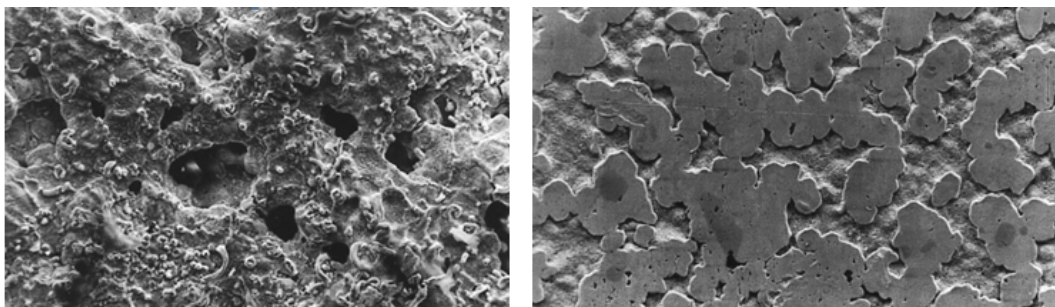
Figure 20: SE image of the surface of an amalgam gilding sample before burnishing (on the left) and after burnishing (on the right) [35]

One alternative to this technique is to coat the bronze alloy with mercury before applying the gold leaf on the metal. Then the heating and burnishing steps are done for obtaining the gold amalgam. However, using mercury, 8-25% of this compound remains in the gold.

By mixing gold and mercury (in excess), a gray γ-gold amalgam (Au_2Hg) is created. The paste of this mixture is then put on the surface of the sample for gilding it. However, due to the low solid solubility of mercury in copper, the wetting of a copper or bronze is more difficult [35]. Moreover, the formation of the copper-oxide layer on the surface, which is formed by contact with air, needs to be removed using nitric acid in addition to the amalgam paste.

For the gilded samples used in this thesis, the fire gilding procedure was carried out by the goldsmith A. Pacini, following the ancient recipes, mainly based on the Treatises of Benvenuto Cellini "On Goldsmithing and Sculpture" (1565-1567).

1.3.4. Conservation of the Paradise Door

The doors of the Baptistery were removed, temporarily, during the World War II for safety.

Because of the fact that the center of Florence (where is located the Baptistery) is highly polluted, and the door suffered damages during the Florence's flood in 1966, restoration works were considered. In 1990, to preserve the panels after over five hundred years of exposure and damage, the Paradise Door was substituted. Currently, the door in the Baptistery is a copy of the original one.

The beginning of the restoration study was in the 1980s when the Opificio delle Pietre Dure planned a diagnostic campaign to restore this door. It consisted first in the cleaning of the panels of the door using chemical reagents [30]. More recently, laser cleaning was used to clean the gilded bronze decorations around the central panels of the door [36]. After restoration, which finished in 2012, the Door has been moved from the laboratories of the Opificio to the Museum of the Opera del Duomo, where it will be kept and exhibited in a display case with controlled indoor environment (dry air, RH<20%). This is an example of the main conservation approach for valuable gilded bronze, which is preventive conservation (i.e. moving the artworks indoor in a controlled environment and substituting them with copies exposed to the outdoor, uncontrollable environment). However, also the active conservation approach (i.e. the use of protective treatments) may be considered.

1.4. Protective treatments for outdoor bronzes : application and removal

The corrosion processes are the main form of degradation that affects the metallic works of art. Moreover, the action of aggressive substances present in the natural environments can produces unaesthetic changes on the surface of the metallic work such as stains, stripes or crusts that can compromise the artwork fruition.

Some ways of forming artificially patina are used by sculptors. These patinas permit to obtain different final visual effects depending on the chemical products that are applied on the surface of bronze [37]:

- Ammonium and sodium sulfides: brown color

- Ammonium chloride and ammonium sulfate: green to blue color

- Chloride salts: green color

Artificial patination offers an alternative in which the bronze surface is chemically treated so that corrosion products are formed more uniformly to a desired appearance. However, many artificial patinas are not very protective [38].

Because of significant increasing air pollution, since the last century, additional protection for bronze and its patina exposed in urban environment is needed. The use of corrosion inhibitors is one of the most commonly employed methods for protection of metals. Generally, it is reasonable in cost, easy to apply, and often reversible. The latter condition is one of the main important requirements of restorers and curators for the protection of the artefact of cultural heritage such as the ethics [39].

Using inhibitors, the protection of bronze is more efficient and the number of required interventions on the metal is decreased.

These inhibitors can be natural, synthetic or microcrystalline waxes sometimes dopped with organic inhibitors (for example benzotriazole). Waxes are brushed, sprayed or wiped onto the surface [37]. Kosec et al. studied the effectiveness of benzotriazole and waxes to protect against corrosion the green nitrate and green chloride patina [40].

Benzotriazole (BTA) and its derivatives are the most commonly used inhibitors (since more than 50 years) in the field of cultural heritage due to their effective action against copper corrosion. However, BTA was proved to be less efficient concerning the bronze corrosion due to the insufficient reactivity of BTA with tin and lead in the alloy [7]. Another drawback of BTA and its derivatives is that they have toxic effects on plants and animals and BTA is suspected to be potentially carcinogenic for humans [5, 6].

For these reasons, it is essential to find others inhibitors providing the same efficiency than BTA without endangering the flora and fauna and human health.

Different inhibitors based on thiadiazole, tetrazole and alkoxysilane compounds have been studied in order to find a good alternative to BTA [41, 42, 43]. It appeared that 3-mercapto-propyl-trimethoxy-silane (PropS-SH) is a good candidate due to its interesting protective properties [41, 8, 44].
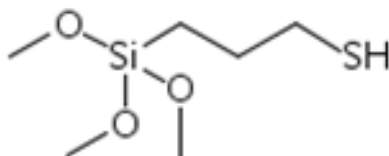
Figure 21: PropS-SH formula

Also, possible modifications of the inhibiting film deserve further researches, such as the addition of nanoparticles, which, in the case of silane-based inhibitors applied on the AZ31 magnesium alloy [10] led to an increase of the protective efficiency.

Before application on any substrate, the hydrolysis of silanes is necessary for having sufficient silanol Si-OH groups, which will interact with the metal substrate. Usually, silanes are applied from dilute water solutions onto the metal surface. In the solution, the silanes are hydrolyzed and silanol groups are formed according to the following reaction:

$$R'\text{-}(CH2)_n\text{-}Si(OR)_3 + 6H_2O \rightarrow R'\text{-}(CH_2)_nSi(OH)_3 + 6\ R\text{-}OH$$
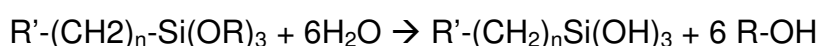
After hydrolysis, the hydrolyzed silanol groups can undergo condensation reactions, resulting in slow polymerization and eventual precipitation. The factors influencing the kinetics and equilibrium of hydrolysis and condensation of silanes in solutions are the nature of the organofunctional groups, the concentration of silanes and water, the value of the solution pH, the temperature and the aging of the solution. Because both hydrolysis and condensation reactions are acid or base catalyzed, solution pH is the major factor governing the stability of silanes in aqueous solutions.
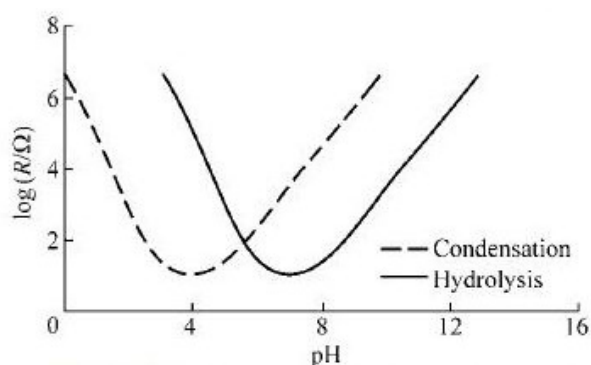
Figure 22: Hydrolysis and condensation rate of a typical silane [45]

Although acids and bases are catalysts for both hydrolysis and condensation of alkoxysilanes, these two processes have different pH dependences. When the reactions are OH− catalyzed, a high rate of condensation is favored with rapid gelation. On the

contrary, when reactions are H$^+$ catalyzed, a high rate of hydrolysis is favored with slow gelation [46].

The process of inhibition of the metal is its dipping into a silane solution. This action is followed by the adsorption of the silanol groups on the metal surface thanks to hydrogen bonds.
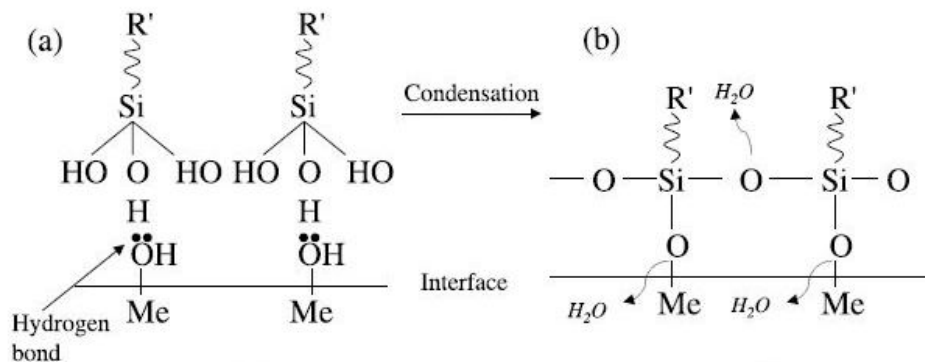
Figure 23: Simplified scheme of bonding mechanism between silane molecules and metal surface hydroxide layer; (a) before condensation: hydrogen-bonded interface and (b) after condensation: covalent-bonded interface [47]

The curing is related to the reaction of silanol groups (SiOH) with each other by cross-linking, with the formation of a Si-O-Si network according to the condensation reaction:

$$SiOH + HOSi = SiOSi + H_2O$$
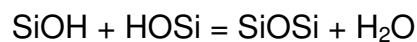
But also the condensation of SiOH groups in the solution and MeOH groups on the metal surface to produce metallo-siloxane bonds (Me-O-Si). During this process, water evaporates.

$$MeOH + HOSi^- = MeOSi^- + H_2O$$
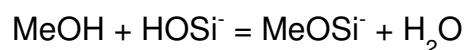
Concerning PropS-SH on copper, metal thiolate bonds (Me-S-C) also form improving the surface adhesion of the silanic film to the metal, compared to oxane bonds [48], resulting in an improvement of the inhibitive effects [49].
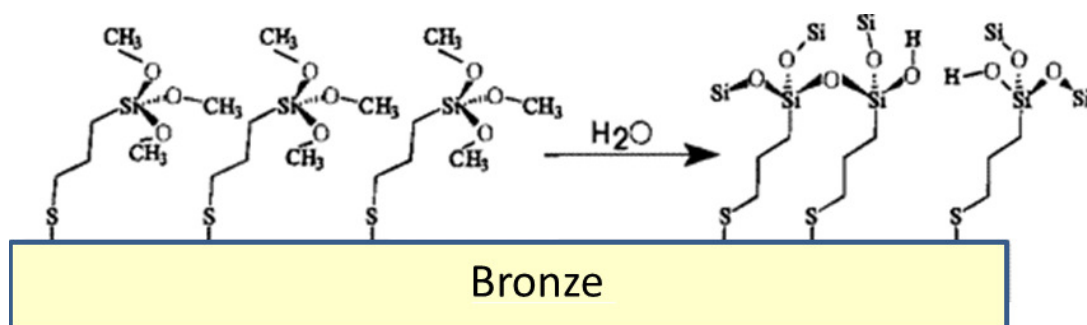
Figure 24: PropS-SH on bronze [48]

For preparing the silane solution, a mixture of deionized water and ethanol is used for dissolving the silane agents. The ratio of silane/DI water/ethanol is 5:5:90 (v/v/v) with a pH adjusted to 4.

The silane solution is aged at room temperature for 1 month to allow the hydrolysis of the Si-OCH$_3$ groups. After that, the bronze sample is coated by immersion of the sample into a hydroalcoholic solution of silane agents for 1 hour at 20°C.

Finally, the bronze sample is dried and cured for 10 days at room temperature for inducing the coating reticulation [50]. This step permits to obtain optimum protection efficiency.

It has been shown that after a 30 days curing, the silane crosslinking is still incomplete. However, a 10 days curing is retained for the inhibited procedure because it is the best compromise between the requirements of high protectiveness of the films and an acceptable speed of work [41].

The removal of the inhibitor is one priority because its effectiveness may decrease with time. Moreover, one request in the field of cultural heritage is to have a reversibility of the process of application of a protective coating. It means that we should be able to go back to the original state of the masterpiece [51]. The protective coatings on bronze can be removed either by chemical or mechanical methods (by the use of solvents or by controlled abrasion, respectively). These methods were also applied for cleaning the patina. In recent years, also laser treatments gained an increasing research attention for patina cleaning as well as for removing protective coatings.

The Opificio delle Pietre Dure of Florence studied both chemical and laser approaches on the gilded bronze from the Paradise Door [52]. Ion-exchange resin, trisodium EDTA salt and Rochelle salt were investigated as reagents for chemical cleaning. It has been demonstrated that concentrated neutral aqueous solution of Rochelle salt is the most selective chemical cleaning of the cuprite layer underlying the gold film [52]. Since the gold film is weakly bonded to the substrate, chemical cleaning is still preferred instead of the laser treatment. This is particularly true for gilded sections that can be detached from the bronze frame, because both the front and the back side of the panels can be treated by chemical cleaning followed by deep rinsing. Conversely, the laser treatment was successfully applied for cleaning the gilded sections of the door which were difficult to take out of the bronze frame [36].

The use of laser treatments for removing either corrosion products or protective coatings by laser ablation involves a set-up phase, where the main parameters of the laser source (such as pulse width and energy density) have to be carefully optimized as a function of the surface features of the object to be treated, in order to avoid unwanted thermal effects such as microstructural modifications or micro-melting [53].

Experimental

Section 1

STUDY OF THE EFFICIENCY OF PROTECTIVE TREATMENTS FOR BRONZES BY ACCELERATED CORROSION TESTS

1.1. Accelerated corrosion test

In order to evaluate the protective efficiency of the surface treatments, accelerated corrosion conditions were used. They consist of different ageing tests describing the different action of the rain. Since it has been shown that in real outdoor bronze monuments, the corrosion behavior is strongly influenced by the exposure geometry (sheltered and unsheltered areas with respect to the action of rainfall) [4], it is necessary to simulate both sheltered and unsheltered conditions. It is thus important to understand the mechanisms of formation of the patina in order to find a proper conservation strategy.

With the purpose to acquire a better understanding of the interactions between outdoor bronzes and the environment, different devices have been developed to simulate real outdoor conditions into the laboratory. In particular, accelerated ageing devices by wet & dry (simulating the action of stagnant rain in sheltered areas) and by dropping (simulating the leaching action of the rain in unsheltered areas) tests were designed [12, 1].

In the present work, we used the dropping test as a method to produce pre-patinated bronze surfaces to be used as a representative substrate for the application of the silane coating (first step) and, subsequently, for evaluating its protective efficiency on aged surfaces (second step).

1.1.1. Tested material: quaternary bronze and organic coating (PropS-SH + nanoparticles)

The samples used for studying the protective efficiency of the 3-mercapto-propyl-trimethoxy-silane (shortly PropS-SH) with nanoparticles by dropping test were coupons of quaternary bronze (manufactured by the goldsmith A.Pacini of Montepulciano (SI), reproducing the composition of the bronze Paradise Doors of the Baptistery in Florence). The chemical composition of the bronze, measured in a previous work [20], is shown in table 1.

	Cu	Sn	Zn	Pb	Sb
Weight%	91.9	2.4	2.9	1.0	0.8

Table 1: Composition of the alloy (by FAAS)

The dropping test device (described in section 1.1.2) was first used in the pre-patination step for ageing the samples by creating a patina on the bronze surfaces. In that way, the patinated samples are representative of the real substrates on which conservation interventions are applied (bare metals can only be found in contemporary art monuments).

Then, a protective coating was applied on the pre-patinated samples. This coating is a silane coating (3-mercapto-propyl-trimethoxy-silane (henceforward PropS-SH)), with the following structural formula:
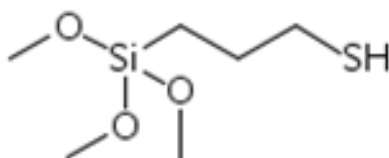
Figure 1: PropS-SH structural formula

The application method of the inhibitor is described in 1.1.4 and it is done at the University of Ferrara, Corrosion and Metallurgy Centre "A.Daccò".

Finally, the dropping test was used for testing the protective efficiency of the different kinds of samples: coated/patinated and uncoated/patinated. The latest will be the reference sample (which was aged but not inhibited). Before the pre-patination step, the samples were polished with 1000 grit sandpaper with the purpose to remove all the scratches (which are preferential sites for the corrosion process to occur), and obtain a shiny surface. After sanding, they were washed with distilled water, dried with a hairdryer and put into a desiccator. Later, they were weighted and their lengths, widths and thicknesses were measured with the purpose to calculate the total surface area of each coupon.

A summary of the development of this test is shown in table 2.

sample	Pre-patination by dropping test	Protective coating	Ageing by dropping test
H	31d TOW	none	10d TOW
E	19d TOW	PropS-SH + TiO_2	10d TOW
F	22d TOW	PropS-SH + La_2O_3	10d TOW
G	19d TOW	PropS-SH + CeO_2	10d TOW

Table 2: Samples under artificial exposure (dropping test); TOW = time of wetness

During the pre-patination step, it is considered that the ageing is satisfactory when the mass percentage of Sn on the surface is almost equal to ~ 20% (in agreement with

enrichment in Sn observed on previous studies about unsheltered areas of real outdoor bronze [28]).

For the sample H, this percentage was too low after the first cycle of dropping ($\sim$ 13%) so the pre-patination step by dropping was extend until the tin percentage reached $\sim$ 20%. In that way, the pre-patination phase of sample H lasted 31d TOW. For the same reason, the dropping test on sample F took more time than on sample E and sample G (22 days instead of 19 days).

Figure 2 shows the pictures of the reference sample surface and coated sample surfaces, before and after ageing step. In the case of the reference sample, a more noticeable change in the color of the surface appears after ageing, due to the formation of a patina which is more developed than in the case of the inhibited samples.
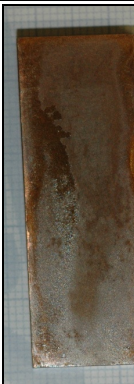
Ageing time	Reference sample	Coated Prepatinated PropS-SH + CeO_2	Coated Prepatinated PropS-SH + La_2O_3	Coated Prepatinated PropS-SH + TiO_2
(0d TOW)				
(10d TOW)				

Figure 2: sample surfaces at different ageing times
TOW = time of wetness

1.1.2. Weathering method: dropping test

The atmospheric exposure is simulated through a cyclic exposure of the alloy to a precipitation runoff where an artificial rain is periodically dripped on the sample. It means that this test simulates a severe runoff condition with a solution reproducing natural acid rain.

As above mentioned, this dropping test was thus used for two different approaches. The first one is the production of the patina by accelerated ageing. This first step (pre-patination) is done before applying the corrosion inhibitor because the goal is to simulate the situation of actual conservation interventions (it means having a patinated sample and not a bare metal). The second approach is to use the dropping test as an exposure test with a view to study the effectiveness of the inhibitor on bronze surfaces.

The device consists on a support inclined at 45° where the samples are mounted. The support is pierced in order to pass pipes carrying the artificial rain using a pump system. The leaching solutions are collected under the support and then analyzed. Immediately after collection, the leaching solution is acidified at pH < 2 with HNO3 65% suprapur in order to avoid absorption of metals on the container surfaces and dissolve possible metal complexes [54].
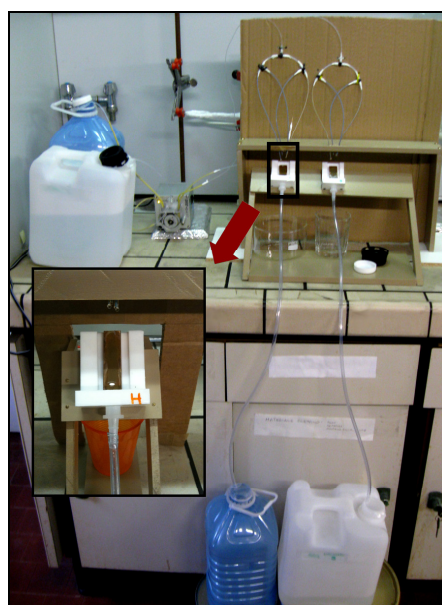
Figure 3: dropping test device

During ageing test, the evolution of the surface corrosion and the metal release in the ageing solution were analyzed through the use of a wide range of spectroscopic techniques. In particular, the sample surface was monitored by SEM, EDS, Raman spectroscopy, XRD and color measurement whereas the metal release in the leaching solutions was monitored by AAS.

An X-ray diffractometry (XRD) in the Bragg-Brentano geometry, using Cu Kα radiation (λ = 0.154060 nm) was utilized.

For the μ-Raman analysis, the spectra were acquired with the Invia-Renishaw device. A wavelength of 514.5 nm was used to limit fluorescence and spectra were acquired in the range 0-4000 cm^{-1}. The laser power was set to 50 mW (=100%) for all spectra, due to the fact that no thermal degradation of the corrosion products had been observed.

The solutions sampled during exposure test were analysed by graphite furnace atomic absorption (GFAAS, Perkin-Elmer AAnalyst 400) using pyrocoated graphite tubes with L'vov platform.

Colour was measured by Reflectance Spectrophotometry (illuminant D65, 10° observer, beam of diffuse light of 6 mm) and data elaborated in the CIELAB colour system. In this system, the difference between two colours is expressed by the ΔE* parameter:

$$\Delta E^* = \sqrt{(\Delta L*)^2 + (\Delta a*)^2 + (\Delta b*)^2}$$

where L*, a* and b* represent the lightness, the red/green and the yellow/blue axis, respectively.

In the field of Cultural Heritage, ΔE=3 is considered as a perceptibility threshold [55].

1.1.3.   Artificial acid rain solution

Starting from the detected concentrations in natural rain, a synthetic rain (SR) containing the same quantities of the main inorganic and organic ions has been prepared. The real acid rain consists of a mixture of nine weekly natural rain samples (pH < 4.5), collected in Bologna (an urban site in northern Italy), during winter months.

The artificial rain was synthesized with analytical grade reagents and ultra-pure deionized water.

The composition of the synthetic rain is shown in Table 3.

Synthetic Rain (SR)	
Conductivity (20°C)	37,92 ± 0,09 µS/cm
pH	4,27 ± 0,01
Cl^-	1,24 ± 0,04 mg/L
$N.NO_3^-$	1,02 ± 0,02 mg/L
SO_4^{2-}	1,94 ± 0,02 mg/L
CH_3COO^-	0,23 ± 0,02 mg/L
$HCOO^-$	0,04 ± 0,02 mg/L
$N.NH_4^+$	0,86 ± 0,03 mg/L

Table 3: Chemical composition of the synthetic rain (SR)

1.1.4. Application of coating

The samples were inhibited at the University of Ferrara, in the Centro di Corrosione "A. Daccò". PropS-SH was chosen as inhibitor according to its advantages (discussed in the Introduction).

The application of the protective silane coating on the samples can be described as following:

- Preparation of a solution with 90% ethanol, 5% water and 5% of the inhibitor (PropS-SH, pH 4)
- 1 month of waiting to permits the hydrolysis of the $Si-OCH_3$ groups in the solution
- 1 hour of immersion of the samples into the hydrolyzed solution
- Coupons are taken out of the solution and dried for 10 days at room temperature (no heating is applied at any moment) for having a coating reticulation

For having the silane molecules adhering to the metal surface, the hydrolyzed form of the silane coating has to be used. In that way, the coating is absorbed by the substrate thanks to the formation of hydrogen bonds between silanol (SiOH) groups of the silane and metal hydroxyls (MeOH) at the metal surface. These bonds are due to the presence of air-formed oxide films [56].

During the curing process, condensation steps occur, between SiOH and MeOH groups, resulting in the formation of metallo-siloxane (MeOSi) and siloxane (SiOSi) covalent bonds on the metal surface.

In the case of PropS-SH on Cu, the reaction between the silane and the cuprous oxide film on the metal surface gives birth to the formation of Cu(I)-thiolate bonds in the first adsorption step [8]. Thus, the alloy composition plays a role in the adhesion strength of PropS-SH coating and, in the case of pre-patinated surfaces, this adhesion is certainly correlated to the patina nature and its stability.

As said before in introduction, the curing time at room temperature was found to significantly affect the inhibiting efficiency and a period of 10 days was selected on the basis of previous work [41].

Concerning PropS-SH coatings containing metal oxide nanoparticles, it was obtained by dispersion of 250 ppm of the nanoparticles CeO_2 (nominal size < 25 nm), La_2O_3 (nominal size ~100 nm), TiO_2 (nominal size < 25 nm) which were dispersed into the hydrolyzed silane solutions. This addition permits to accelerate the pre-filming treatment without losing the protective properties of the silane coating [57].

In PropS-SH, the metal oxide nanoparticles can be trapped into a siloxanic strong network formed by condensation reactions coming from the hydrolysis of the methoxy group [50].

1.2. Results

In this part are shown the results coming from different analysis that were run on the samples. Those results permit to draw conclusions about the inhibitor efficiency by making a comparison between the samples with and without the silane layer and between silane layer with or without nano-particles, considering that the silane layer without nanoparticles was investigated in a previous thesis work [58], in the same conditions as for the present work.

1.2.1.   Gravimetric measurements

Gravimetric measurements have been done on the samples at different times of wetness (TOW) during the ageing test with the purpose to observe the mass variations. Results are shown in figure 4:
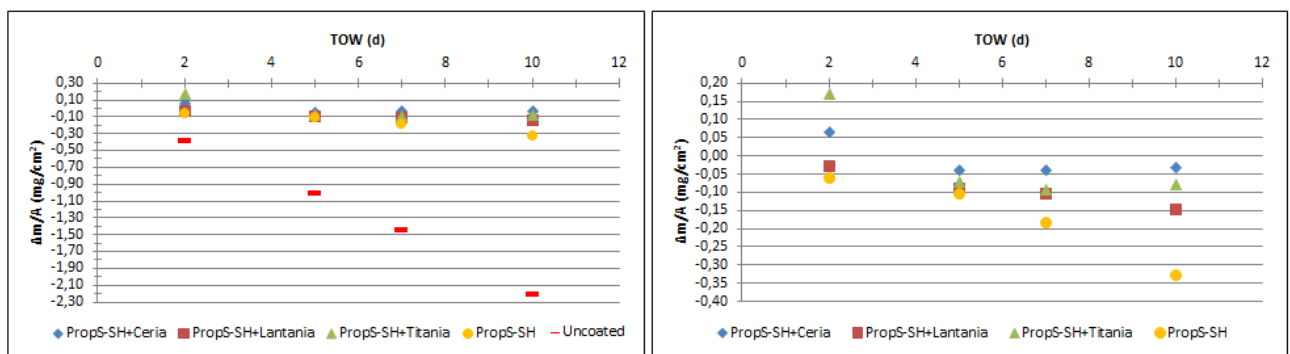
Figure 4: gravimetric measurements of all samples during the ageing test (uncoated sample without inhibitor)

The graph on the right does not contain the blank (uncoated) sample for having a better view of the other samples.

The mass variation of the uncoated sample is significantly higher compared to the other samples. Moreover, the mass variation is lower concerning the coated samples containing nano-particles than the one coated only with PropS-SH. Thus it indicates that the silane coating has a considerable impact on the decrease of the mass variation and it has a better efficiency on mass variation when it contains nano-particles.

At 2d TOW, a positive mass variation occurs for PropS-SH+ TiO_2 and PropS-SH+ CeO_2, thus the growth of corrosion products overrides the leaching action of the rain in the dropping test.

From 2d TOW to 10d TOW, the mass variation decreases progressively before its stabilization around 10d TOW. At the end of the ageing test (10d TOW), the mass variation shows the following order:

$$PropS\text{-}SH > PropS\text{-}SH+La_2O_3 > PropS\text{-}SH+ TiO_2 > PropS\text{-}SH+ CeO_2$$

1.2.2. Ageing solutions : Atomic Absorption Spectroscopy

Atomic Absorption Spectroscopy analysis was run on the leaching solutions that were collected during the ageing test. The results permit to obtain information about the release of the alloying elements from metallic surface. Elemental concentrations (in ppb) were measured for each one of the sampled solutions and normalised by the corroded area of the respective coupon. Results are shown in the following sub-paragraphs.

- **Cu release**

Figure 5 shows the daily release of Cu for all the samples:
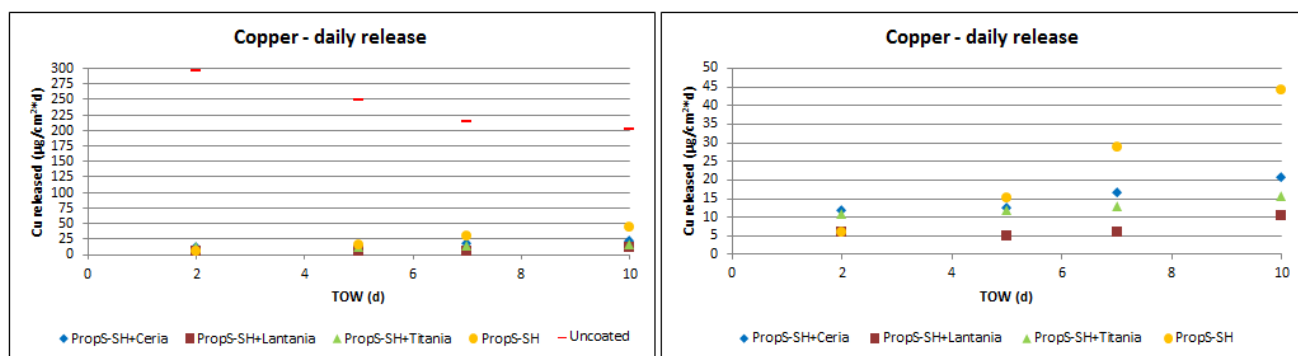
Figure 5: daily release of Cu for all the samples during ageing test; graph on the right: without the uncoated sample

The Cu release decreases for the blank sample whereas it increases slightly for the other samples. Concerning the uncoated sample, the decrease is due to the fact that, probably, there is the formation of a product layer that slows down the Cu dissolution in the case of the uncoated sample.

In the case of PropS-SH, at the end of the ageing test, the amount of released metal is almost twice the value of the other coated samples. It shows that the efficiency of the inhibitor is better with nano-particles.

 At the end of the ageing test (10d TOW), the Cu daily release shows the following order:

$$PropS\text{-}SH > PropS\text{-}SH+ CeO_2 > PropS\text{-}SH+ TiO_2 > PropS\text{-}SH+ La_2O_3$$

Figure 6 shows the cumulative release of Cu for all the samples:
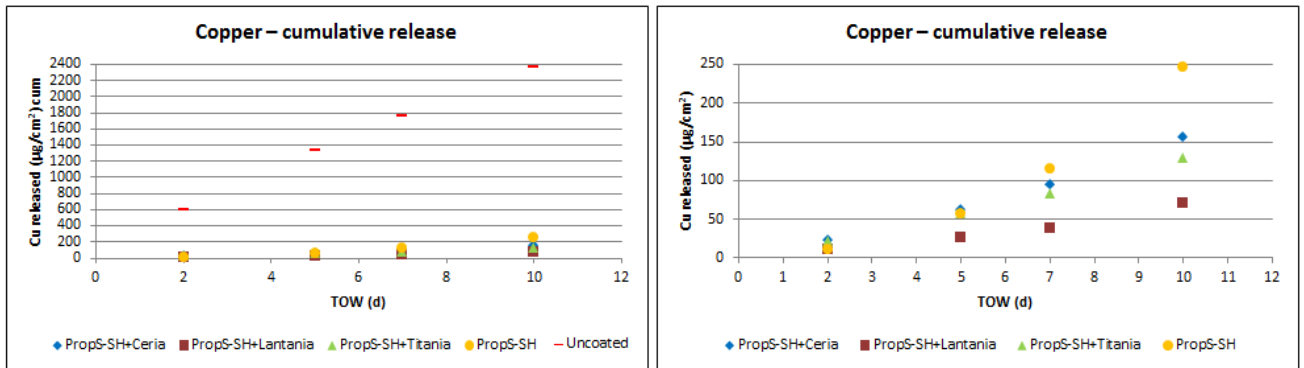
Figure 6: cumulative release of Cu for all the samples during the ageing test; graph on the right: without the uncoated sample

For all samples, there is a higher release of Cu at 10d TOW with:

$$PropS\text{-}SH > PropS\text{-}SH + CeO_2 > PropS\text{-}SH + TiO_2 > PropS\text{-}SH + La_2O_3$$

- **Zinc release**

Figure 7 shows the daily release of Zn for all the samples:
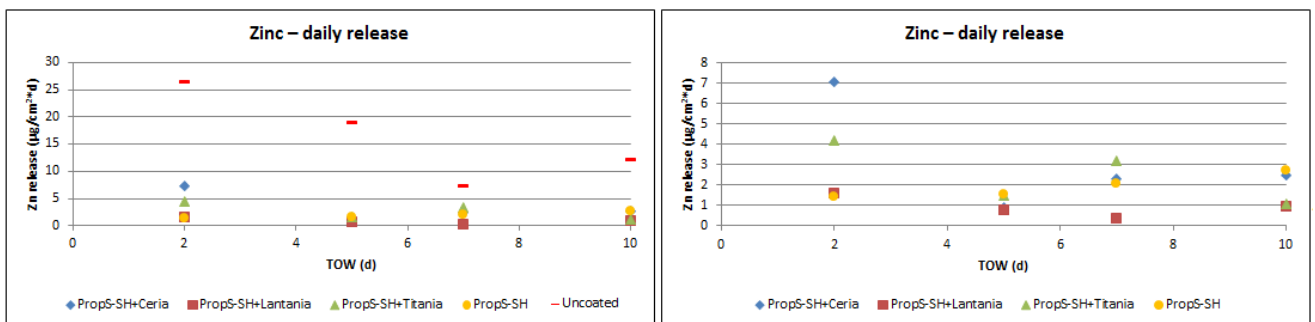
Figure 7: daily release of Zn for all the samples during the ageing test; graph on the right: without the uncoated sample

The Zn release decreases for the blank sample until 7d TOW. This might be due to the formation of a product layer that slows down the Zn dissolution.

There is an increase of the Zn release in the case of PropS-SH without nano-particles, whereas Zn release decreases for the other inhibited samples.

For PropS-SH+ CeO_2 and PropS-SH+ TiO_2, there is a strong release of Zn at 2d TOW followed by an important decrease afterwards.

At the end of the ageing test (10d TOW), the Zn daily release shows the following order:

- PropS-SH $\approx$ PropS-SH+ CeO_2 > PropS-SH+ TiO_2 $\approx$ PropS-SH+ La_2O_3
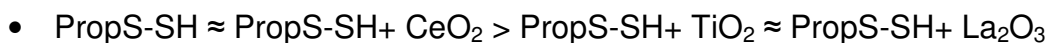
Figure 8 shows the cumulative release of Zn for all the samples:

37
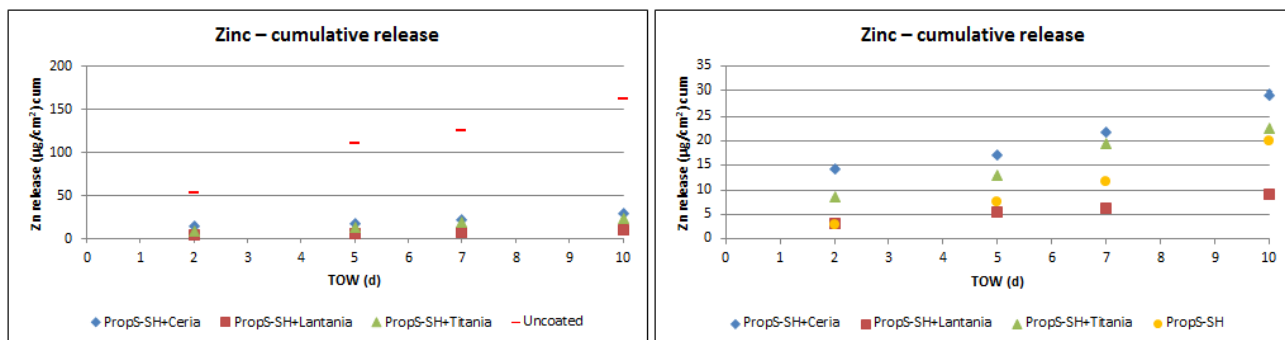
Figure 8: cumulative release of Zn for all the samples during the ageing test; graph on the right: without the uncoated sample

For all the samples, there is almost the same release at different times of wetness.

At 10d TOW, the cumulative release follows this order:

$$PropS\text{-}SH + CeO_2 > PropS\text{-}SH + TiO_2 \approx PropS\text{-}SH > PropS\text{-}SH + La_2O_3$$
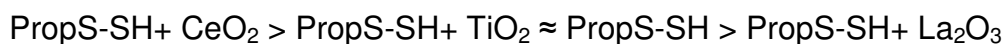
- **Lead release**

Figure 9 shows the daily release of Pb for all the samples:
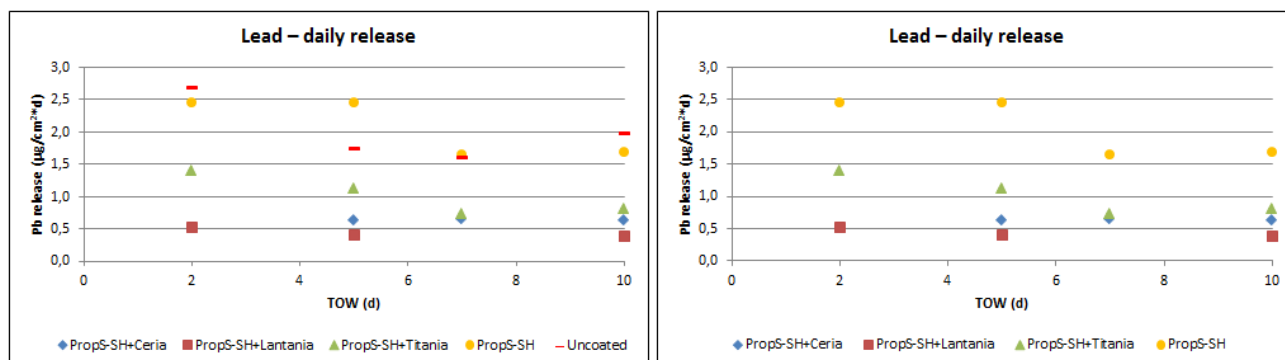
Figure 9: daily release of Pb for all the samples during the ageing test; graph on the right: without the uncoated sample

The Pb daily release decreases for the blank sample until 7d TOW. This may be due to the formation of a product layer that slows down the Pb dissolution.

At the end of the ageing test (10d TOW), the Pb daily release shows the following order:

$$PropS\text{-}SH > PropS\text{-}SH + TiO_2 \approx PropS\text{-}SH + CeO_2 \approx PropS\text{-}SH + La_2O_3$$

Figure 10 shows the cumulative release of Pb for all the samples:

38
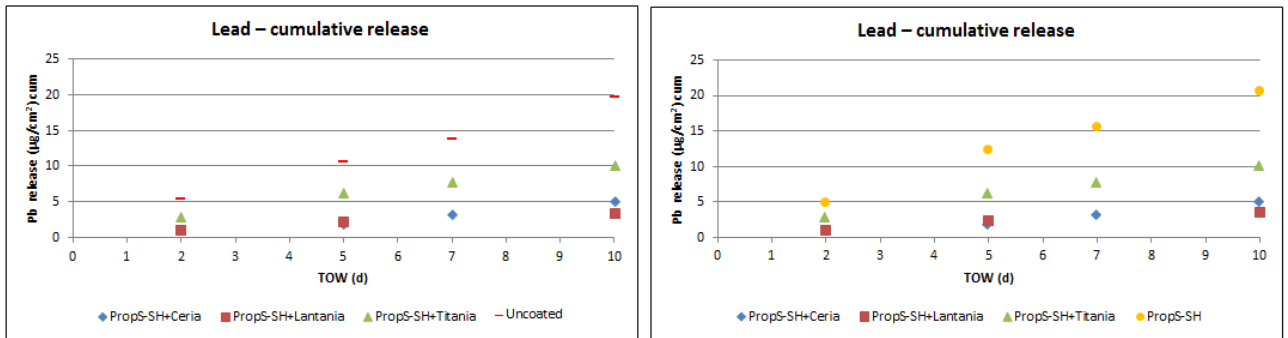
Figure 10: cumulative release of Pb for all the samples during the ageing test; graph on the right: without the uncoated sample

At 10d TOW, the cumulative release follows this order:

$$PropS\text{-}SH > PropS\text{-}SH+ TiO_2 > PropS\text{-}SH+ CeO_2 \approx PropS\text{-}SH+ La_2O_3$$

1.2.3. Inhibiting efficiency

In order to express the ability of the silane coating to protect the sample against corrosion, an inhibiting efficiency (IE) calculation was done. IE is calculated using the formula:

$$IE = \frac{M_{sol,\,NI} - M_{sol,I}}{M_{sol.NI}} \times 100$$

Where :

- IE = inhibiting efficiency (in percentage).

- IE is equal to 100% if no metal is released from the coated coupon whereas it is equal to 0% if the coated coupon releases as much metal as the uncoated one.

- M sol = amount of metal in the leaching solution (Cu or Zn or Pb, in $\mu g\ cm^{-2}$)

- NI = non-coated coupon (blank coupon)

- I = coated coupon

Table 4 provides information on the inhibitor efficiency for all the alloying elements on the different coated samples and calculated at the end of ageing test (10d TOW):

Inhibitor efficiency of Cu (%)				
TOW	PropS-SH	PropS-SH+CeO$_2$	PropS-SH+TiO$_2$	PropS-SH+La$_2$O$_3$
10d	83	93	95	97

Inhibitor efficiency of Pb (%)				
TOW	PropS-SH	PropS-SH+CeO$_2$	PropS-SH+TiO$_2$	PropS-SH+La$_2$O$_3$
10d	27	74	48	82

Inhibitor efficiency of Zn (%)				
TOW	PropS-SH	PropS-SH+CeO$_2$	PropS-SH+TiO$_2$	PropS-SH+La$_2$O$_3$
10d	76	82	86	94

Table 4: inhibiting efficiency of the coated samples for the different alloying elements at the end of the ageing test (10d TOW)

It appears that in all cases, the coating works better when it contains nano-particles. Moreover, the highest efficiency is for PropS-SH containing La$_2$O$_3$ whereas the lowest one is for PropS-SH containing CeO$_2$ (in most of the cases).

There is a drastic decrease of the inhibiting efficiency in the case of Pb compared to Cu that has the highest IE% values. This may be explained on the basis of further investigations on corroded surfaces (reported in the next section).

The equation was also used to calculate the total inhibiting efficiency, at the end of the ageing test (10d TOW), which is the sum of all the values for the alloying elements. Table 5 shows the results:

Total inhibitor efficiency (%)				
TOW	PropS-SH	PropS-SH+ CeO$_2$	PropS-SH+ TiO$_2$	PropS-SH+ La$_2$O$_3$
10d	84	93	94	97

Table 5: total inhibiting efficiency of the coated samples at the end of the ageing test (10d TOW)

At the end of the ageing cycle (10d TOW), the total inhibiting efficiency is higher than 80% in all cases. This demonstrates a good protective action of the coating against the corrosion process. Moreover, as said before, PropS-SH that contains nano-particles ends up with less release of metals by comparison to PropS-SH without nano-particles. The total IE values do not change remarkably with the nature of the nanoparticles and are always higher than 90%.

1.2.4. Characterization of corroded surfaces : SEM-EDS, µ-Raman, XRD

1.2.4.1. Analysis of cross sections

In order to have complementary information both on the bulk alloy (the original microstructure) and on the adhering corrosion layer, examination of the cross-section of samples from the dropping test was also performed at the end of the ageing test.

Figure 11 is a summary of the samples analyzed with their characteristic layers.

Figure 11: Samples name and their characteristic layers

The samples were first cut near to the area where the artificial rain fell during the dropping test. Then they were embedded into a conductive resin. In fact, this resin contains graphite which is a conductive material and thus permits to avoid charging effects on the sample during the SEM analysis. Finally, the cross sections were polished with sandpapers at decreasing grain size with the purpose to remove all the scratches and obtain a mirror surface.

During the polishing step, some defects on the metal appeared. They are due to the solidification process, during which both shrinkage and gas evolution occurred.

By analyzing the cross-sections, some corrosion morphologies in the metal are highlighted such as intergranular corrosion or pitting.

The cross sections were analyzed by SEM analysis on different sites of interest. Results are shown in the following sub-paragraphs.

a. Sample H: without PropS-SH

- Site of interest 1
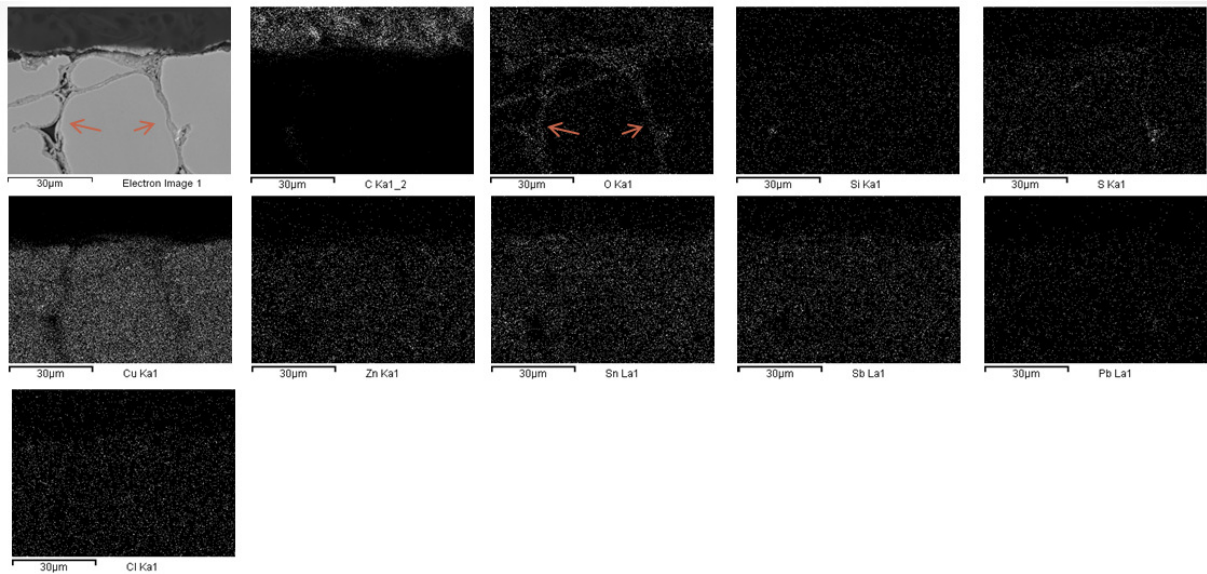
Figure 12: BSE image and X-ray maps for the different elements of interest in sample H (without coating)

This sample shows a characteristic form of corrosion called intergranular corrosion (orange arrows). The intergranular corrosion is a preferential attack and penetration of corroding agents along the grain boundaries (zones with high energy content). Such an evident corrosive attack is due to the absence of the protective silane coating.

In this area, the Sn-rich products layer is not as evident: maybe it was locally damaged during the metallographic preparation.

- Site of interest 2
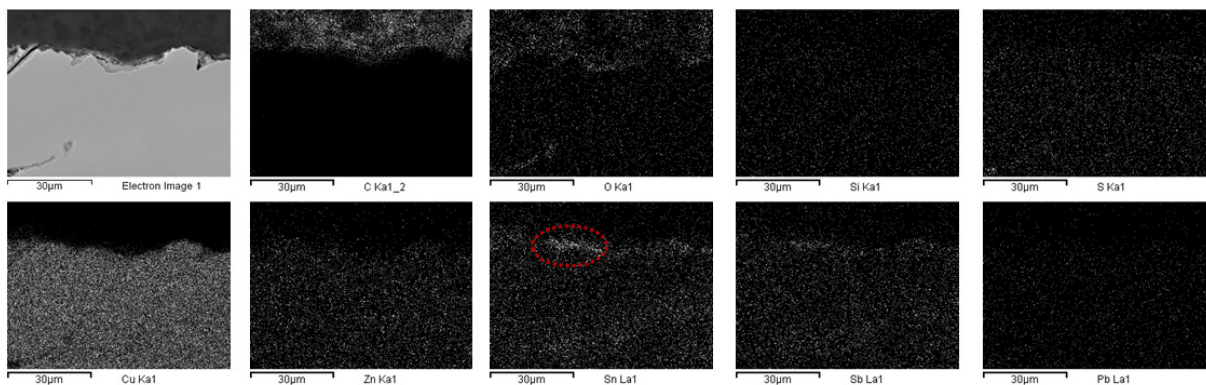
Figure 13: BSE image and X-ray maps for the different elements of interest in sample H (without coating)

The resulting patina displays some small Sn-rich zones over Sn-rich interdendritic areas (orange circle). Thus, according to literature [1], we can affirm that in the corrosion layer, tin species are mainly formed over the external part of the dendrites.

- Site of interest 3
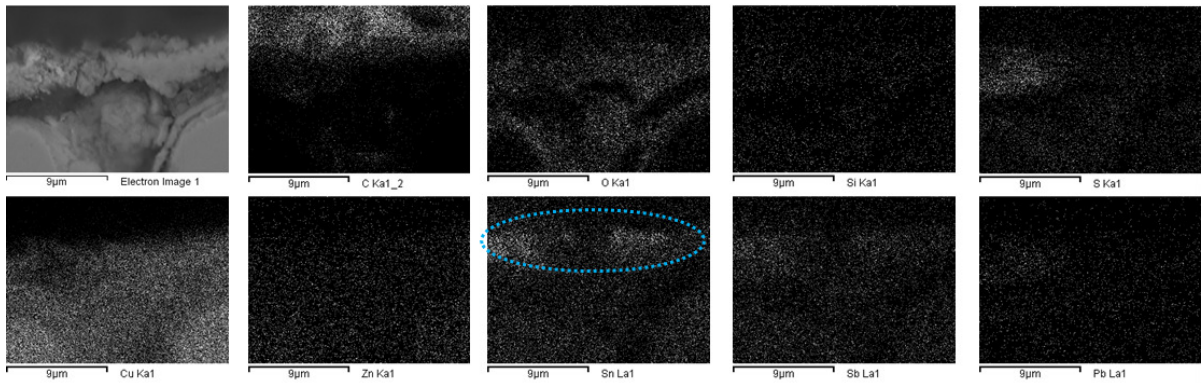
Figure 14: BSE image and X-ray maps for the different elements of interest in sample H (without coating)

This sample seems to show a characteristic form of corrosion called pitting corrosion. The pitting corrosion is a localized corrosion attack, confined to a point or small area that takes the form of cavities.

The blue circle shows the presence of Sn-rich products layer.

- Site of interest 4
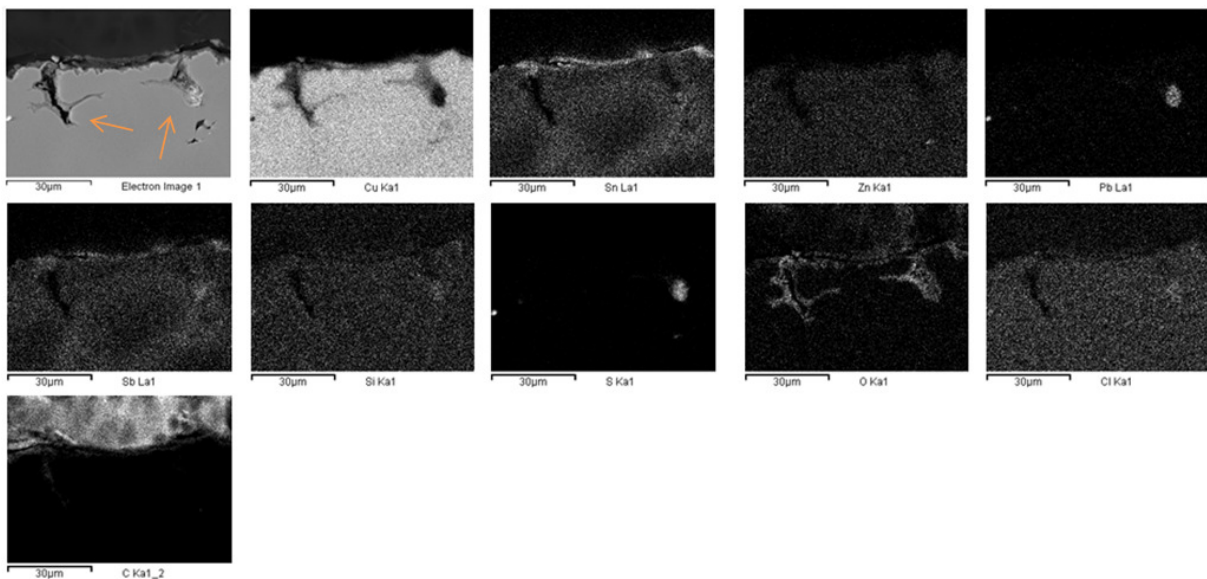
Figure 15: BSE image and X-ray maps for the different elements of interest in sample H (without coating)

In this site also it is observed the presence of Sn-rich products layer. Moreover, casting defects filled up by corrosion products (O and Cl) are observed (orange arrows).

b. Sample A: PropS-SH

- Site of interest 1
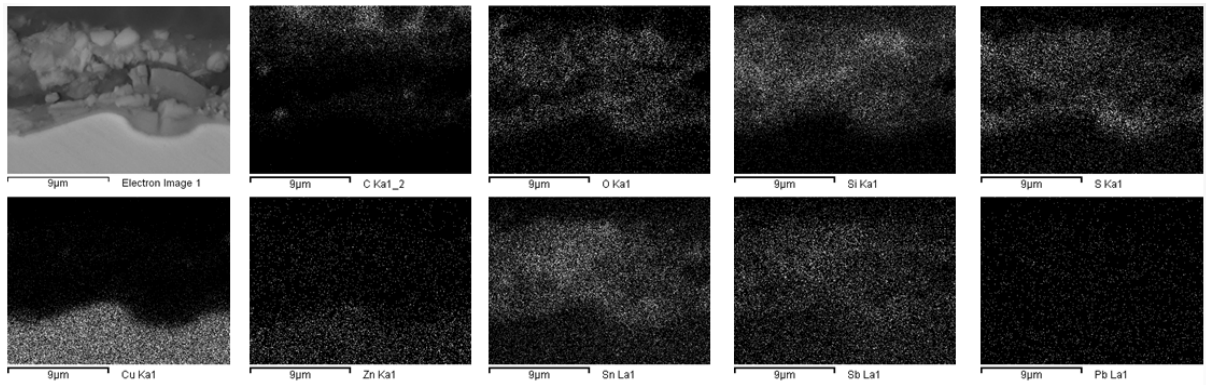
Figure 16: BSE image and X-ray maps for the different elements of interest in sample A (coated with PropS-SH)

According to the EDS results, we can differentiate between the bronze substrate and the corrosion layer (*patina*).

Specifically we observe that the corrosion layer (grey area in the top-left BSE image) is Sn-rich. In fact, previous studies confirm that under a severe permanent leaching drop effect, a progressive dissolution of Cu in the bronze alloy takes place. Sn cations remain in the patina, forming poorly crystallized stable species, related to the presence of $SnO_x(OH)_y$ [1].

Moreover, in the corrosion layer we observe, together with Sn, elements from the silane protective coating, such as Si and S probably due to the ability of the silane coating to go into the porous patina.

- Site of interest 2
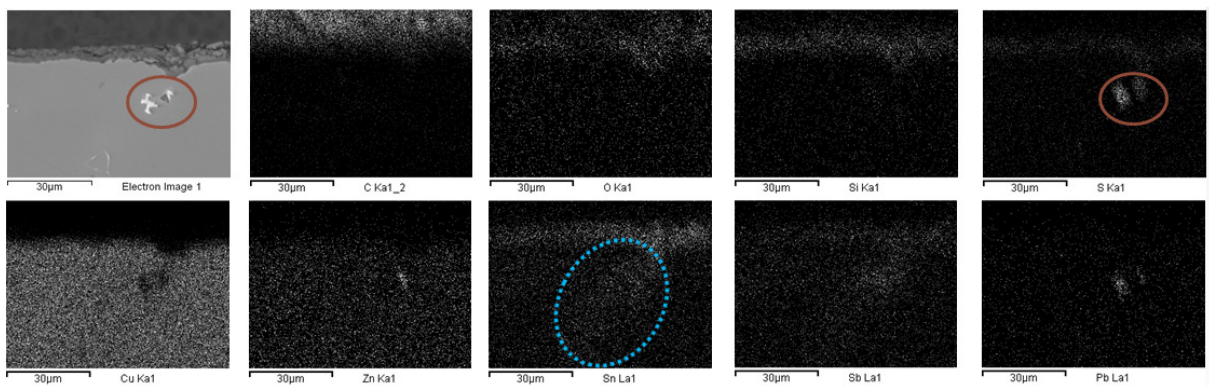
Figure 17: BSE image and X-ray maps for the different elements of interest in sample A (coated with PropS-SH)

Sn products and inhibitor elements (Si and S) are localized in the same areas, corresponding to the corrosion layer, due to the porosity of the patina.

The X-ray maps highlight that the areas corresponding to the core of the dendrites are rich in Cu, whereas the interdendritic areas (blue circle) are Sn-enriched because of notable microsegregation due to casting.

Moreover, in the interdendritic spaces, we can also observe Pb globules, insoluble in the Cu matrix, and some inclusions of ZnS (see S and Zn maps).

- Site of interest 3

Element	Spectrum 1	Spectrum 2	Spectrum 3
C	14.64	42.17	49.76
O	16.09	22.19	25.09
Si	4.52	4.05	2.98
S	4.19	3.44	2.41
Cu	43.95	17.55	7.62
Zn	1.45	-	-
Sn	13.92	10.59	12.14
Sb	1.23	-	-
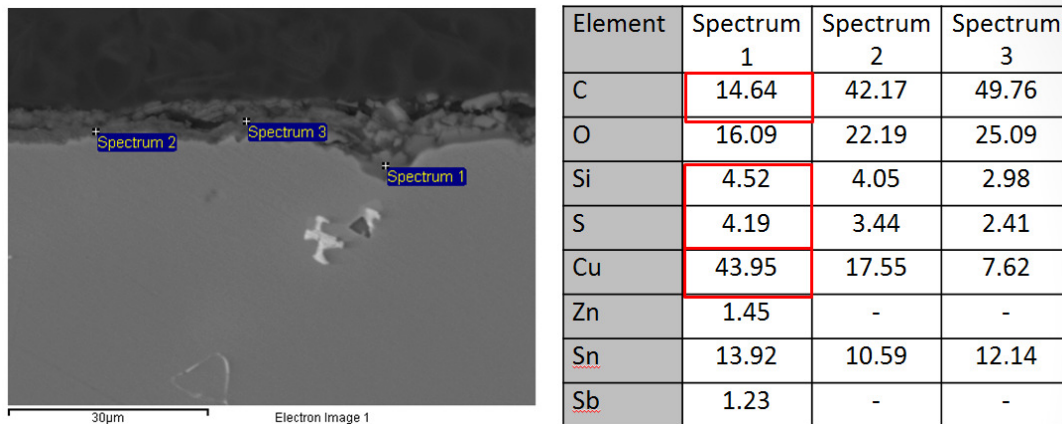
Figure 18: BSE image and X-ray maps for the different elements of interest in sample A (coated with PropS-SH)

Zone 1 (area under a more thick patina) contains more Cu and Zn than zone 2 and zone 3. The results confirm that in the case of bronzes exposed to the leaching action of rainwater, a specific mechanism is developed by migration/dissolution of Cu and Zn cations through the thin patina towards the interface with the environment [4].

The higher concentration of C in zone 2 and zone 3 is related to the mounting resin. This resin impregnates the patina and results in overestimation of the C amount by EDS. There is less C in zone 1 because it is localized deeper into the patina whereas zone 2 and 3 are closer to the resin.

- Site of interest 4
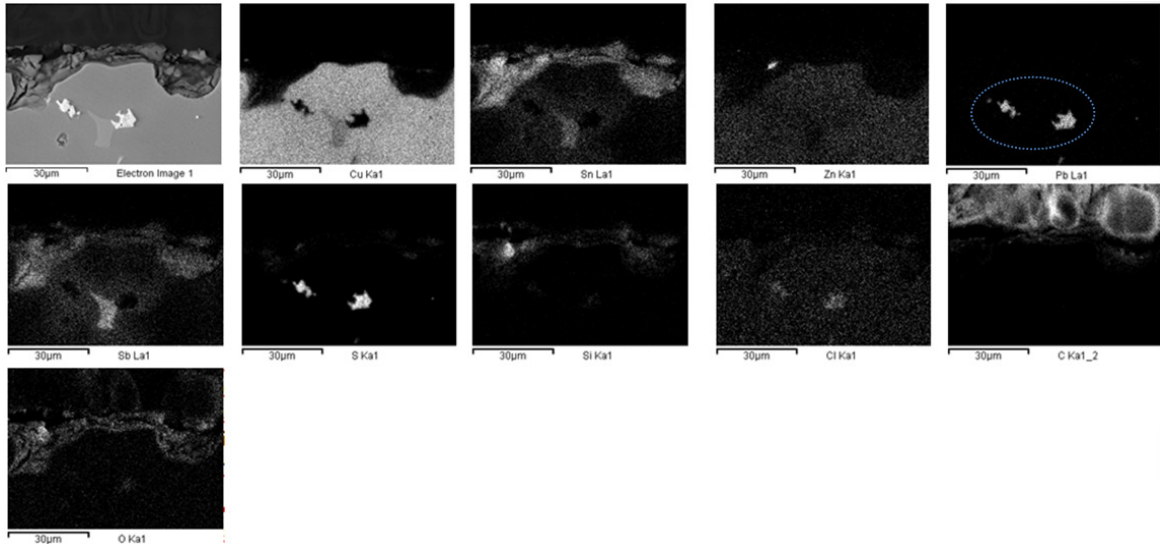
Figure 19: BSE image and X-ray maps for the different elements of interest in sample A (coated with PropS-SH)

Both elements of the inhibitor (Si and S) and of corrosion products (O and Cl) are present in the patina.

Some Pb globules (blue circle) are localized on the Cu matrix because of the fact that Pb is not soluble into the Cu-rich matrix. It is worth noting that, although these globules could be attributed also to S (due to overlapping of the S K alpha and Pb L alpha peaks), this is not the case.

Sn and the elements of the inhibitor are localized in the same areas, probably due to the ability of the silane coating to go into the porous patina.

c. Sample E: PropS-SH + TiO$_2$

- Site of interest 1
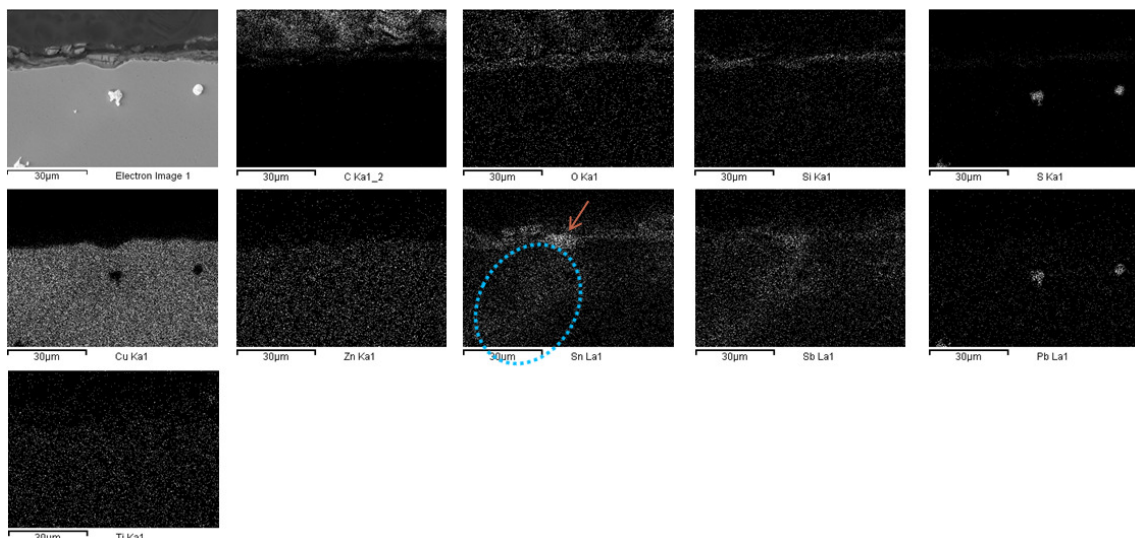
Figure 20: BSE image and X-ray maps for the different elements of interest in sample E (coated with PropS-SH+TiO$_2$)

In this site, an interdendritic Sn-rich area is evident (blue circle) with a higher amount of Sn at the top (orange arrow).

Pb globules (white dots in the BSE image), immiscible with the Cu-rich matrix, are observed (X-ray map of S is affected by the fact that the S K alpha and Pb L alpha peaks partly overlap).

- Site of interest 2
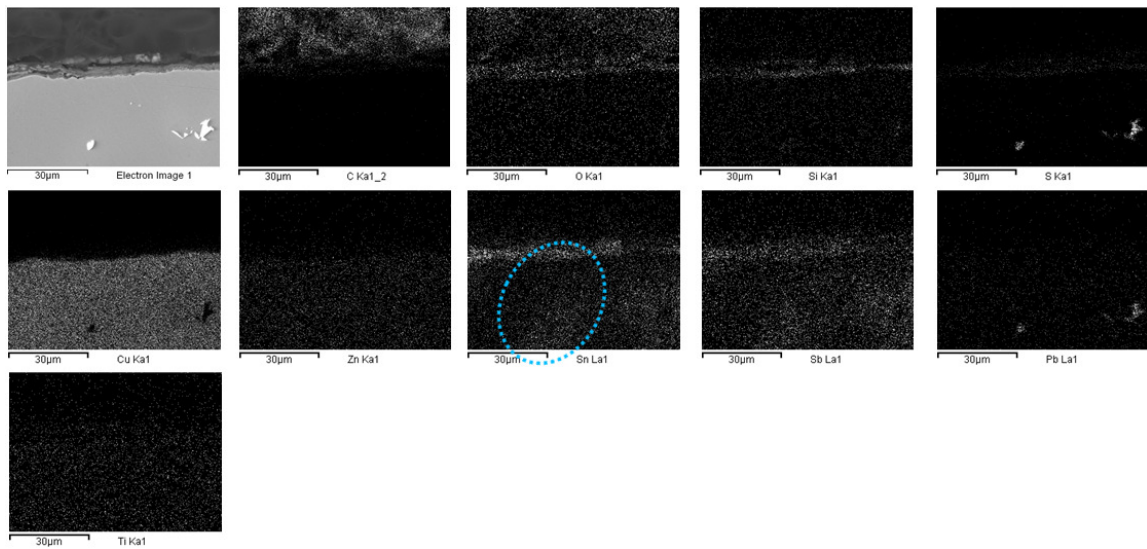
Figure 21: BSE image and X-ray maps for the different elements of interest in sample E (coated with PropS-SH+TiO$_2$)

Also in this site Pb rich globules and an interdendritic Sn-rich area (blue circle) were observed.

- Site of interest 3
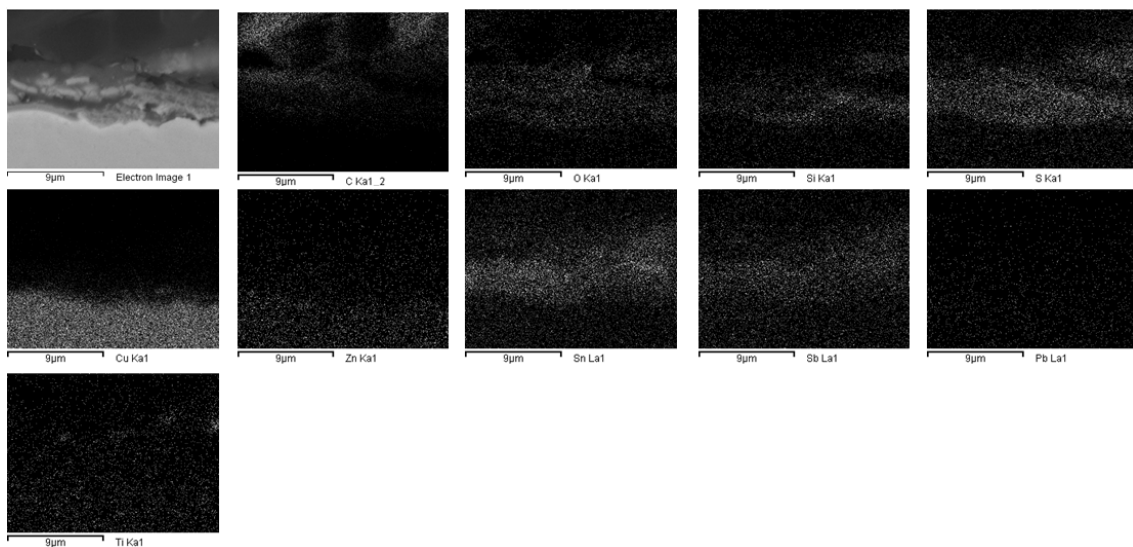
Figure 22: BSE image and X-ray maps for the different elements of interest in sample E (coated with PropS-SH+TiO$_2$)

The elements from the silane coating (Si and S) and Sn are localized in the corrosion layer. This could result from a porous patina that was impregnated by the silane coating.

- Site of interest 4
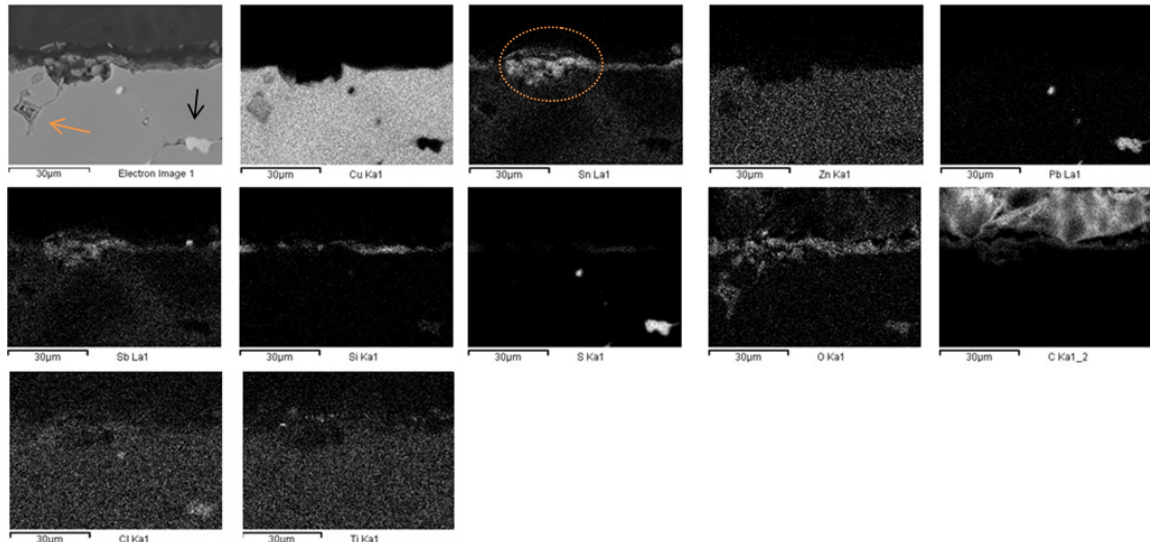
Figure 23: BSE image and X-ray maps for the different elements of interest in sample E (coated with PropS-SH+TiO₂)

A high amount of Sn is localized in the area of the patina which is connected to the Sn-rich interdendritic area (orange circle).

Pb globules can be seen on the Cu matrix (black arrow) because of the insolubility of Pb in this matrix. A signal is detected at the same place for S because Pb and S have almost the same energy thus there is an overlapping of the signals.

A shrinkage cavity (casting defect) with ah high O content is observable (orange arrow).

d. Sample F: PropS-SH + La₂O₃

- Site of interest 1
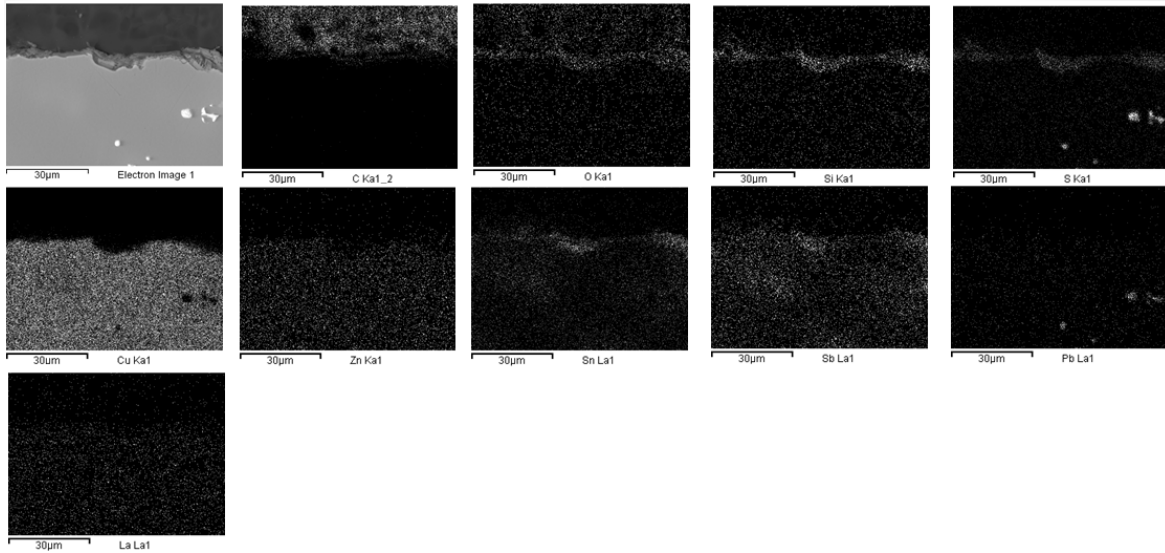
Figure 24: BSE image and X-ray maps for the different elements of interest in sample F (coated with PropS-SH+La$_2$O$_3$)

Once again, in the corrosion layer, there is the presence of Sn with also the elements of the silane coating (Si and S). Pb globules are visible in the Cu-matrix due to the fact that they are immiscible on it.

- Site of interest 2
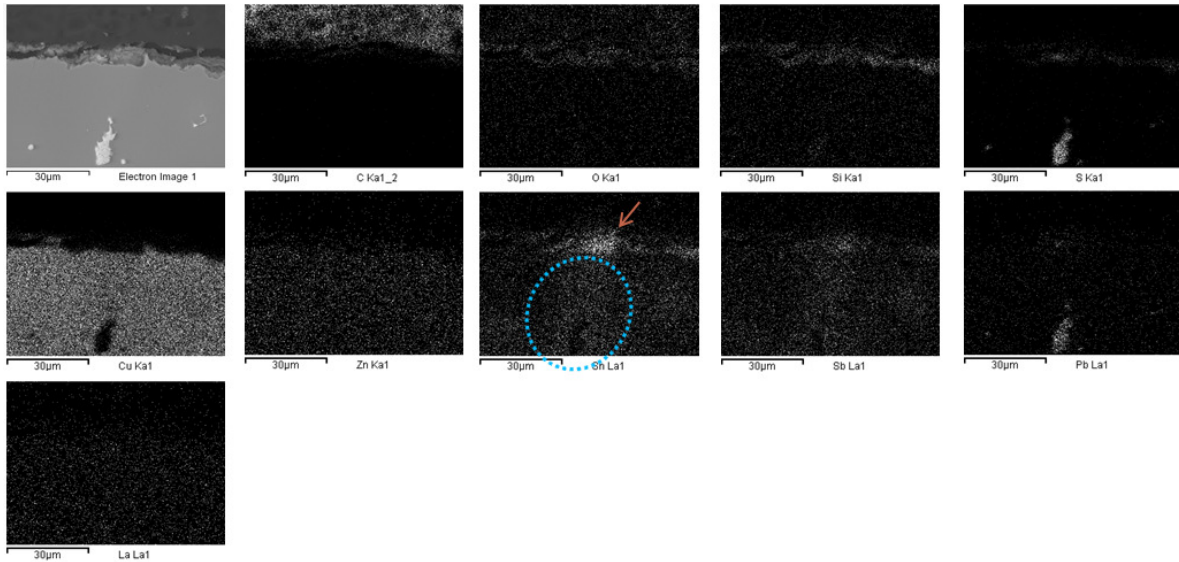
Figure 25: BSE image and X-ray maps for the different elements of interest in sample F (coated with PropS-SH+La$_2$O$_3$)

This site is characteristic of an interdendritic area Sn-rich (blue circle) with a higher amount of Sn at the top (orange arrow). Thus, according to literature [1], it can be assumed that in the corrosion layer, tin species are mainly formed over the external part of the dendrites.

Pb globules (white dots in image SEM), immiscible with the Cu-rich matrix, are also observed

- Site of interest 3
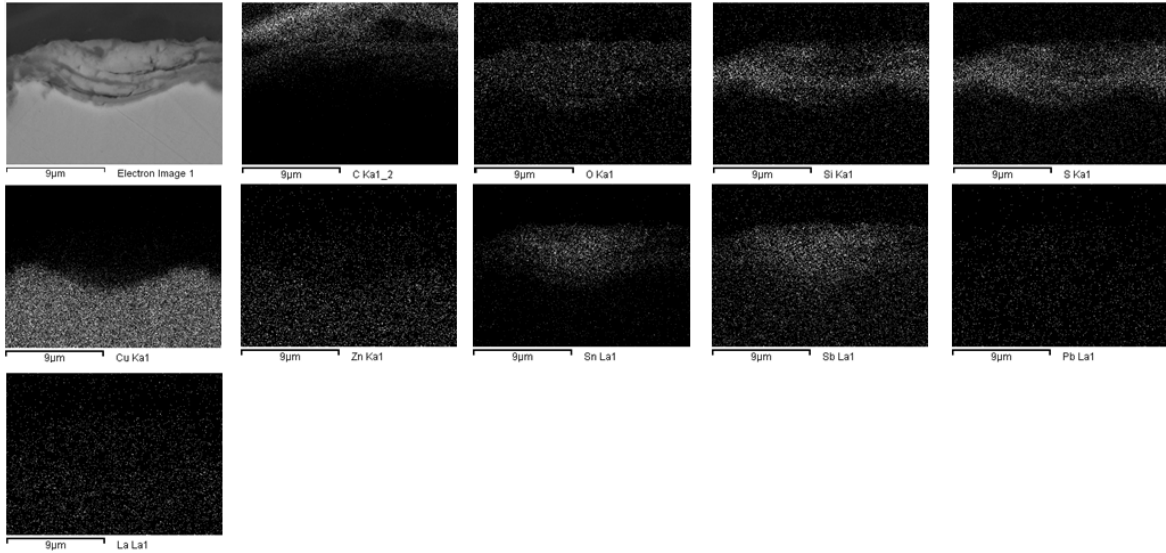
Figure 26: BSE image and X-ray maps for the different elements of interest in sample F (coated with PropS-SH+La$_2$O$_3$)

Again the elements of the silane coating (Si and S) are localized in the patina, together with Sn.

- Site of interest 4
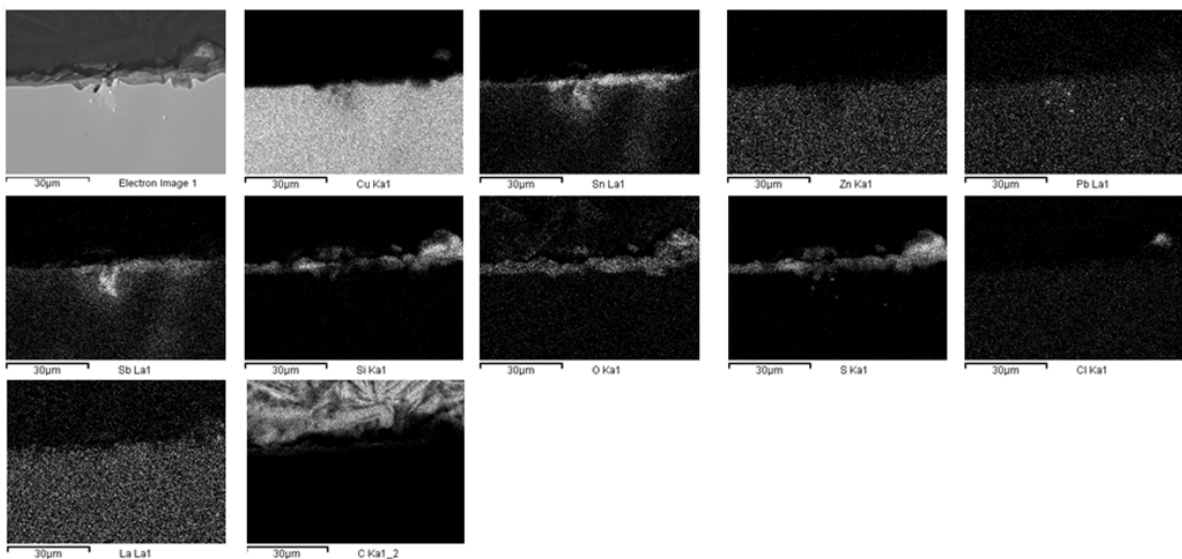
Figure 27: BSE image and X-ray maps for the different elements of interest in sample F (coated with PropS-SH+La$_2$O$_3$)

The BSE image and the maps in figure 27 show the presence of a Sn-rich area of the patina, in correspondence with an interdendritic Sn-rich area.

e. Sample G: PropS-SH + CeO₂

- site of interest 1
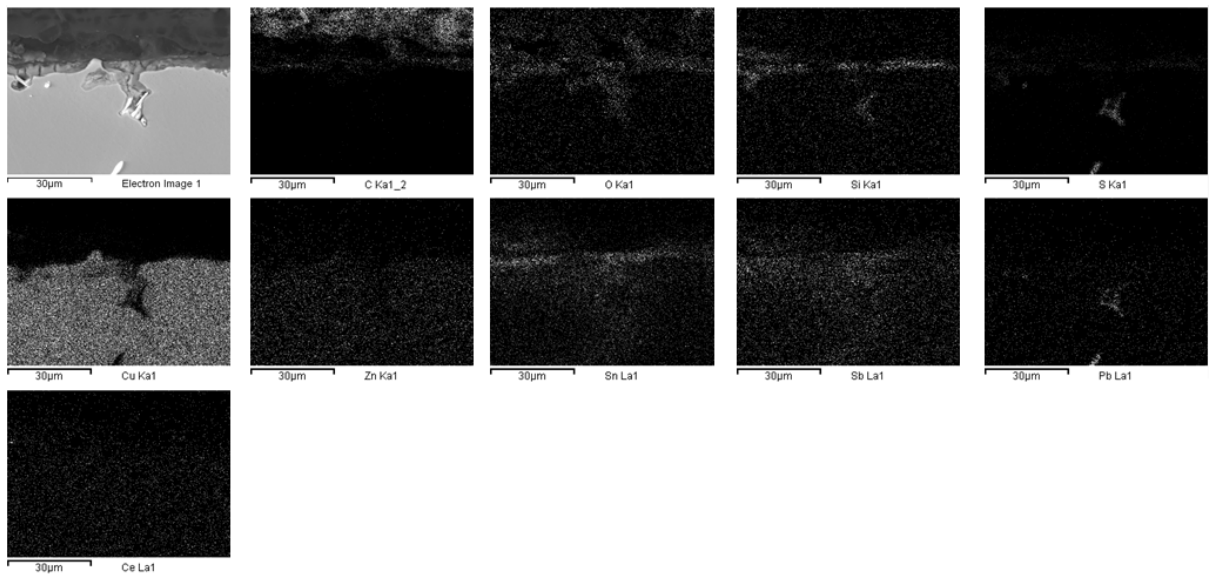
Figure 28: BSE image and X-ray maps for the different elements of interest in sample G (coated with PropS-SH+CeO₂)

This sample seems to show a characteristic form of corrosion called *pitting corrosion*. Due to the fact that there is Si (silane coating element) in the hole, this one was probably formed during the pre-patination.

- Site of interest 2
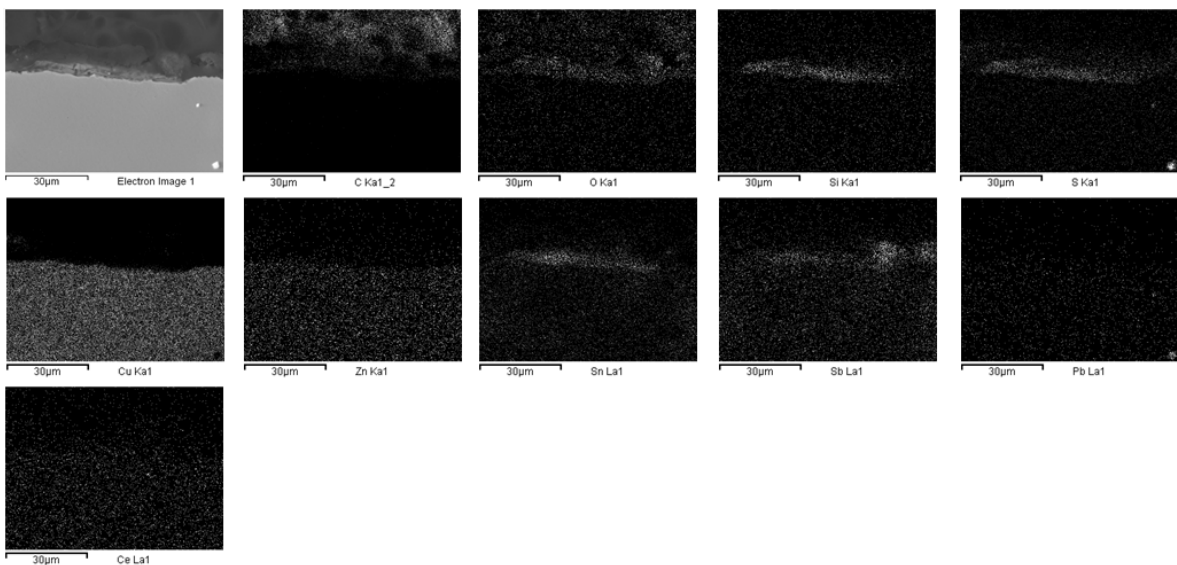
Figure 29: BSE image and X-ray maps for the different elements of interest in sample G (coated with PropS-SH+CeO₂)

In the corrosion layer we observe once more, together with Sn, inhibitor elements Si and S. Also Pb globules (white dots in the BSE image), immiscible with the Cu-rich matrix, are observable.

- Site of interest 3
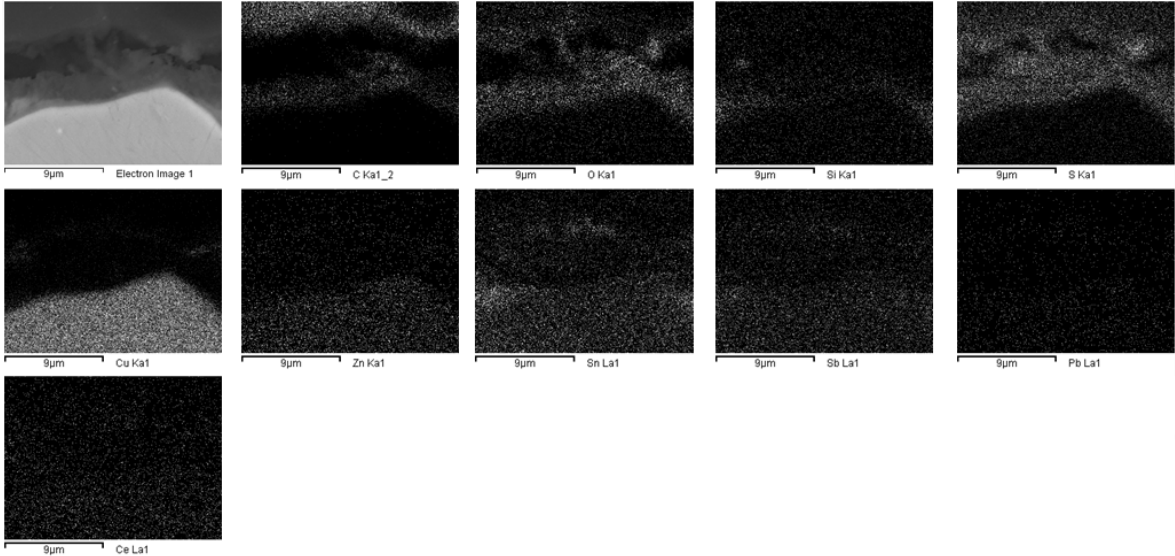
Figure 30: BSE image and X-ray maps for the different elements of interest in sample G (coated with PropS-SH+CeO$_2$)

In the corrosion layer, both the elements of the silane coating (Si and S) and Sn are in the same place. This phenomenon could be due the presence of a porous patina.

- Site of interest 4
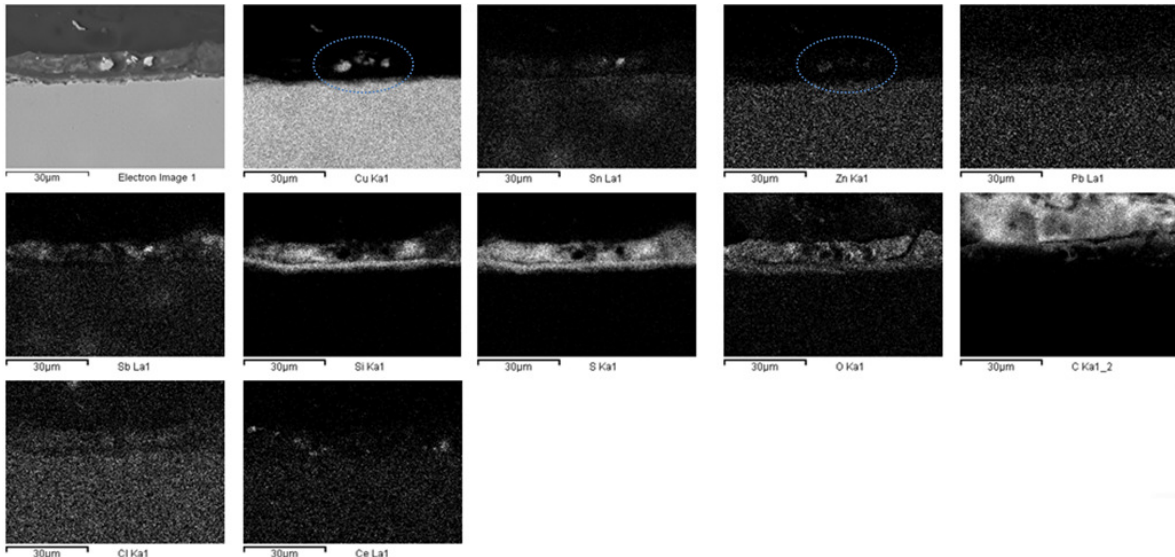
Figure 31: BSE image and X-ray maps for the different elements of interest in sample G (coated with PropS-SH+CeO$_2$)

In this site, the same comment than before can be made. The difference is that there are globules of Cu and Zn that could describe the migration of Cu and Zn cations from the metal to the corrosion layer.

1.2.4.2. SEM-EDS analysis of corroded surfaces

SEM-EDS analyses have been performed for having a morphological description of the surface of the coated samples at different steps of the study (prepatined, coated and aged).

Figure 32 shows the differences in the homogeneity of the nanoparticles into PropS-SH. While the distribution of Ti and Ce is not well defined due to the size of nanoparticles, the distribution of La shows the formation of micrometric-sized clusters.
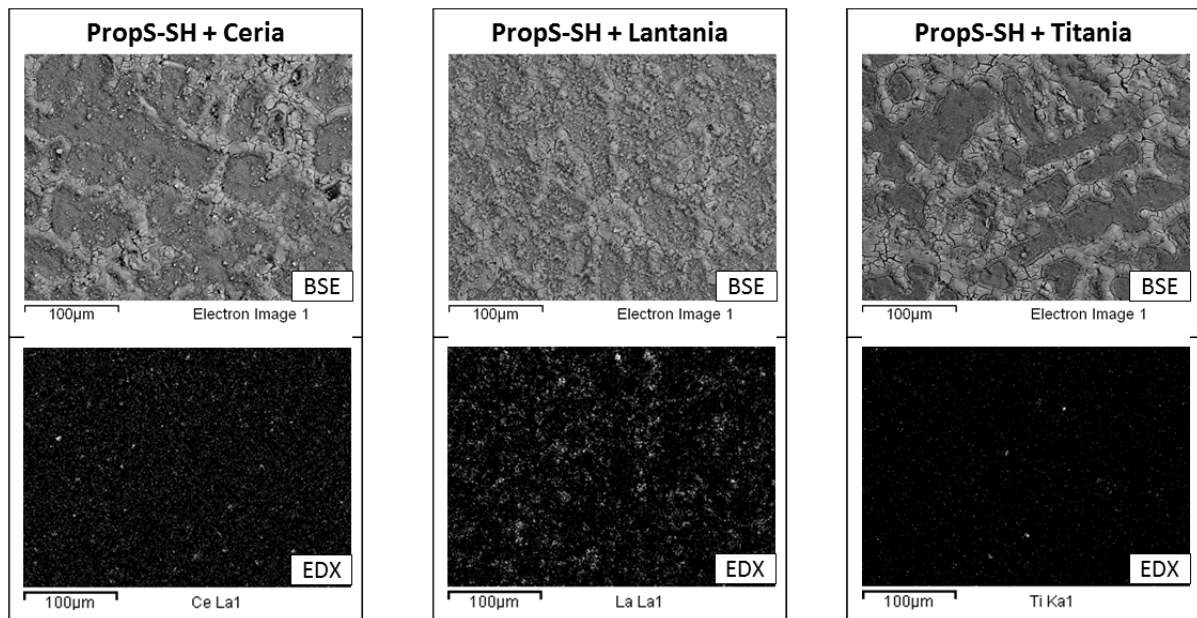
Figure 32: BSE images and X-Ray maps showing the distribution of the nanoparticles into PropS-SH (before ageing cycle)

The following tables show pictures of the surface of the coated samples at different steps of the study (prepatined, coated and aged):
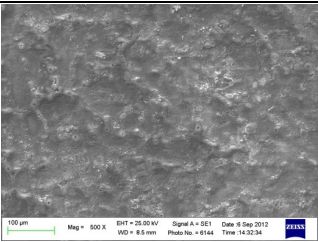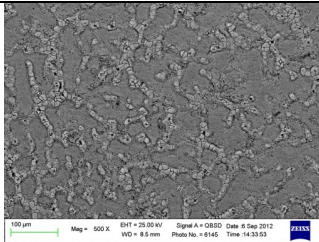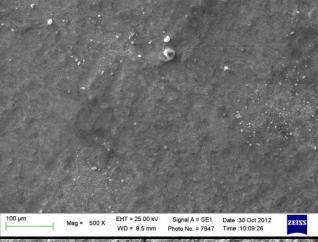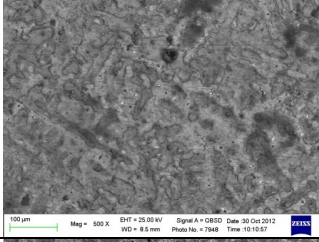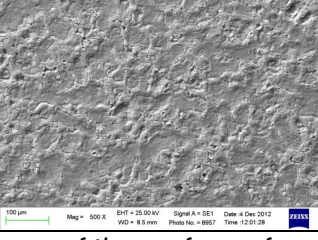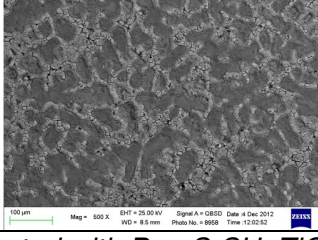
SAMPLE E		
Condition	**SE**	**BSE**
Pre-patinated		
Prepat-Coated with PropS-SH + TiO$_2$		
Prepat-Coated Ageing (10d TOW) with PropS-SH + TiO$_2$		

Table 5: SE and BSE images of the surface of sample E (coated with PropS-SH+TiO$_2$) at different steps of the study (prepatined, coated and aged)
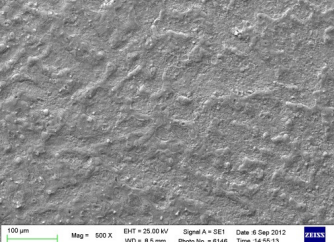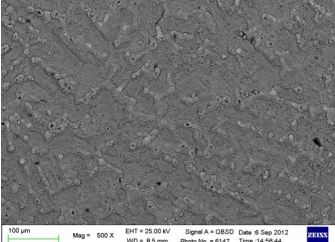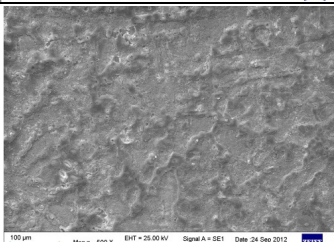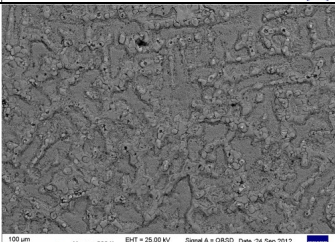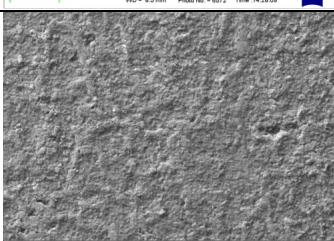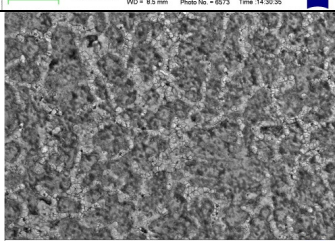
SAMPLE F		
Condition	**SE**	**BSE**
Prepatinated		
Prepat-Coated with PropS-SH + La$_2$O$_3$		
Prepat-Coated Ageing (10d TOW) with PropS-SH + La$_2$O$_3$		

Table 6: SE and BSE images of the surface of sample F (coated with PropS-SH+La$_2$O$_3$) at different steps of the study (prepatined, coated and aged)
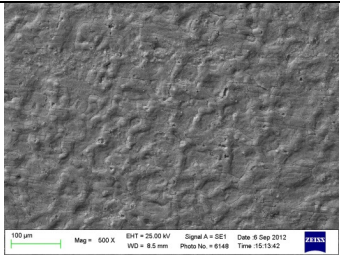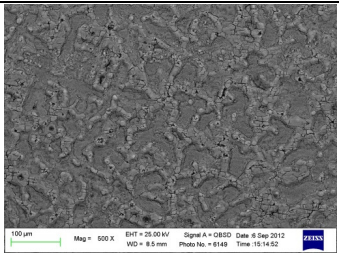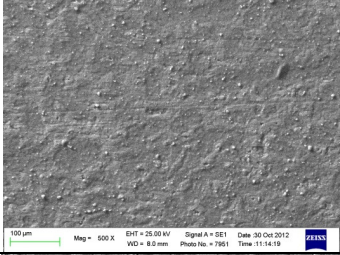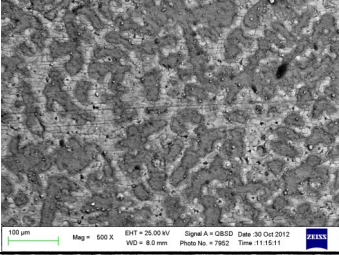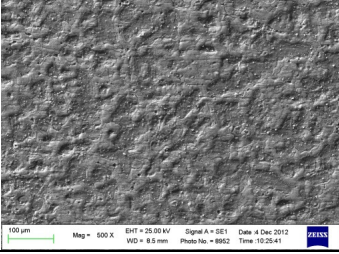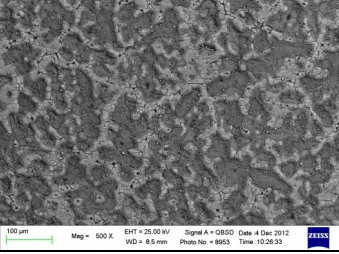
SAMPLE G		
Condition	**SE**	**BSE**
Prepatinated		
Prepat-Coated with PropS-SH + CeO$_2$		
Prepat-Coated Ageing (10d TOW) with PropS-SH + CeO$_2$		

Table 7: SE and BSE images of the surface of sample G (coated with PropS-SH+CeO$_2$) at different steps of the study (prepatined, coated and aged)
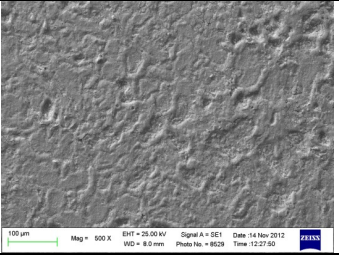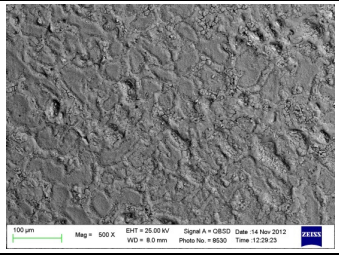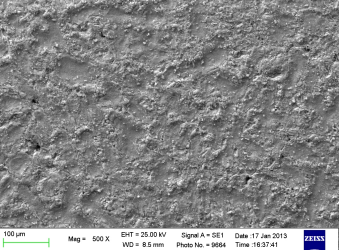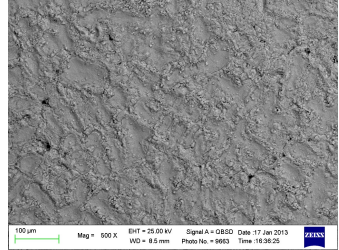
Sample H		
Condition	**SE**	**BSE**
Prepatinated (31d TOW)		
Ageing (10d TOW)		

Table 8: SE and BSE images of the surface of sample H (without coating) at different steps of the study (prepatined, coated and aged)

By making a comparison between the different steps, it can be concluded that the protective silane coating covers the surface of the pre-patinated sample without hiding the typical morphology of the pre-patinated surface (in which the leaching action of the rain highlighted the cored microstructure, due to decuprification of the dendrite core

55

[58]). After 10d TOW of ageing test, the morphology of the protected surfaces does not change significantly.

Table 9 shows the average composition of the surface (EDS, mass %) in areas corresponding to the previous pictures:

Element	sample H (uncoated)	
wt%	prepat. (31d TOW)	Ageing (10d TOW)
C	/	9.25
N	/	2.96
O	26.29	24.11
Al	/	/
Cl	0.26	0.21
Cu	**54.26**	**45.22**
Zn	/	**0.58**
Sn	**18.15**	**18.52**
Pb	**0.88**	**1.09**
Sb	/	0.62
S	0.16	/
Si	/	/

Table 9: SEM-EDS results for the Uncoated sample

Element	Sample A (PropS-SH)		
wt%	Prepat. (24d TOW)	Coat. Prepat. PropS-SH (0d TOW)	Coat. Prepat. PropS-SH (10d TOW)
C	5.7	10.7	9.2
N	/	2.5	/
O	23.9	21.4	25.7
Al	0.5	/	/
Cl	0.3	0.2	0.2
Cu	**48.7**	**44.5**	**36.5**
Zn	**0.8**	**0.5**	**0.6**
Sn	**17.1**	**12.4**	**17.9**
Pb	**1.5**	/	**0.9**
Sb	2.6	2.0	2.3
S	**0.2**	**3.8**	**3.4**
Si	/	**3.8**	**3.2**

Table 10: SEM-EDS results for the sample coated with PropS-SH

Element	sample E	sample E +TiO2	sample E +TiO2	sample F	sample F + La2O3	sample F + La2O3	sample G	sample G + CeO2	sample G + CeO2
wt%	Prepat.	Coat .prep	Ageing coat. prep	Prepat.	Coat. prep	Ageing coat. prep	Prepat.	Coat. prep	Ageing coat. prep
C	3.925	15.4	11.55	6.77	13.13	12.33	5.06	15.23	11.9
N	/	/	/	/	/	/	2.92	/	/
O	23.17	24.68	24.81	21.97	31.88	23.14	23.97	27.98	27.97
Al	0.31	0.26	0.2	0.3	/	0.11	0.21	/	/
Si	/	**6.79**	**6.04**	/	**5.86**	**7.77**	/	**6.23**	**6.11**
S	/	**6.52**	**5.98**	0.22	**6.57**	**7.34**	/	**6.16**	**6.3**
Cl	0.22	0.21	/	0.23	/	/	0.2	0.15	/
Cu	**53.77**	**32.32**	**38.93**	**53.24**	**21.94**	**34.76**	**49.35**	**28.3**	**29.85**
Zn	**0.9**	/	/	**0.77**	/	**0.06**	**0.79**	/	/
Sn	**16.64**	**11.79**	**15.9**	**16.26**	**14.63**	**14.13**	**18.28**	**13.69**	**16.84**
Sb	**0.67**	**1.43**	/	/	**1.56**	**1.38**	**0.69**	**1.65**	/
Pb	**1.06**	**0.17**	**0.06**	**0.93**	**0.43**	/	**1.08**	**0.2**	**0.04**
La	/	/	/	/	4.01	0.09	/	/	/
Ce	/	/	/	/	/	/	/	1.07	1,00
Ti	/	0.46	0.42	/	/	/	/	/	/

Table 11: SEM-EDS results for the samples coated with PropS-SH + nanoparticles at different steps of the study (prepatined, coated and aged)

By comparing the concentration of the typical elements from the protective silane coating (Si and S) before and after ageing test (Table 11), we can see that, in samples E and G, the amount of Si and S does not decrease significantly after exposure, which means that the coating+nanoparticles layers were not damaged by exposure. The increase of Si and S for the sample F is probably due to the fact that EDS analysis was made in different areas before and after exposure, and also the non-homogeneous distribution of La_2O_3 particles, compared to TiO_2 and CeO_2 (see Figure 32), could have affected the results.

If we consider the alloying elements as indicators of the evolution of corrosion in the exposure step, in the case of the uncoated sample (Table 9), the amount of Cu decreases with increasing exposure time, while the amount of Sn increases. This is due to the typical Sn enrichment of the surface, which occurs because of the depletion of Cu and Zn [1].

In the case of protected samples (Table 11), the increase of Sn concentration on the surface, which is indicative of ongoing corrosion, can be observed more clearly in the case of PropS-SH+CeO_2 and PropS-SH+TiO_2, whilst it is less noticeable in the case of PropS-SH+La_2O_3, in agreement with metal release data and IE% values (Table 4).

According to the results, we cannot discuss the effect of the addition of nanoparticles to the silane coating concerning the efficiency of PropS-SH to slow the corrosion process. Moreover, there are not clear differences on surface compositions between the silane layers with the three different nanoparticles due to the non-homogeneous nature of the surface.

Details about the surface composition on the micro-scale, differentiating between core and periphery of dendrites, are shown in the following figures.

SEM images of the surfaces (analyzed at the end of the ageing test (10d TOW)) and the corresponding tables, giving the mass percentage of each element in the analyzed areas, are reported below:

Elements % in mass	Spectrum 1	Spectrum 2	Spectrum 3	Spectrum 4
C	-	8.84	-	-
N	-	-	-	-
O	17.97	20.34	29.30	27.65
Al	-	-	-	0.18
Si	6.74	6.78	3.39	4.35
S	5.80	5.97	4.01	4.66
Cl	0.36	0.32	-	-
Zn	-	-	-	-
Cu	61.93	51.83	14.17	35.05
As	-	-	-	-
Sn	6.79	5.40	45.64	27.00
Sb	-	-	-	-
Pb	-	-	2.76	0.62
Ce	0.40	0.52	0.73	0.50
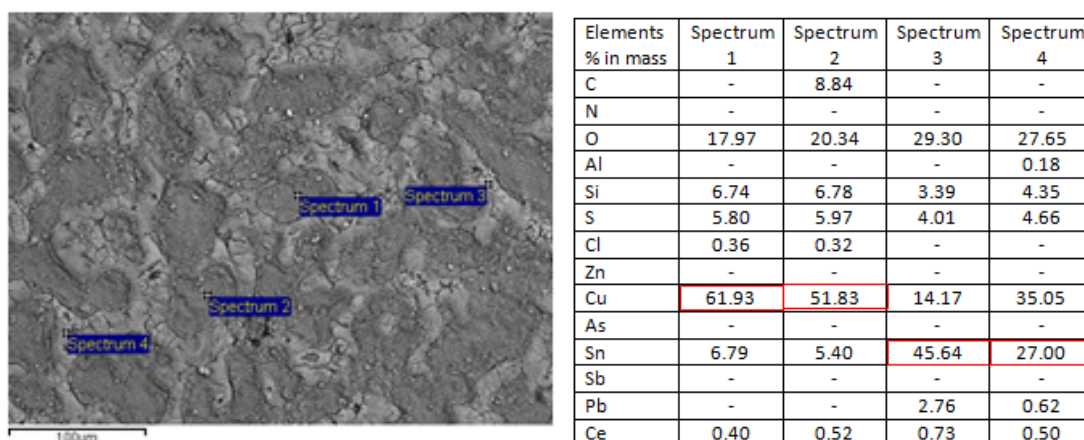
Figure 33: Sample G (coated with PropS-SH+CeO_2) inhibited and aged (10d TOW)
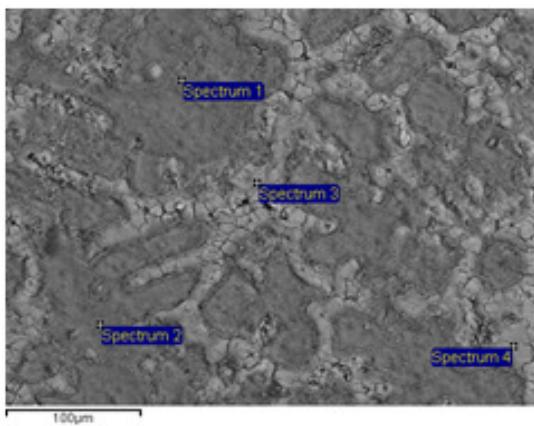
Elements % in mass	Spectrum 1	Spectrum 2	Spectrum 3	Spectrum 4
C	-	5.91	-	-
N	-	-	-	-
O	19.06	18.13	15.09	21.33
Al	-	-	-	-
Si	8.84	7.39	2.51	3.51
S	8.09	6.88	2.42	3.86
Cl	0.34	0.42	0.22	-
Zn	-	-	0.74	0.39
Cu	51.72	54.16	66.94	47.40
As	-	-	-	-
Sn	11.95	7.11	11.63	22.99
Sb	-	-	-	-
Pb	-	-	0.44	0.52
Ti	-	-	-	-

Figure 34: Sample E (coated with PropS-SH+TiO$_2$) inhibited and aged (10d TOW)
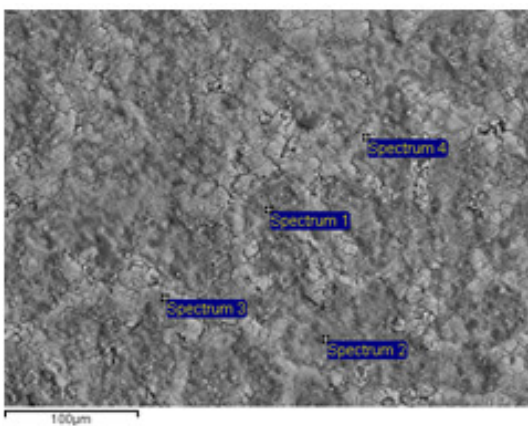
Elements % in mass	Spectrum 1	Spectrum 2	Spectrum 3	Spectrum 4
C	13.49	10.73	7.57	-
N	-	-	-	-
O	22.75	16.65	31.79	28.50
Al	-	-	3.38	-
Si	9.23	7.76	5.44	5.53
S	8.20	5.82	5.37	7.05
Cl	-	0.26	-	-
Zn	-0.01	-	-	-
Cu	32.76	55.36	20.58	21.24
As	-	-	-	-
Sn	13.57	3.43	25.87	37.11
Sb	-	-	-	-
Pb	-	-	0.01	0.58
La	-	-	-	-

Figure 35: Sample F (coated with PropS-SH+La$_2$O$_2$) inhibited and aged (10d TOW)

For each sample, different sites of interest were analyzed with the purpose to make comparisons between the different areas.

For the three samples coated with nanoparticle-additivated silane, the SEM-EDS analysis highlights the differences between dendritic and interdendritic areas. Dendritic areas always show a higher amount of Cu, whilst a higher amount of Sn was detected in the interdendritic areas, due to microsegregation during solidification of the alloy. The periphery of dendrites is a high-relief area due to the formation of insoluble Sn-rich compounds which hinder alloy dissolution, whilst decuprification of dendrite core leads to material removal (low-relief area) [58]. Higher values of silane-related elements (Si and S) are usually measured in the low-relief core of dendrites, whilst lower amounts of Si and S are detected in the high-relief periphery of dendrites, where also Pb is present. This probably accounts for the higher metal release of Pb (less protected due to its location in interdendritic areas, where a thinner layer of protective coating is present), as discussed in the previous section.

1.2.4.3. µ-Raman analysis

A Raman analysis was done on bare bronze sample coated with PropS-SH with the purpose to have a Raman spectrum of PropS-SH as reference. This was useful for interpreting the results about Raman analysis which we done, at the end of ageing test (10d TOW), on samples coated with PropS-SH containing different oxide particles.

Raman spectrum in Figure 36 shows the main peaks of PropS-SH.
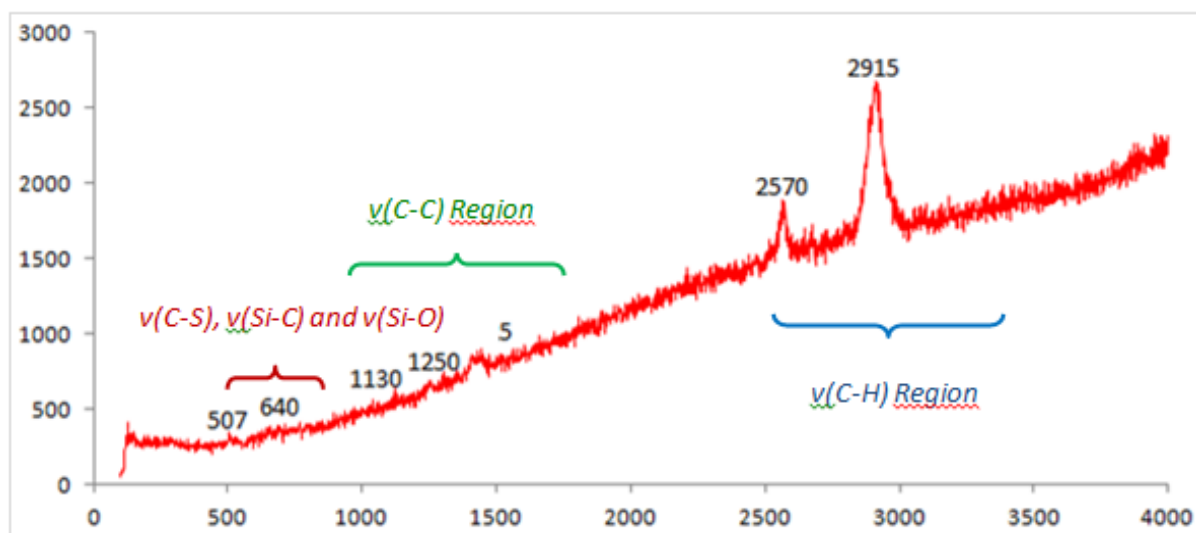
Figure 36: Raman spectrum of PropS-SH (used as a reference)

On table 12, only one representative spectrum and the picture of its corresponding analyzed area are reported for each sample.
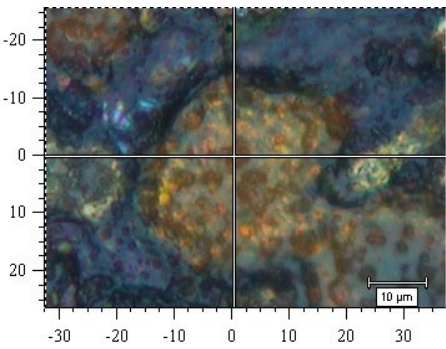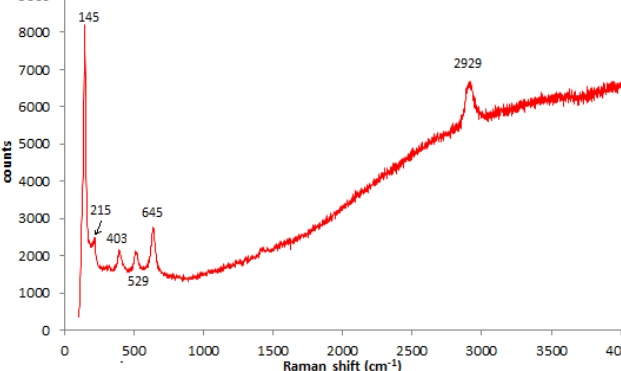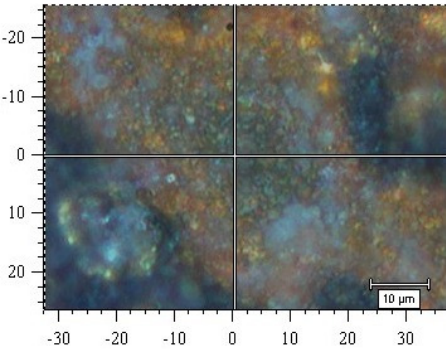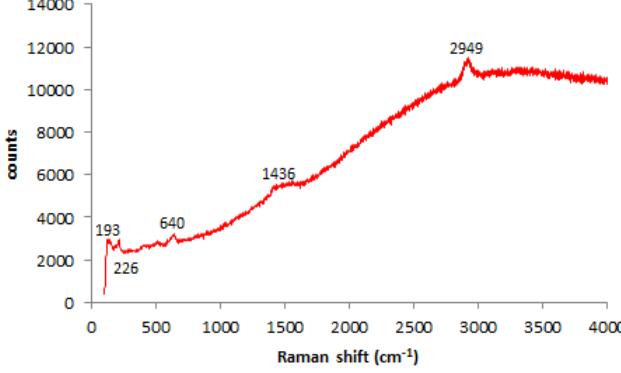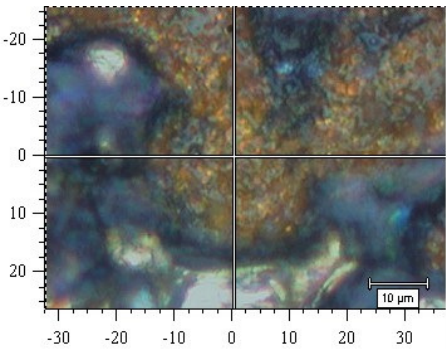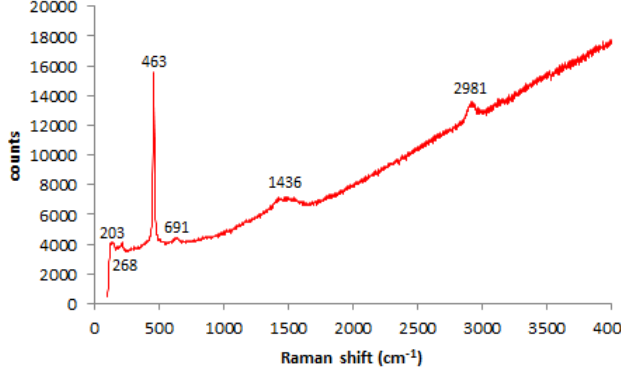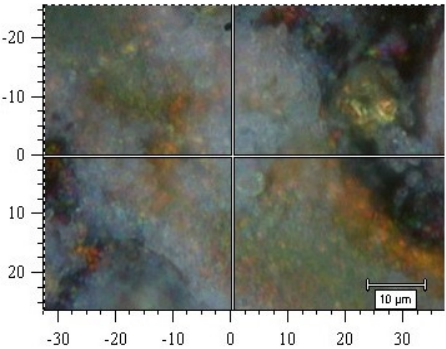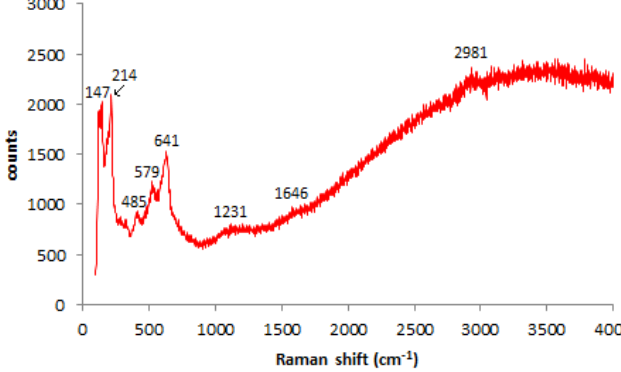
Sample name	Picture of the area	Raman spectrum + compound name
E + TiO$_2$		Anatase + cuprite + PropS-SH
F + La$_2$O$_3$		Cuprite + PropS-SH
G + CeO2		Cuprite + PropS-SH + cerium oxide
H		Cuprite + amorphous carbon

Table 12: Raman spectra of the different samples at the end of exposure test (10d TOW)

In all spectra, the presence of cassiterite cannot be confirmed due to the fact that there are no evident peaks or broad bands which could be assigned to SnO_2.

Usually, when the Raman spectrum is collected in a Sn-rich area, it shows a broad band at ~560/580 cm^{-1} that can be assigned to a surface mode of SnO_2 nanocrystals. In other cases there is a peak ~630 cm^{-1} and a peak around 780 cm^{-1} too.

For each sample, it appears that the corrosion products resulting from Cu (cuprite Cu_2O) give the main contribution to Raman spectra.

Concerning the spectrum of sample E (coated with PropS-SH + TiO_2), the Raman spectrum shows the presence of anatase [59], that is one of the polymorphs of TiO_2.

In the case of sample G, the sharp peak at 463 cm^{-1} can be assigned to cerium (IV) oxide (CeO_2) [60].

As samples E, F and G contain PropS-SH, which is an organic compound, multiple peaks are present in the upper part of the spectrum, over 1000 cm^{-1}, which correspond to the fingerprint of the silane coating.

In the case of sample H, also peaks in the organic part of the spectrum appear. However they cannot be assimilated to PropS-SH due to the fact that sample H is not coated with inhibitor. The peaks at 1231 cm^{-1} and 1646 cm^{-1} are characteristic of the Raman spectrum of amorphous carbon [61].

1.2.4.4. XRD analysis

X-Ray Diffraction measurements were made on samples for having a more complete description of samples by obtaining a general picture of the surfaces.

Table 13 is a summary of the corrosion products detected by XRD on each sample at the end of the ageing test (10d TOW).

Corrosion product	Sample H (without inhibitor)	PropS-SH	PropS-SH + CeO$_2$	PropS-SH + La$_2$O$_3$	PropS-SH + TiO$_2$
Cuprite (Cu_2O)	+	+	+	+	+
Litharge (PbO)	-	-	+	-	-

Table 13: Corrosion products detected by XRD at the end of exposure test (10d TOW) (+) detectable; (-) not detectable

The main corrosion product detected is cuprite, which is present in all samples.

The sample coated with PropS-SH + CeO_2 is the only one that showed presence of litharge (PbO). This is probably due to surface conditions (Pb was smeared on the

surface during polishing). In that case, compounds containing Pb cannot be related to corrosion during the accelerated ageing test.

1.2.5. Color measurement

The goal of conservation of bronze monuments is to find an inhibitor/coating that will slow down the corrosion process without changing the aspect and the color of the surface.

Color measurements are therefore necessary for determining if the color changes or not after applying the protective coating on the surface.

Table 14 and table 15 show the results of the color measurements before and after ageing of the sample.

Pre-ageing (0d TOW)	ΔG	ΔE
PropS-SH + CeO_2	3,9±0,8	14,6±2,4
PropS-SH + La_2O_3	0,6±0,3	12,0±3,3
PropS-SH + TiO_2	6,1±1,3	15,1±2,5

Table 14: Comparison of aesthetical parameters in the dropping test before ageing of the samples
ΔG (=$\Delta Gloss$) is a data about the brightness of the surface whereas ΔE is about color variation.

Post-ageing (10d TOW)	ΔG	ΔE
Uncoated	0,7±0,1	8,4±2,3
PropS-SH + CeO_2	0,6±1,0	1,0±2,2
PropS-SH + La_2O_3	0,3±0,6	1,8±2,6
PropS-SH + TiO_2	-1,9±1,2	0,5±2,0

Table 15: Comparison of aesthetical parameters in the dropping test after ageing of the samples; the non-inhibited, pre-patinated bronze is taken as reference for comparison.
ΔG (=$\Delta Gloss$) is a data about the brightness of the surface whereas ΔE is about color variation.

Concerning results about ΔG we can affirm that the application of coating has an impact on the brightness of the samples, mainly for PropS-SH + TiO_2, (table 14) but this effect disappears after ageing test (table 15).

There is also a quite important color variation due to the application of the silane layer. The perceptibility threshold in Cultural Heritage materials is $\Delta E \leq 3$, thus the coating changes significantly the color of the patina, already before ageing test (table14) However, the coating is able to preserve the color during ageing test (table15) because ΔE decreases drastically. In fact, this decrease shows that the coating protects the patina after ageing thus it keeps its color instead of changing due to corrosion products that would form on the patina if there was no coating.

As regards PropS-SH without nanoparticles [58], the application of the protective coating did not change significantly the color of the patinated surface (differently from PropS-SH with nanoparticles) and was able to preserve the color during ageing test (similarly to PropS-SH with nanoparticles).

1.3. Accelerated corrosion test: concluding remarks

Quaternary bronze samples were aged by the dropping test, which simulates the action of leaching rain in unsheltered areas of outdoor monuments. After the production of the patina by ageing ("pre-patination"), the influence of different treatment conditions (uncoated or coated by a protective silane layer, additivated by different oxide particles) was investigated.

By analyzing cross sections of the samples, it appears that specific corrosion processes (for example: intergranular and pitting corrosion) are present in the uncoated sample but not in the coated ones. The silane layer impregnates the patina, which shows the typical Sn enrichment due to decuprification, and slows down the corrosion process.

The influence of the addition of nanoparticles to PropS-SH was studied using different spectroscopic analyses. There are not significant differences between the samples in terms of surface features (apart from a slight differentiation in the extent of Sn enrichment), but the gravimetric measurements and the inhibiting efficiency values (in terms of metal release in the ageing solutions) highlighted that the addition of nanoparticles increases the protective efficiency by comparison to PropS-SH, and PropS-SH + La_2O_3 gives the best results.

Section 2

STUDY OF THE EFFICIENCY OF PROTECTIVE TREATMENTS FOR GILDED BRONZES BY ACCELERATED CORROSION TEST

2.1. Accelerated corrosion test

For studying the efficiency of the candidate protective treatments for gilded bronzes without damaging the original artworks, accelerated ageing tests were carried out on representative samples. The same exposure test described in section 1 (dropping test) was used also for gilded bronzes, in the same ageing conditions. Moreover, the same silane coating as in section 1 was tested in order to study its efficiency on gilded bronzes. The addition of nanoparticles to the silane coating was also investigated but only for CeO_2 nanoparticles.

2.1.1. Tested material: quaternary gilded bronze and organic coating (PropS-SH + nanoparticles)

For the study concerning gilded bronzes, we used gilded samples (manufactured by the goldsmith A.Pacini of Montepulciano (SI)), which reproduce the gilded bronze of the Paradise Door. The alloying elemental composition of the bronze substrate is listed in Table 1.

	Cu	Sn	Zn	Pb	Sb
Weight%	91.9	2.4	2.9	1.0	0.8

Table 1: alloying composition of the samples reproducing the bronze substrate of the Paradise Door of the Baptistery in Florence

A summary of the development of this test is shown in table 2.

sample	Protective coating	Ageing by dropping test
Uncoated	none	10d TOW
PropS-SH	PropS-SH	10d TOW
PropS-SH + CeO_2	PropS-SH + CeO_2	10d TOW

Table 2: sample description

Figure 2 shows the surface appearance of the gilded bronzes before and after ageing. Unlike non-gilded bronzes, gilded bronzes do not show a noticeable difference of the surface after ageing. This is due to the fact that, in short term exposure, the corrosion products might mostly grow at the interface between the two metals.

Ageing time	Uncoated	Coated Prepatinated PropS-SH	Coated Prepatinated PropS-SH + CeO$_2$
(0d TOW)			
(10d TOW)			

Figure 2: sample surfaces of gilded bronzes at different ageing times
TOW = time of wetness

2.2. Results

For studying the efficiency of the silane coating on gilded bronzes, various techniques have been used. In this part are reported the results.

2.2.1. Gravimetric measurements

Gravimetric measurements were recorded at different ageing time during the dropping test, with the purpose to observe the mass variations during ageing. Results are shown in Table 3.

TOW (d)	Mass variation (g) Sample: Uncoated	Mass variation (g) Sample: PropS-SH	Mass variation (g) Sample: PropS-SH+CeO$_2$
2	0,000	0,016	0,000
5	-0,001	0,001	0,000
8	-0,003	-0,003	-0,004
10	-0,003	-0,003	-0,004

Table 3: mass variation of the samples during dropping test; TOW: time of wetness

During the dropping test, which finished at 10d TOW, no significant change in the mass of the samples occurred. Thus the behaviors of the uncoated sample and the coated ones are similar.

However, compared to the other samples, the sample coated with PropS-SH shows a slight increase after 2 days of TOW. This could be due to growth of corrosion products prevailing on the leaching action of the rain. Or, more likely, also the significant porosity of the gold layer might have made difficult to achieve complete drying of the sample.

2.2.2. Ageing solutions: Atomic Absorption Spectroscopy

During the dropping test, ageing solutions were collected in order to determine the concentration of released metals by Atomic Absorption Spectroscopy (AAS).

Figure 4 reports the cumulative release of copper as a function of TOW (time of wetness) for all the samples.
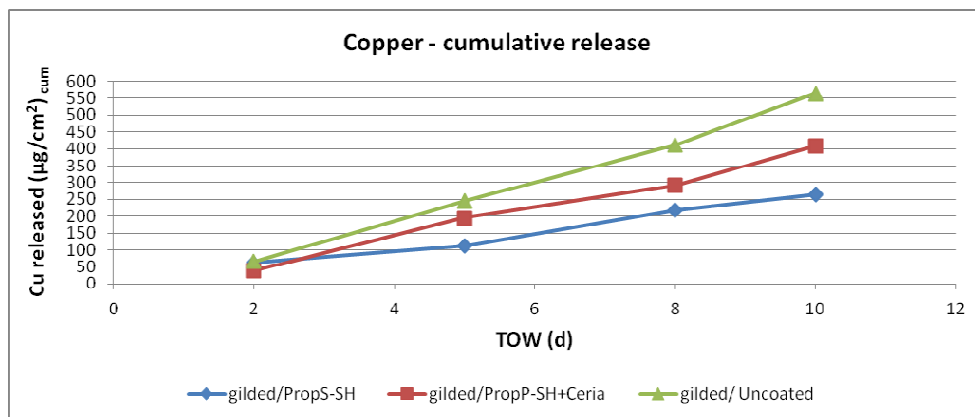
Figure 4 : cumulative release of copper for a cycle of 10d TOW by dropping test

According to figure 4, the amount of copper released into the acid rain solution is lower in the case of coated samples. Thus, the presence of coating on surface of gilded bronze is effective in reducing the amount of copper released into the acid rain solution, as already observed also for non-gilded bronzes, aged in the same conditions (described in section 1).

Moreover, the copper release is lower for the gilded sample coated with PropS-SH without nanoparticles than the one coated with PropS-SH+CeO$_2$. Thus the addition of nanoparticles to the silane coating does not seem to contribute to decrease the metal release from the gilded bronze.

2.2.3.   XRD analysis

XRD analysis was run on the uncoated sample at the end of dropping test (10d TOW) for examining the possible presence on the surface of corrosion products. The same conditions as in section 1 were used for acquiring the XRD pattern.

Figure 5 shows the XRD pattern obtained for the uncoated gilded sample after exposure (a). In Fig. 5b the XRD patterns of the uncoated gilded sample are compared before and after exposure, showing that cuprite is the only corrosion product which was found after exposure. Moreover the low intensity of its most intense peak suggests that cuprite is present in a small amount.
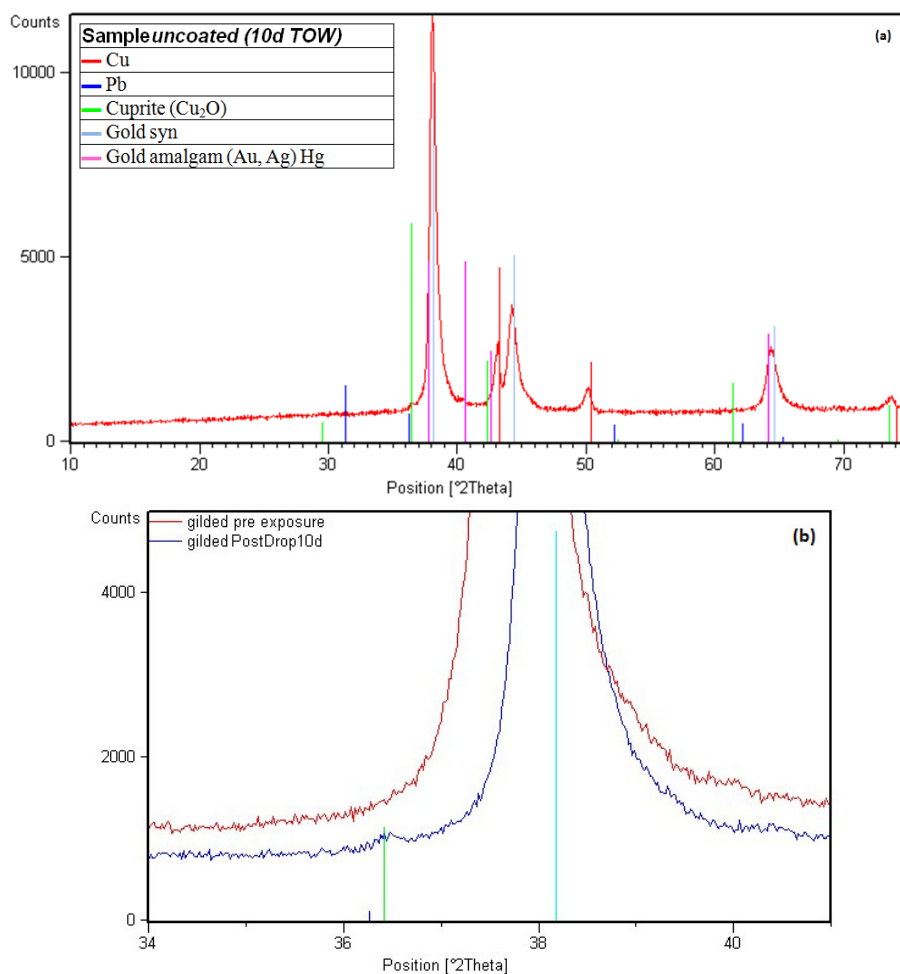
Figure 5: (a) XRD pattern of the uncoated gilded sample after ageing by dropping test (10d TOW) and (b) comparison of XRD patterns for the gilded samples before (red line) and after (blue line) exposure.

The other phases found during the experiment are Cu, Pb, Au and the Au-Hg amalgam. For a more detailed characterization of aged surfaces, SEM-EDS was used.

2.2.4. Characterization of corroded surfaces: SEM-EDS

2.2.4.1. SEM-EDS analysis

SEM-EDS analyses were carried out for characterizing the surface morphology of the samples and obtaining the elemental compositions of each surface before and after accelerated ageing tests.

Table 4, 5 and 6 show SE and BSE pictures of the surface of each sample before and after ageing.
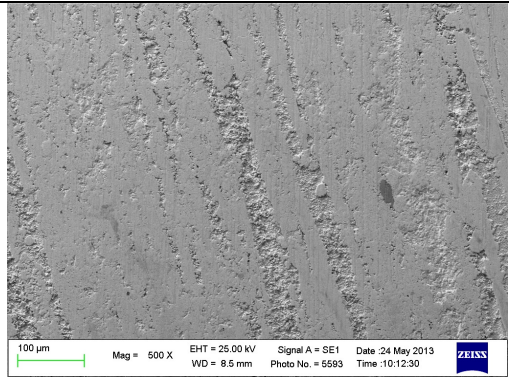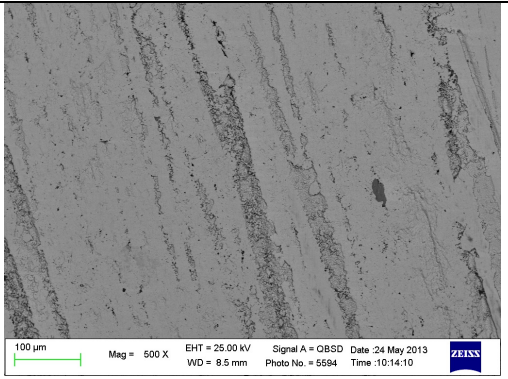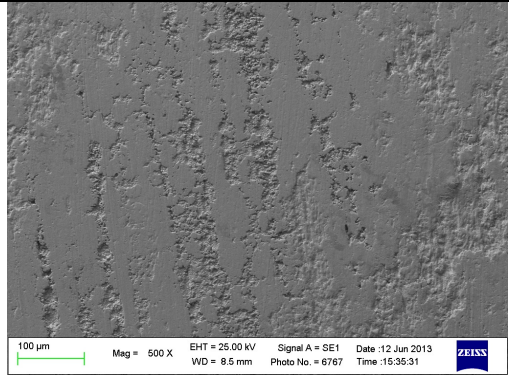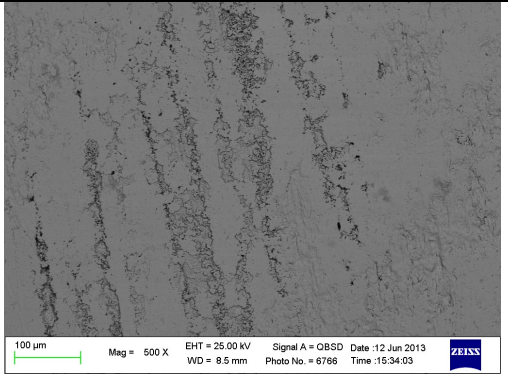
Uncoated		
condition	SE	BSE
Before ageing 0d TOW		
After ageing 10d TOW		

Table 4: SE and BSE images of the surface of gilded sample uncoated,at different time of ageing
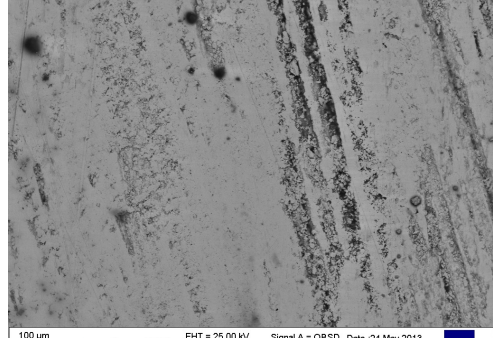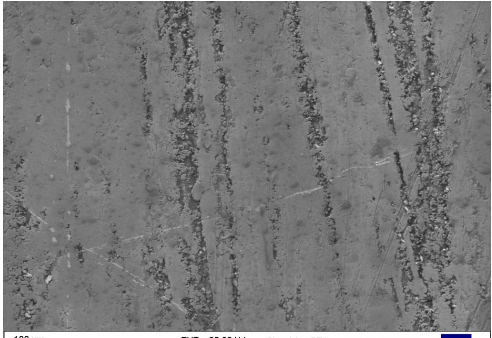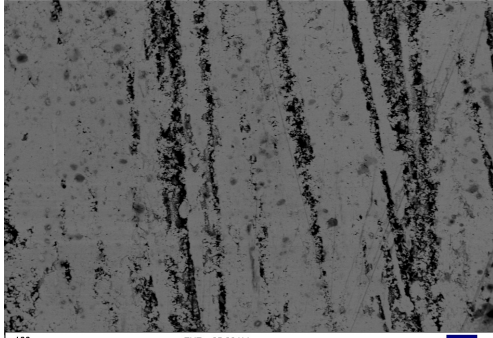
PropS-SH		
condition	SE	BSE
Before ageing 0d TOW		
After ageing 10d TOW		

Table 5: SE and BSE images of the surface of gilded sample coated with propS-SH, at different time of ageing
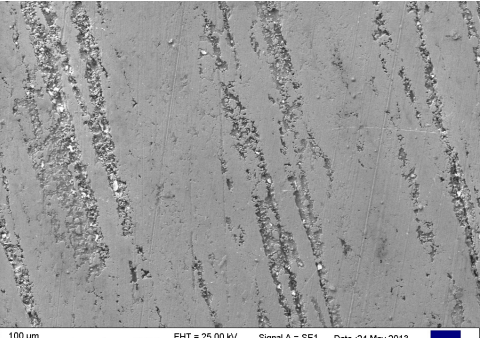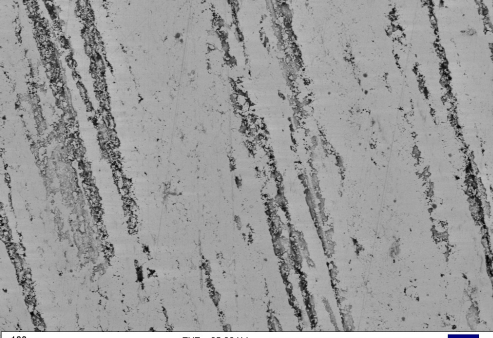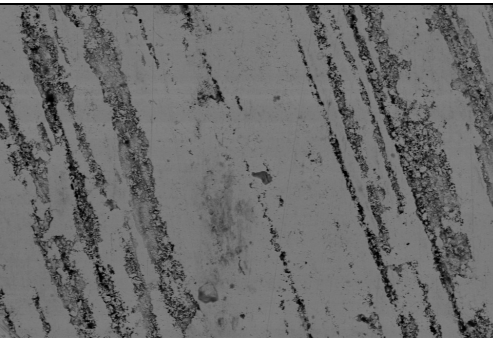
PropS-SH + CeO$_2$		
condition	SE	BSE
Before ageing 0d TOW		
After ageing 10d TOW		

Table 6: SE and BSE images of the surface of gilded sample coated with propS-SH+CeO$_2$, at different time of ageing

The images in Table 4, 5 and 6 show that the surface morphology of gilded samples (both before and after ageing tests) consists of smooth areas with diagonal grooves into which the gold layer is less compact and more porous. The presence of grooves on the bronze surface, already before gilding, is due to the polishing procedure for removing the oxidized layer after casting. The polishing grooves did not allow a homogeneous burnishing, i.e. gold compaction, after mercury evaporation, leading to the presence of a porous gold layer into the grooves.

In the areas shown in Table 4, 5 and 6, at first the general composition was analysed (Table 7), then localized analyses were carried out on both smooth and porous areas in the gold layer, for checking if there is any difference between them (Figure 6 to 11).

Table 7 gives the EDS results of the different gilded samples before and after ageing in the broad areas (500x magnification).

Element	uncoated	uncoated	PropS-SH	PropS-SH	PropS-SH + CeO2	PropS-SH + CeO2
wt%	*0d TOW*	*10d TOW*	*0d TOW*	*10d TOW*	*0d TOW*	*10d TOW*
C	8.05 ± 0.6	6.94 ± 0.8	11.41 ± 0.4	13 ± 2.1	10.16 ± 0.7	12.03
N	3.98	/	3.31	/	/	/
O	2.14 ± 0.3	1.74 ± 0.2	10.11 ± 1.6	9.81 ± 2.7	8.87 ± 1.8	8.49 ± 1.1
Si	/	/	1.62 ± 0.5	1.89 ± 1.2	0.98 ± 0.2	1.2 ± 0.3
S	/	/	2.32 ± 1	2.78 ± 2.5	/	1.3 ± 0.5
Cl	/	0.13 ± 0.1	/	0.12 ± 0.1	/	0.14 ± 0.03
Cu	5.51 ± 3	1.93 ± 0.8	1.99 ± 0.2	2.2 ± 0.4	2.52 ± 1.2	2.9 ± 1.1
Au	74.21 ± 3.1	80.29 ± 1.8	63.65 ± 2.7	62.02 ± 7.1	69.84 ± 2.4	74.8 ± 5
Hg	8.76 ± 0.6	9.52 ± 0.3	7.84 ± 0.2	8.08 ± 1.5	7.39 ± 0.3	6.84 ± 0.1
Sn	/	0.05 ± 0.01	/	/	/	0.19 ± 0.2
Ce	/	/	/	/	0.23 ± 0.1	0.28 ± 0.1

Table 7: EDS results (averaged over three 500x magnification areas) for the gilded samples, at different time of ageing

In all samples, no significant change on the metal elements concentration appears. Moreover, Hg is present in all samples due to the fact that it was used in the process of application of the gold layer.

In the case of the uncoated sample, the corrosion-related elements (such as Cl, O and S) do not show a significant increase. However, the main difference after exposure is that N and C concentrations diminish quite considerably compared to other elements. These elements are related to the gilding procedure and they were probably etched away, during dropping test, by the ageing solution.

In the case of coated samples, the corrosion elements (Cl, O, S) remain almost the same. Moreover, the concentration of the elements of the silane coating (Si, S) is quite constant. It describes the fact that the silane coating was not significantly damaged during the ageing process.

Subsequently, localized areas were analysed by EDS analysis for comparing smooth and porous areas at different times of exposure. Since smooth areas correspond to surfaces where the gold layer fit well to the bronze one, and porous areas correspond to the area where the cavities of bronze are not filled in the same way with gold, one expectation is that there is not the same quantity of inhibitor into these two different areas.

a) Uncoated gilded sample

- Before ageing (0d TOW)

Elements % in mass	Spectrum 1	Spectrum 2
C	3.32	11.91
N	5.24	-
O	-	6.73
Cu	1.51	2.40
Au	80.29	69.21
Hg	9.64	9.75
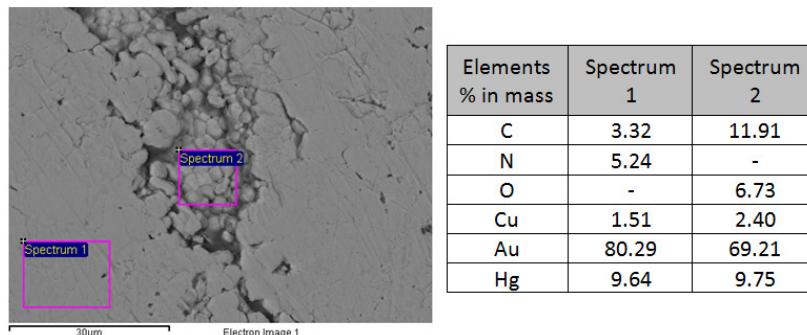
Figure 6: BSE image of the uncoated sample at 0d TOW of exposure

A difference in the aspect of the surface is visible between the smooth area (zone 1) and the porous one (zone 2).

In zone 2, the amount of gold is lower than in zone 1 because the gold layer is porous. Thus the amount of copper from the bronze substrate underneath the gold layer (which can be less than 2 µm thick in some places) is higher is zone 2.

- After ageing (10d TOW)

Elements % in mass	Spectrum 1	Spectrum 2	Spectrum 3	Spectrum 4	Spectrum 5	Spectrum 6
C	49.19	6.85	3.53	7.45	10.56	7.33
O	18.24	-	-	-	-	-
Al	0.28	-	-	-	-	-
Cl	-	0.20	0.04	0.01	-	0.09
Cu	2.29	0.98	3.88	3.21	1.56	1.76
Sn	0.26	-	-	-	-	-
Au	25.71	83.39	81.96	79.47	78.13	80.48
Hg	4.03	8.59	10.60	9.85	9.75	10.33
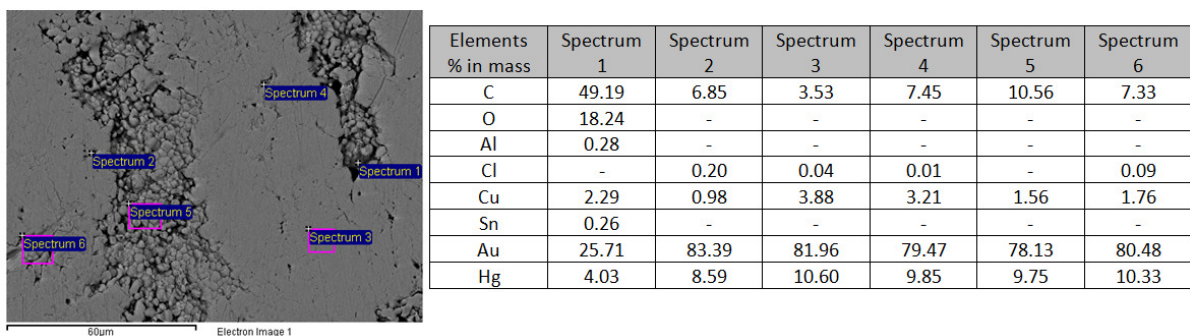
Figure 7: BSE image of the uncoated sample at 10d TOW of exposure

The corrosion process may have started because there is the presence of Cl in many areas. However, only cross section observation will give reliable indications due to the non-homogeneous morphology of these surfaces. Zone1 corresponding to porous gold, contain more O than other areas and less Au/Hg.

b) Gilded sample coated with PropS-SH

- Before ageing (0d TOW)

Elements % in mass	Spectrum 1	Spectrum 2
C	10.20	17.45
O	5.98	14.23
Si	-	2.91
S	-	4.81
K	-	0.23
Cu	5.12	2.86
Au	67.74	51.25
Hg	10.96	6.27
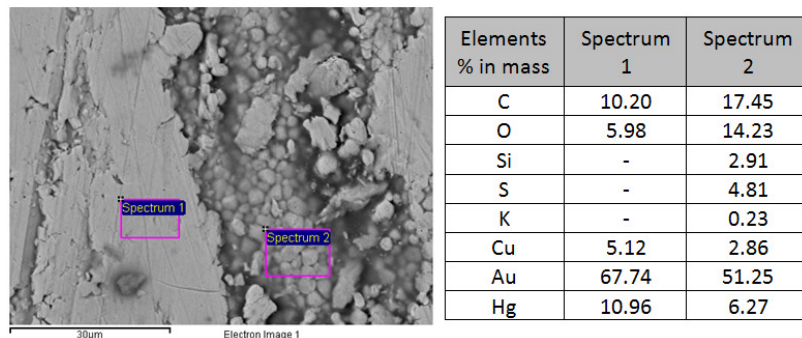
Figure 8: BSE image of the sample coated with PropS-SH at 0d TOW of exposure

The same conclusions as for the uncoated sample can be drawn.

Moreover, the elements of the silane coating (Si and S) are present in zone 2 (porous area) which appears more blurred than in the case of the uncoated sample. Therefore, the silane coating accumulates in porous areas.

- After ageing (10d TOW)

Elements % in mass	Spectrum 1	Spectrum 2	Spectrum 3
C	23.07	61.37	12.91
O	21.19	5.13	11.79
Si	14.77	2.38	1.93
S	19.51	3.26	3.10
Cu	0.79	0.64	3.38
Au	20.68	23.94	59.95
Hg	-	3.29	6.94
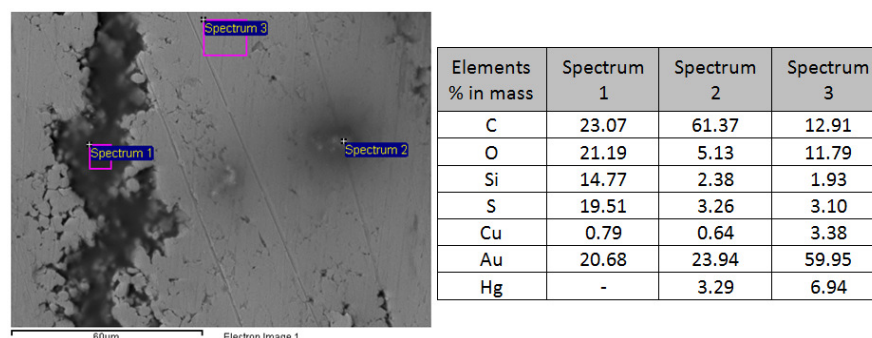
Figure 9: BSE image of the sample coated with PropS-SH at 10d TOW of exposure

After ageing there is a more significant concentration of Si, S and O in the porous areas (Zone 1). Zone 2 displays a "cluster" of silane coating, where C, Si and S are slightly higher than in the smooth background (Zone 3).

c) Gilded sample coated with PropS-SH + CeO₂

- Before ageing (0d TOW)

Elements % in mass	Spectrum 1	Spectrum 2	Spectrum 3
C	6.99	15.75	11.91
O	3.91	13.80	9.37
Si	-	2.04	1.08
S	-	2.87	1.42
Cu	4.67	4.57	3.67
Au	75.93	55.86	65.06
Hg	8.50	4.99	7.48
Ce	-	0.11	-
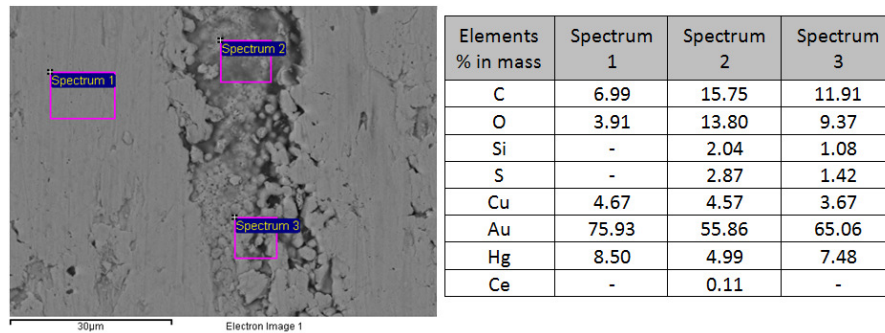
Figure 10: BSE image of the sample coated with PropS-SH +CeO$_2$ at 0d TOW of exposure

Zone 2 and zone 3 are porous areas and thus contain more Si and S (elements of the silane coating) than the smooth area in Zone 1. They also contain a higher amount of O and C and a lower amount of gold.

- After ageing (10d TOW)

Elements % in mass	Spectrum 1	Spectrum 2	Spectrum 3	Spectrum 4	Spectrum 5	Spectrum 6
C	44.68	26.34	23.04	10.05	3.59	25.17
O	10.45	26.24	14.39	4.97	-	25.34
Si	1.52	6.96	1.94	-	-	7.68
S	2.03	10.32	2.44	-	-	10.76
Cl	0.13	-	0.21	0.21	-	-
Cu	1.45	3.78	2.55	1.73	1.03	4.53
Sn	-	-	-	-	0.35	-
Ce	1.33	-	0.24	-	0.42	-
Au	34.95	26.37	48.24	75.10	89.36	26.52
Hg	3.45	-	6.96	7.94	5.25	-
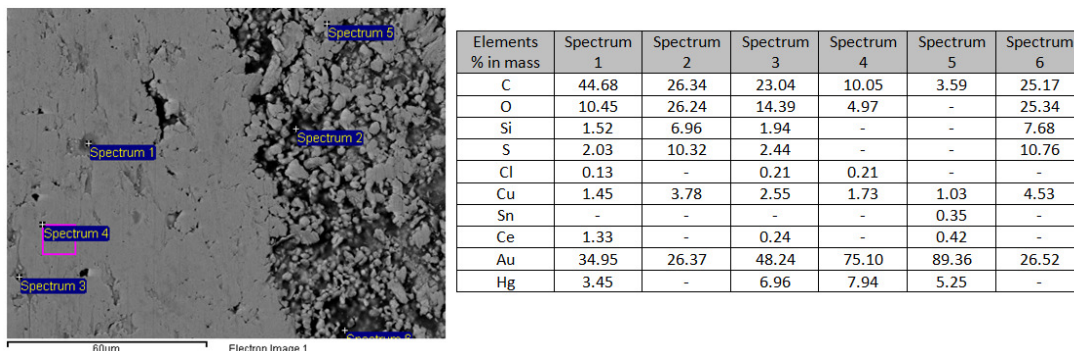
Figure 11: BSE image of the sample coated with PropS-SH +CeO$_2$ at 10d TOW of exposure

Tiny darker points are visible on the smooth surface. They are represented by Zone 1. In this zone, more C and Ce elements are present than in the other ones.

Since these darker points are not present in the case of the uncoated sample, they could correspond to thicker accumulations of the silane coating. However, in the case of the sample coated with PropS-SH + CeO$_2$, there are less big silane clusters than in the PropS-SH coated sample (as the one shown in Figure 11). One hypothesis is that it is due to a higher homogeneity of the silane layer due to the beneficial influence of CeO$_2$ particles.

2.2.4.2. Analysis of cross sections

At the end of the ageing test, cross-sections have been made for having a better understanding of the corrosion process that occurs in gilded bronzes coated or uncoated with silane layers.

The procedure of mounting of the samples for cross sections is the same as described in section 1.2.4.1.

The cross sections were analyzed by SEM analysis on different sites of interest. Results are shown in the following sub-paragraphs.

By scanning the entire cross-sections, it occurred that gilded bronzes contain less corrosion than non-gilded ones aged in the same conditions (described in section 1). It is due to the addition of the gold layer that is a protective barrier against corrosion, at least in short term exposure.

a) Uncoated gilded sample
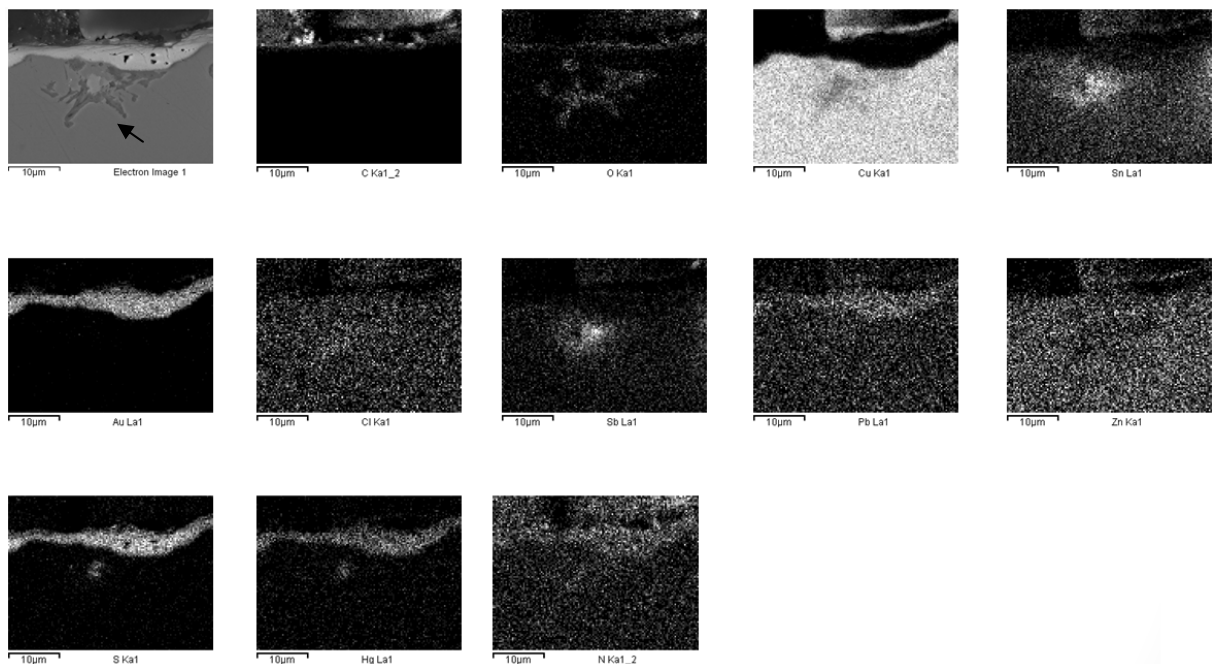
Figure 12: BSE image and X-ray maps showing the distribution of elements in the uncoated gilded sample (10d TOW)

In all the cross section images of gilded bronzes, the dark layer on the top is due to the presence of the mounting resin. The white layer in the middle is the gold layer.

The uncoated sample shows a few localized corrosion spots at the interface between the gold layer and the bronze substrate. The BSE image and X-ray maps in Figure 12 show a representative example (black arrow) of localized corrosion at the Gold/bronze

interface, where elements such as O and Cl were detected. The branching morphology in the lower part of the corroded zone might be related to intergranular corrosion. A Sn-rich area is present at the center of the corroded spot.

As regards the gilded layer, Pb and Au are localized at the same place. According to the Au-Pb binary phase diagram [62], Au and Pb are not soluble in each other, however they can form intermetallic compounds. Also some residual Hg was detected in the Au-rich layer.

b) Gilded sample coated with PropS-SH

Elements % in mass	Spectrum 1
O	13.44
Cu	76.92
Sn	2.71
Pb	6.93
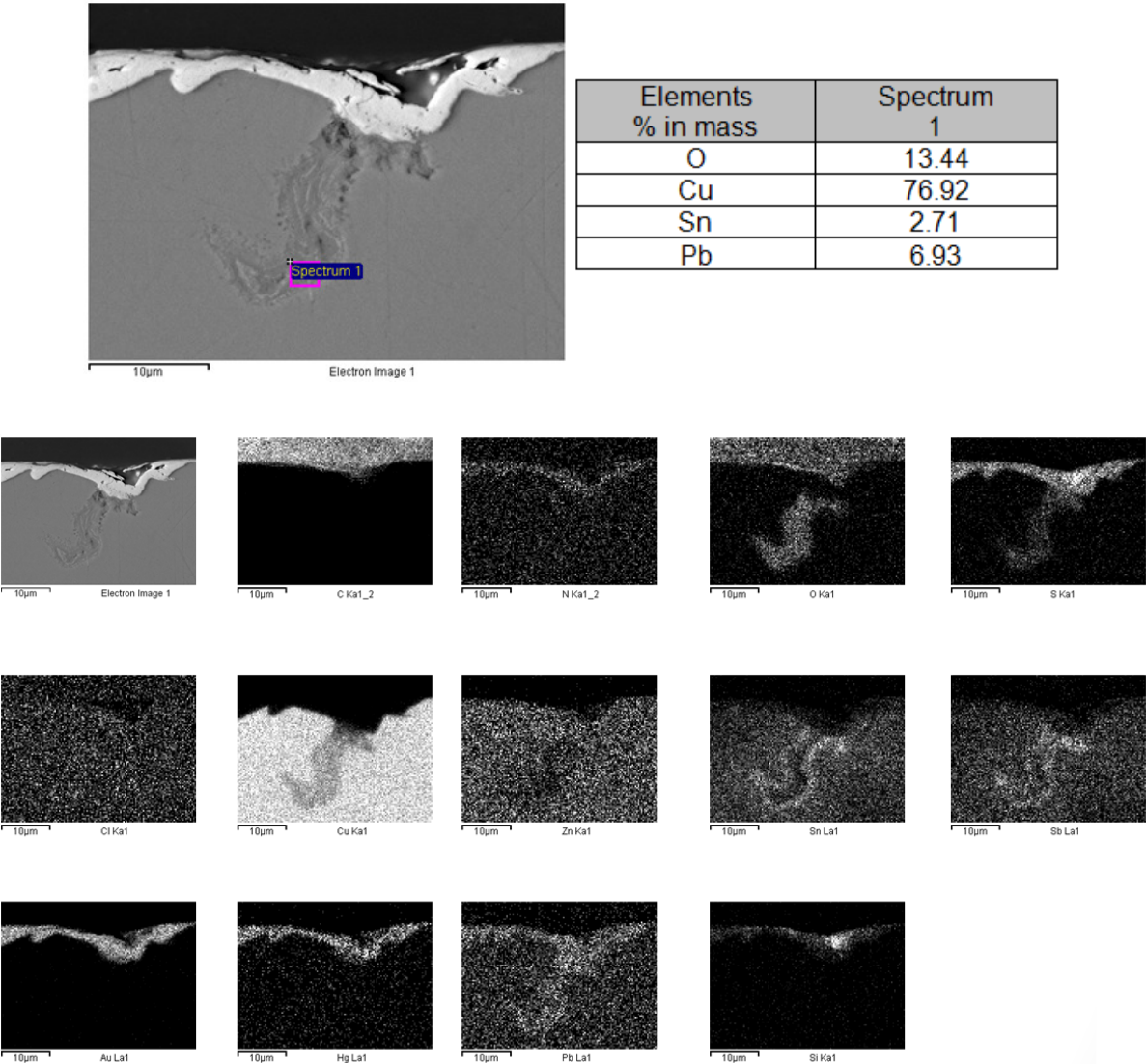
Figure 13: BSE image and X-ray maps showing the distribution of elements in the gilded sample coated with PropS-SH (10d TOW)

Notwithstanding the observation of all the cross section, no areas with clearly recognizable corrosion attacks were detected. However, all the possible alteration

morphologies were documented. One of the most representatives is shown in Figure 13.

The X-ray maps in Figure 13 show that the analysed area is not clearly related to corrosion (absence of Cl). The morphology of this zone, together with the presence of O and Pb and the distribution of Sn (around the borders of the oxidized area) might be explained by the hypothesis that this is a shrinkage cavity (casting defect), emerging on the bronze surface before gilding.

In this area, the distribution of the silane coating is visible (S, Si maps). It highlights the fact that PropS-SH goes into the cavities of the Au-rich layer.

N is present as a layer in the same area than the gold layer. In that case, N is related to the nitric acid that was used during the etching of the bronze surface which takes place in the gilding process. Moreover, Hg is also present in the same place.

c) Gilded sample coated with PropS-SH + CeO$_2$

Elements % in mass	Spectrum 1	Spectrum 2	Spectrum 3	Spectrum 4	Spectrum 5
C	6.68	-	56.35	6.39	-
O	21.10	10.10	19.28	-	-
Cl	0.38	-	-	-	-
Cu	52.31	2.87	4.86	6.69	93.14
Sn	13.58	-	-	-	3.99
Sb	5.95	-	-	-	0.86
Pb	-	1.87	-	-	-
Zn	-	-	-	-	2.01
Si	-	1.00	4.77	-	-
S	-	-	5.76	-	-
Au	-	76.44	8.98	76.21	-
Hg	-	7.73	-	10.71	-
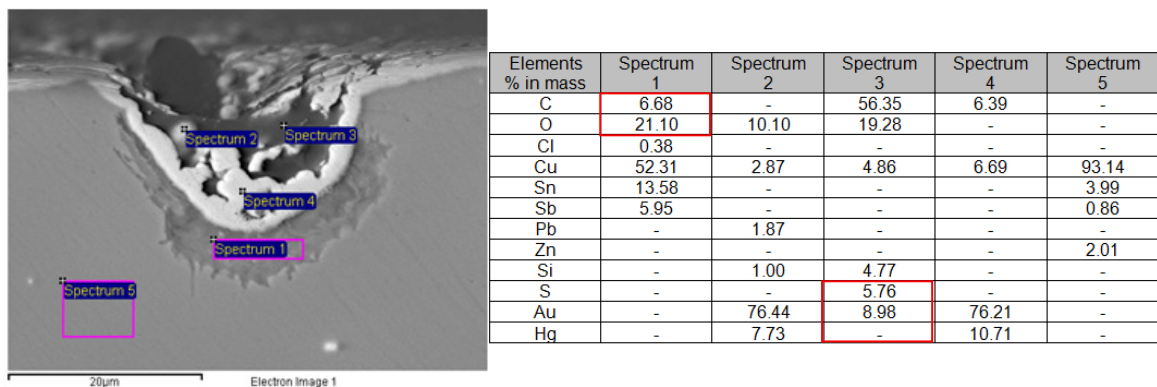
Figure 14: BSE image and EDS results of the sample coated with PropS-SH + CeO$_2$

Also in the case of this sample, as for the PropS-SH coated one, the observation of the all interface between the gold layer and the bronze substrate in the prepared cross section showed only a few shrinkage cavities emerging at the bronze surface. A possible localized corrosion spot is show in Figure 14, together with localized EDS analysis results.

Zone 1 contains elements of corrosion (O and Cl) and thus can be assimilated to the corrosion layer that forms at the interface between Cu and Au.

Zone 3 shows the presence of elements of the silane coating (Si and S). It corresponds to porous areas in the gold layer (the mass percentage of gold here is lower in zone 3 than in zone 2 and zone 4, which correspond to the compact gold layer) filled by the silane coating, as already observed when analyzing the free surfaces (section 2.2.4.1.).

2.3. Accelerated corrosion test: concluding remarks

In this section, the corrosion of uncoated and coated gilded bronzes was studied by the dropping test, which simulates the action of leaching rain in unsheltered areas of monuments. The protective coating on these samples was the same silane coating described in section 1 (PropS-SH).

After short-term dropping tests, no noticeable corrosion products were detected on the samples because of the gold layer, which acts as a barrier against atmospheric corrosion and the silane coating which improves this protection. Localised corrosion attacks were detected at the interface between the gold layer and the bronze substrate, mostly in the case of unprotected samples. The determination of released metals in ageing solutions showed that the PropS-SH coating is able to decrease Cu release by comparison to the uncoated gilded sample.

The efficiency of this silane coating was investigated also after adding CeO_2 nanoparticles to PropS-SH. However, in the investigated conditions (dropping test, TOW: 10d) the addition of nanoparticles to the silane coating does not seem to improve significantly the protection against corrosion compared to PropS-SH without nanoparticles.

Section 3

LASER TREATMENT FOR THE REMOVAL OF PropS-SH

3.1. Laser treatment

In this section, the removal of the silane coating with the help of a laser treatment is investigated. Since the silane coating may lose its efficiency with time, it is necessary to find a method that will permit to remove it safely without damaging the noble patina and the substrate.

To that purpose, different methods can be used such as the laser cleaning or the chemical cleaning [52], [63]. Moreover, some questions about the type of laser that could be used and its characteristics have been investigated and discussed in the literature [64], for avoiding possible damages on the masterpieces. In the present work, we investigated the influence of laser fluence (energy/surface) on the morphology of the surface after removal of the PropS-SH layer, applied on patinated quaternary bronze and aged by natural exposure.

3.1.1. Tested material

The sample used for studying the removal of PropS-SH by laser treatment was a coupon of G-85 quaternary bronze (manufactured by the artistic foundry VenturiArte, in Cadriano (Bologna)), which is often used for artistic casting. The chemical composition of the G-85 bronze, measured by EDS analyses, is shown in table 1.

	Cu	Sn	Zn	Pb	Ni
Weight%	87.5	4.4	3.9	3.8	0.8

Table 1: Composition of G-85 alloy

Before being inhibited with PropS-SH, the sample was aged for 206 days by natural exposure (pre-patination phase). In that way, we are in the situation of actual conservation interventions, in which restorers do not apply the protective films on bare metal but on the patina.

The natural exposure was made in Rimini. The sample was thus exposed to a marine-urban environment. Moreover, the geometry of exposure corresponds to a sheltered area (exposed to the action of stagnant rain).

Figure 1: device in Rimini for the exposure of samples in a sheltered geometry. The samples are located in the centre of the frame

After pre-patination, the surface of the bronze sample was characterized by different spectroscopic methods: X-Ray Diffraction (XRD), Energy Dispersive Spectroscopy (EDS) and μ-Raman in the same conditions described in Section 1.2.4.

The results related to these analyses are shown, respectively, in Table 2-4.

	C	O	Al	Si	S	Cl	Ca	Cu	Sn	Zn	Pb	Ni
Weight %	-	22.1	0.3	0.6	0.8	2.7	0.6	64.6	3.1	1.4	3.8	0.7

Table 2: Surface analysis of the patinated suface by EDS at 206d (natural exposure)

EDS results for the pre-patinated bronze show the presence of elements due to the formation of corrosion products such as O and Cl (not present in the bare bronze, figure 1) and a decrease of alloying elements Cu, Sn, Zn. The typical Sn enrichment observed in real outdoor bronzes [4] has not started yet.

As regards corrosion products, XRD results (table 3) and Raman results (table 4) show mainly the presence of copper corrosion products, among which it is worth mentioning chlorides and posnjakite, a precursor of brochantite [65]. Brochantite is a typical component of patinas on outdoor bronze monuments [65] but it is not present yet in this sample.

Raman analyses reveal also the presence of compounds from atmospheric contamination (quartz, calcite and carbon).

Cuprite - Cu_2O	++
Nantokite - $CuCl$	++
Massicot - PbO	++
Posnjakite - $Cu_4(SO_4)(OH)_6 \cdot H_2O$)	++
Brochantite - $Cu_4(SO_4)(OH)_6$	-
Buttgenbachite - $Cu_{19}Cl_4(NO_3)_2(OH)_{32} \cdot 2(H_2O)$	+/-

Table 3: Surface analysis by XRD at 206d
(-) =non detectable; (+/-) =traces; (++) =significant amount

Cuprite - Cu_2O
Quartz
Calcite
Carbon
Organic compounds

Table 4: Surface analysis by μ-Raman at 206d

After the pre-patination phase, the patinated coupon was sent to the Centro di Corrosione "A. Daccò" of the University of Ferrara for applying the coating film of PropS-SH (by the same method described in Section 1.1.4).

Then, the sample was submitted to the natural exposure in Rimini again. The ageing phase lasted for 380 days. Also in this case, the surface of the samples was characterized at the end of the exposure by SEM-EDS, XRD and micro-Raman analyses.

The results are shown, respectively, in table 5, table 6 and table 7.

	C	O	Mg	Al	Si	S	Cl	Ca	Cu	Sn	Zn	Pb	Ni
Weight%	8.2	29.7	0.6	0.4	4.2	2.7	6.4	1.1	46.6	1.4	0.9	2.7	0.4

Table 5: Surface analysis by EDS at 380d

EDS results for coated bronzes after ageing (380d) show the presence of elements from the silane coating (Si and S). It means that after the ageing step there is still PropS-SH on the surface.

Moreover, EDS results show the presence of elements due to the formation of corrosion products such as O and Cl and the presence of elements from the atmospheric contamination (Al, Mg, C, Ca).

XRD results (table 6) and Raman results (table 7) show mainly the presence of copper corrosion products and compounds from the atmospheric contamination.

Cuprite - Cu_2O	+/-
Nantokite - $CuCl$	+
Atacamite - $Cu_2Cl(OH)_3$	++
Gherardite - $Cu_2(NO_3)(OH)_3$	+/-
Anglesite - $PbSO_4$	+/-
Environmental deposition: quartz	+

Table 6: Surface analysis (by XRD) at 380d
(-) =non detectable; (+/-) =traces; (++) =significant amount

Cuprite - Cu_2O
Environmental deposition: quartz, anatase

Table 7: Surface analysis (by μ-Raman) at 380d

3.1.2.   Laser cleaning method

A laser treatment has been done on the G-85 sample (pre-patinated + coated + aged) in order to try to remove the silane coating layer.

The laser cleaning treatment was carried out at the CNR Institute of Applied Physics "Nello Carrara" of Sesto Fiorentino in Florence, whilst we focused on surface characterization.

Before the laser treatment, the G-85 sample was submitted to indentation using a micro-Vickers device in order to characterize the surface in the same area of the sample, before and after the laser treatment. Eight different areas were marked by micro-Vickers as shown in figure 2.
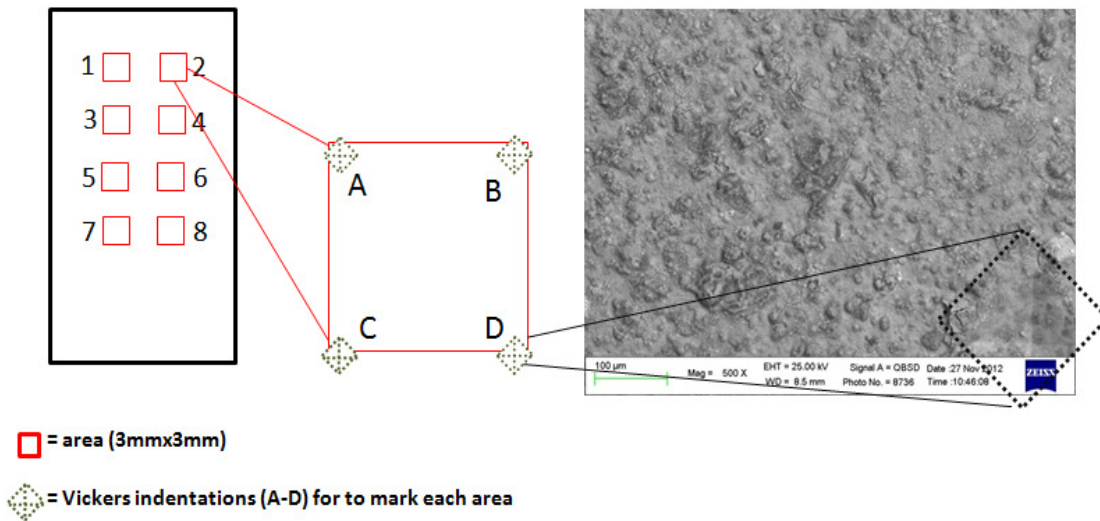
Figure 2: Scheme of indentation marks done by using a micro-Vickers device, on G-85 coupon before laser treatment; on the right: SEM-BSE image of these sites

These different eight areas were made for applying different laser fluence on each one.

The laser characteristics are:

Laser type	Emission wavelength (nm)	Pulse time (ns)	Focal spot area (cm²)	Laser fluence (J/cm²)
Nd: YAG LQS	1064	120	fixed	variable

Figure 3: Laser characteristics

3.2. Results

Eight different laser fluences (table 8) were applied on the sample. In that way, it is possible to understand what is the good laser fluence range that permits to remove the maximum of coating layer without damaging the corrosion patina.

In figure 4 is shown the sample after treatment laser where we can see the areas submitted to the laser treatment. The treated spots in the lower part of the sample were produced in the preliminary step for the selection of the best laser treatment conditions, therefore they were not analysed.

Area	Laser Fluence (J/cm^2)
1	0.57
2	0.53
3	0.36
4	0.40
5	0.26
6	0.24
7	0.28
8	0.43

Table 8: Laser fluences with their corresponding area treatment
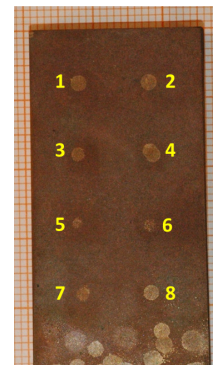
Figure 4: Sample B8 after laser

3.2.1. Characterization of surfaces before and after laser cleaning: SEM-EDS

In order to make a comparison of the surface before and after laser cleaning, a table of the SEM images was made for each area:
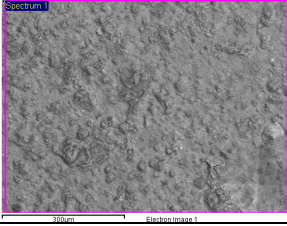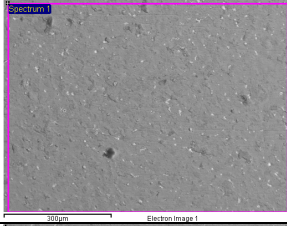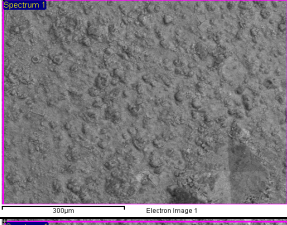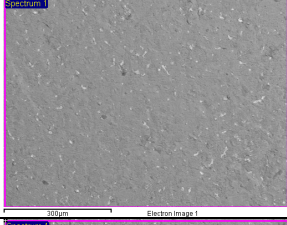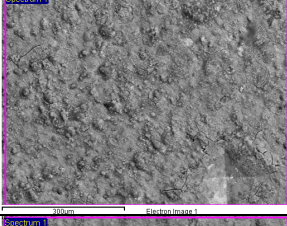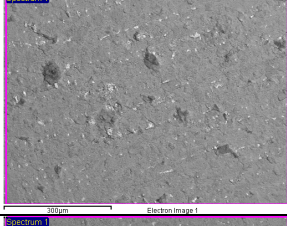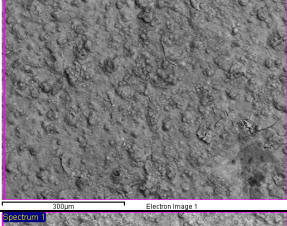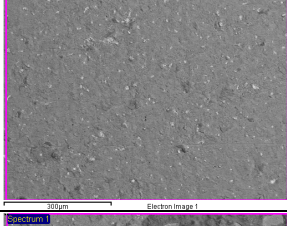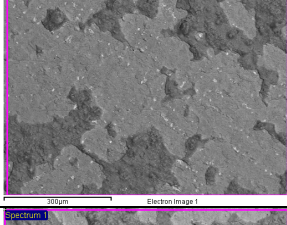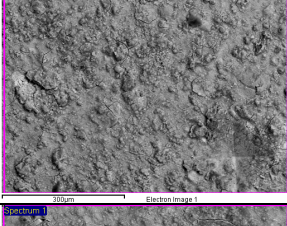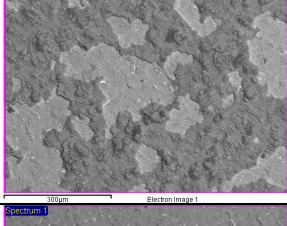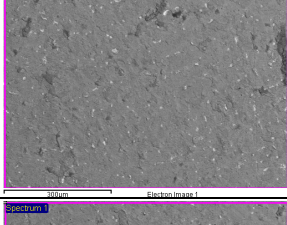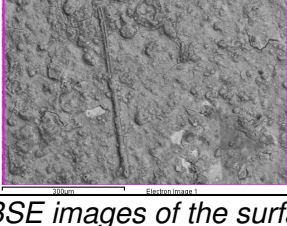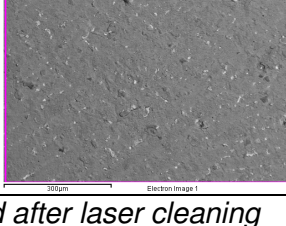
area	SEM image before laser cleaning	SEM image after laser cleaning
AREA 1 Laser 0.57 J/cm^2		
AREA 2 Laser 0.53 J/cm^2		
AREA 3 Laser 0.36 J/cm^2		
AREA 4 Laser 0.40 J/cm^2		
AREA 5 Laser 0.26 J/cm^2		
AREA 6 Laser 0.24 J/cm^2		
AREA 7 Laser 0.28 J/cm^2		
AREA 8 Laser 0.43 J/cm^2		

Table 9: BSE images of the surface before and after laser cleaning

On the pictures after laser cleaning, we can notice that the surface is not homogeneous: both darker areas (where the patina layer (coated with PropS-SH) was not removed by the laser treatment) and lighter areas (i.e. areas with a higher average atomic number in BSE images, where silane layer was completely removed but also the patina was thinned by the laser treatment). Moreover, the area fraction of the dark zones, corresponding to the double layer "patina+PropS-SH", increases with decreasing laser fluence.

In table 10 are reported averaged EDS data of the analysis of the eight different areas after laser cleaning with different fluences (measured at 500x magnification).

EDS (w%)	C	O	Mg	Al	Si	S	Cl	Ca	Cu	Sn	Zn	Pb	Ni
AREA 1- Laser: 0.57 J/cm^2	8.9	8.3	/	/	/	0.2	1.2	/	71.1	4.4	2.7	2.6	0.6
AREA 2- Laser: 0.53 J/cm^2	5.3	8.2	/	/	/	/	1.1	/	74.0	4.6	2.7	3.5	0.6
AREA 3- Laser: 0.36 J/cm^2	11.0	9.6	/	/	0.2	/	1.2	/	66.6	4.5	2.6	3.6	0.6
AREA 4- Laser: 0.40 J/cm^2	7.2	9.7	/	/	/	/	1.3	/	70.4	4.7	2.5	3.6	0.6
AREA 5- Laser: 0.26 J/cm^2	10.6	**14.7**	/	/	**1.2**	**0.7**	**2.8**	/	60.6	3.4	1.8	3.5	0.5
AREA 6- Laser: 0.24 J/cm^2	/	**21.9**	0.5	0.4	**3.2**	**1.6**	**4.8**	0.6	57.8	2.3	1.7	4.8	0.4
AREA 7- Laser: 0.28 J/cm^2	7.0	9.9	/	/	/	/	1.4	/	70.2	4.6	2.3	3.7	0.8
AREA 8- Laser: 0.43 J/cm^2	5.4	9.4	/	/	/	/	1.3	/	72.4	4.9	2.6	3.4	0.7

Table 10: EDS analysis of G-85 sample after laser cleaning

Concerning the area 5 and area 6, the elements of the silane coating (Si and S) are still present. Moreover there is the highest amount of elements (O and Cl) due to the formation of corrosion products.

Conversely, there are no more elements of the silane coating (S and Si) in areas 1, 2, 3,4,7,8 whereas there are elements due to the formation of corrosion products such as O and Cl. It may indicate that in these areas the laser fluence is high enough to remove the inhibitor layer and preserve the patina. However, at higher magnification (figure 5), we can observe that the PropS-SH has been removed together with most

of the patina layer, but locally we can still find tiny islets with the patina and the PropS-SH top layer, even where we applied the highest laser fluence. In particular, this is illustrated in area 1, which corresponds to a laser fluence of 0.57 J/cm^2:

Figure 5: BSE image and EDS results of area 1 (Laser Fluence = 0.57 (J/cm²))
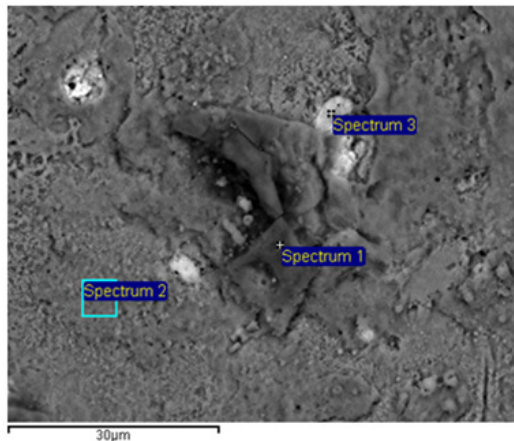
(wt%)	Spectrum 1	Spectrum 2	Spectrum 3
C	-	5.0	5.1
O	10.8	11.5	12.1
Si	2.2	-	-
S	1.9	-	3.3
Cl	5.3	1.4	6.6
Cu	75.6	71.3	12.6
Sn	1.6	5.3	-
Zn	1.8	2.7	-
Pb	-	2.1	60.3

The elements typically present in corrosion products (O and Cl) were detected on each zone that was analyzed, thus indicating that corrosion products are still present on the surface, even though patina composition and morphology has changed after the laser treatment. Concerning elements of the silane coating (Si and S), they are present in zone 1 and zone 3 (lead globule), indicating that the silane coating is still present over the patina in the analysed spot.

A comparison of high magnification SEM images and EDS results is also shown for area 3 (fluence: 0.36 J/cm², Figure 6) and area 5 (fluence: 0.26 J/cm², Figure 7).
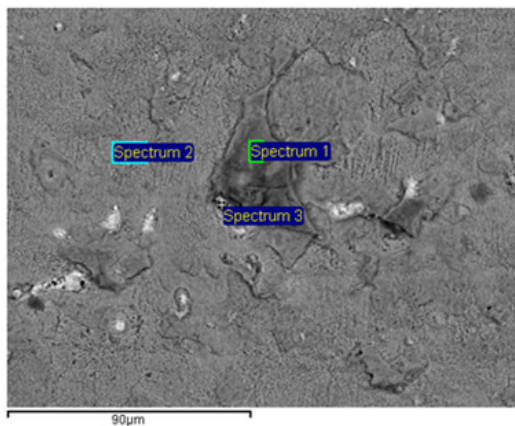
(wt%)	Spectrum 1	Spectrum 2	Spectrum 3
C	13.9	6.9	-
O	17.8	7.2	6.8
Si	4.8	-	-
S	2.1	-	-
Cl	1.6	0.6	9.8
Cu	58.6	76.5	35.7
Sn	1.1	5.0	-
Zn	-	3.0	-
Pb	-	-	47.7

Figure 6: BSE image and EDS results of area 3 (Laser Fluence = 0,36 (J/cm²))
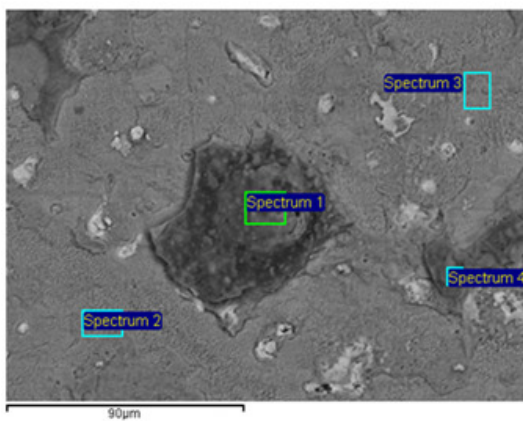
(wt%)	Spectrum 1	Spectrum 2	Spectrum 3	Spectrum 4
C	-	5.7	5.6	-
O	23.0	7.4	7.3	29.3
Si	6.0	-	-	5.1
S	6.9	-	-	3.0
Cl	6.9	1.0	0.6	7.0
Cu	56.0	80.0	77.4	47.6
Sn	-	2.4	4.5	-
Zn	-	2.7	2.7	1.0
Pb	-	-	1.1	5.7

Figure 7: BSE image and EDS results of area 5 (Laser Fluence = 0,26 (J/cm²))

85

Also in these areas, there are some dark zones which correspond to the double layer patina+PropS-SH because in these areas the elements of the silane coating (Si and S) were detected. Moreover, we observed the presence of elements typically present on corrosion products (O and Cl) on each zone that we analyzed. Therefore, the area fraction where the PropS-SH was removed (mostly together with the underlying patina) changes with the laser fluence, but no fluence in the investigated range allowed the complete and selective removal of PropS-SH without altering the patina.

We also observed the presence of spherical particles in each area, at every fluence that we used. It was possible to observe these particles at higher magnification.

As representative examples of these spheres and for making comparisons, we reported in figure 8 the data about area 1 (Laser Fluence = 0.57 J/cm^2), area 4 (Laser Fluence = 0.40 J/cm^2) and area 7 (Laser Fluence = 0.28 J/cm^2).
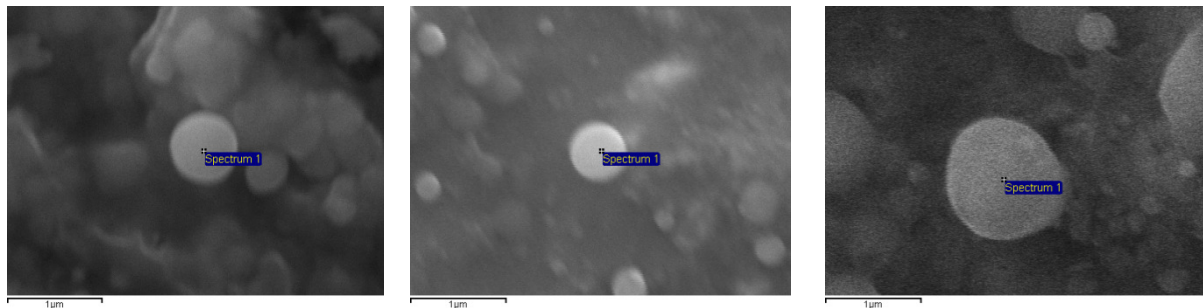
Figure 8: BSE maps at high magnification of the spherical particles for different laser fluence (on the left: area1, in the middle: area 4, on the right: area 7)

One hypothesis about the origin of these spherical particles may be the following: consequently to the heating of the surface because of the laser power, PropS-SH may undergo thermal modification. Differential Scanning Calorimetry measurements (temperature rate: 20 °C/min) on the silane coating showed that the melting temperature of PropS-SH is about 108 °C. Since this temperature can be reached by the bronze surface during the laser treatment [66], these spherical particles could be due to a local melting of the silane coating.

3.2.2.   Quantification of areas after laser cleaning

In order to quantify the area fraction of the double layer patina+PropS-SH still present on the surface after the laser treatment, we carried out image analysis by the Image ProPlus software.

Two different thresholds were selected, the red one describing the layer patina+PropS-SH and the yellow one describing the substrate (i.e. the thin layer of patina modified by the laser treatment).

In figure 19 are reported pictures of the threshold selection with the corresponding percentages of the double layer patina+PropS-SH coating.
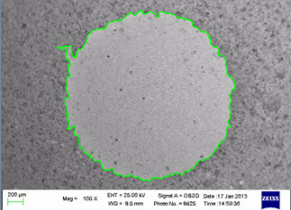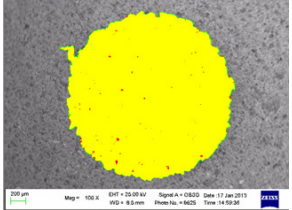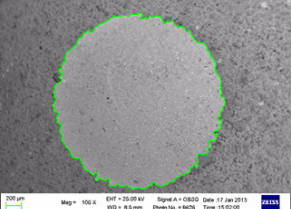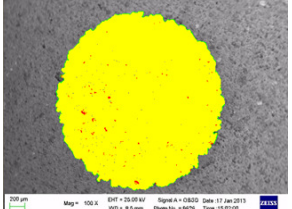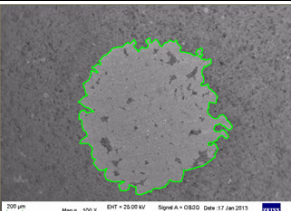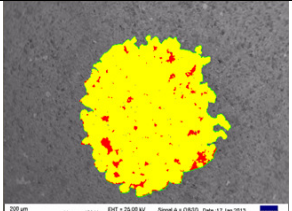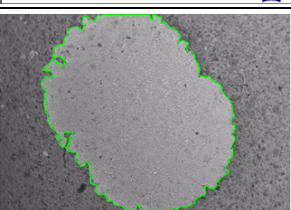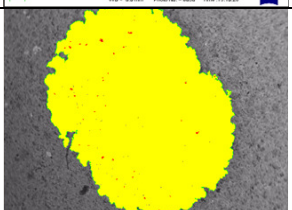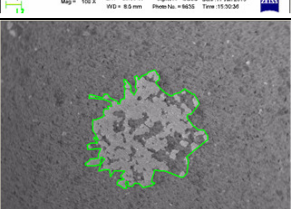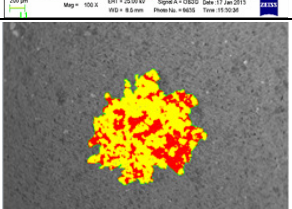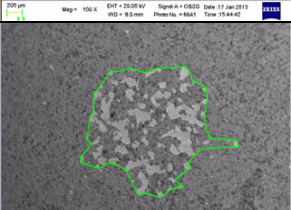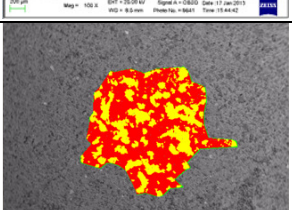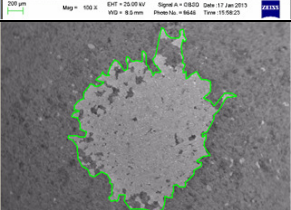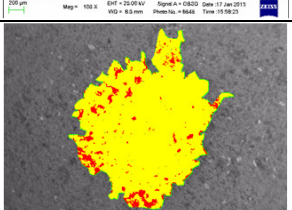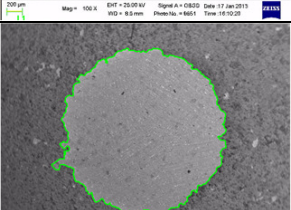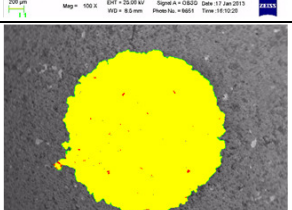
Area	Selected area	Quantified areas	% Patina+coating
AREA 1 Laser 0.57 J/cm^2			0.518
AREA 2 Laser 0.53 J/cm^2			0.676
AREA 3 Laser 0.36 J/cm^2			5.889
AREA 4 Laser 0.40 J/cm^2			0.266
AREA 5 Laser 0.26 J/cm^2			35.903
AREA 6 Laser 0.24 J/cm^2			67.127
AREA 7 Laser 0.28 J/cm^2			8.992
AREA 8 Laser 0.43 J/cm^2			0.331

Figure 9: quantified areas with the corresponding percentage of patina+coating

The quantification of area fractions is summarized in figure 10, where area fraction of the patina+PropS-SH double layer is plotted against laser fluence. The results in figure 10 show that, as already observed on the basis of SEM/EDS, the area fraction of the residual patina+PropS-SH double layer decreases significantly with increasing laser fluence. However, the laser removal treatment was never able to remove selectively the PropS-SH coating from the patinated surface.
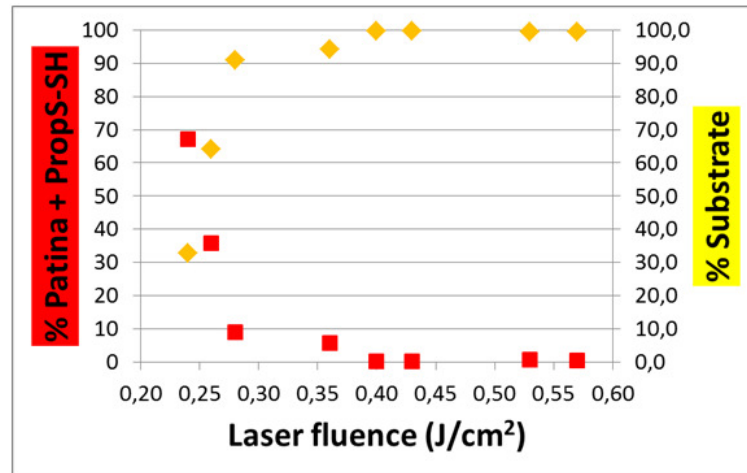
Figure 10: Area fraction of the double layer patina+PropS-SH (red) and of the modified substrate (thinned patina, yellow) as a function of laser fluence.

3.3. Laser cleaning: concluding remarks

On the basis of the characterization of patinated and coated surfaces before and after laser treatment, we can draw the following conclusions: the laser treatment is not able to remove only the organosilane coating: either the treatment modifies the patina (by thinning it) or it leaves tiny islets of the PropS-SH+patina double layer. There is thus a lack of selectivity in the removal step. Further work is required to find better laser treatment conditions.

Conclusions

In this thesis, the protective efficiency of a silane coating (3-mercapto-propyl-trimethoxy-silane (shortly PropS-SH)) on quaternary bronze samples (gilded or not) was assessed by accelerated ageing tests. The ageing of the samples was carried out by dropping test, which simulates the action of leaching rain in unsheltered areas of outdoor monuments. In the case of non-gilded bronzes, the dropping test was used also for the pre-patination of the bronze surface, before applying the protective silane coating. Lastly, also possible removal treatments based on the use of a Nd:YAG laser were investigated for checking the reversibility of the silane coating.

Surface analysis and cross-sections analysis of the samples were run by SEM-EDS, micro-Raman and XRD analysis during the different steps of the study (i.e. pre-patination, ageing) for comparing the corrosion processes that occur on uncoated or coated (with or without addition of nanoparticles) samples and thus have an overview of the efficiency of the silane coating.

1) As regards non-gilded bronzes, pre-patinated before the application of the silane coating, there are not significant differences between the samples in terms of surface features (apart from a slight differentiation in the extent of Sn enrichment). However, gravimetric measurements and inhibiting efficiency values (in terms of metal release) highlighted that the addition of nanoparticles increases the protective efficiency by comparison to PropS-SH. In particular, PropS-SH + La_2O_3 gives the best results.

2) As regards gilded bronzes, no noticeable signs of degradation were detected on the surfaces after exposure, whilst localised corrosion attacks were detected at the interface between the gold layer and the bronze substrate, mostly in the case of unprotected samples. The determination of released metals in ageing solutions showed that the PropS-SH coating is able to decrease Cu release by comparison to the uncoated gilded sample. The addition of nanoparticles to the silane coating does not seem to improve significantly its protective efficiency towards gilded bronzes.

3) A laser treatment was performed on patinated, non-gilded bronzes for studying the removal efficiency of the silane coating (important in terms of reversibility of the protective coating process for outdoor monuments). The silane coating was applied on quaternary bronze (pre-patinated by natural exposure) and was aged by natural exposure for about 1 year before the removal treatment. The laser fluences used for removing the silane coating were not selective enough: either the treatment modified the patina (by thinning it) or it left tiny islets of the PropS-SH+patina double layer.

Acknowledgements

References

[1] E. Bernardi, C. Chiavari, B. Lenza, C. Martini, L. Morselli, F. Ospitali, L. Robbiola (2009). The atmospheric corrosion of quaternary bronzes: The leaching action of acid rain. Corrosion Science, Vol. 51, pp. 159 – 170

[2] L.B. Brostoff (2003): Coating strategies for the protection of outdoor bronze art and ornamentation. Doctoral thesis, University of Amsterdam

[3] D. De la Fuente, J. Simancas, M. Morcillo (2008). Morphological study of 16-year patinasformed on copper in a wide range of atmospheric exposures. Corrosion Science, Vol. 50, pp. 268 – 285

[4] L Robbiola, L-P Hurtel (1991). Nouvelles contributions à l'étude des mécanismes de corrosion des bronzes de plein air : caractérisation de l'altération de bronzes de Rodin. Mémoires et études scientifiques Revue de Métallurgie- Décembre 1991

[5] JW Kim, KH Chang, T Isobe, S Tanabe (2011). Acute toxicity of benzotriazole ultraviolet stabilizers on freshwater crustacean (Daphnia pulex), J. Toxicol. Sci., Vol. 36, pp. 247–251

[6] D.A. Pillard, J.S. Cornell, D.L. Dufresne, M.T. Hernández (2001). Toxicity of benzotriazole and benzotriazole derivatives to three aquatic species. Water Research, Vol. 35, pp. 557 – 560

[7] G. Brunoro, A. Frignani, A. Colledan, C. Chiavari (2003). Organic films for protection of copper and bronze against acid rain corrosion. Corrosion Science, Vol. 54, pp. 2219 – 2231.12

[8] F. Zucchi, A. Frignani, V. Grassi, G. Trabanelli, M. DalColle (2007). The formation of a protective layer of 3-mercapto-propyl-trimethoxy-silane on copper. Corrosion Science, Vol. 49, pp. 1570 – 1583.15.

[9] M.F. Montemor, R. Pinto, M.G.S. Ferreira (2009). Chemical composition and corrosion protection of silane films modified with CeO2 nanoparticles. Electrochim. Acta, Vol. 54, pp. 5179-5189.

[10] F. Zanotto, V. Grassi, A. Frignani, F. Zucchi (2011). Protection of the AZ31 magnesium alloy with cerium modified silane coatings. Materials Chemistry and Physics, Vol. 129, pp. 1 – 8

[11] D. Wang, G. P. Bierwagen (2009). Sol-gel coating on metals for corrosion protection. Prog. Org. Coat., Vol. 64, pp. 327-338.

[12] C. Chiavari, E. Bernardi, C. Martini, F. Passarini, F. Ospitali, L. Robbiola (2010). The atmospheric corrosion of quaternary bronzes, The action of stagnant rain water. Corrosion Science, Vol. 52, pp. 3002 – 3010

[13] P. Fiorentino, M. Marabelli, M. Matteini and A. Moles (1982). The condition of the "Door of Paradise" by L. Ghiberti tests and proposals for cleaning. Studies in conservation, Vol. 27, pp. 145-153

[14] U.S General Services Administration: Bronze characteristics. http://www.gsa.gov/portal/content/111994

[15] K. Sadayapan, M. Sahoo, H.T. Michels (2008). Copper and copper alloy castings. Casting, Vol. 15, ASM Handbook, ASM International, pp. 1085 – 1094. (http://products.asminternational.org/hbk/do/highlight/content/)

[16] P. Piccardo, et al. (May 2004). European Microscopy & Analysis, pp. 5 – 7.

[17] D.A. Scott (1991). Metallography and microstructure of ancient and historic metals. Tien Wah Press Ltd. Singapore, pp. 5 – 29.

[18] Cambridge. June 25th 2011.
http://www.doitpoms.ac.uk/tlplib/solidification_alloys/dendritic.php

[19] D.R. Askeland, P.P. Phulé (2003). The Science and Engineering of Materials. 4th edition, Brooks-Cole.

[20] H. Morales (2011). Atmospheric corrosion of quaternary bronzes (Cu – Sn – Zn – Pb): Laboratory tests (accelerated ageing in wet & dry conditions) and field studies (the Bottego monument in Parma, Italy). Advanced Spectroscopy in Chemistry Master thesis, University of Bologna

[21] H.Strandberga (1998). Reactions of copper patina compounds—I. Influence of some air pollutants. Atmospheric Environment, Vol. 32, Issue 20, 25 September 1998, pp. 3511–3520

[22] C. Leygraf, T.E. Graedel (2000). Atmospheric corrosion. John Wiley & Sons. Electrochemical Society Series.

[23] A. Krätschmer, I. Odnevall Wallinder, C. Leygraf (2002). The evolution of outdoor copper patina. Corrosion Science, Vol. 44, pp. 425 – 450.

[24] J. G. Castano, C. Arroyave, M. Morcillo (2007). Characterization of atmospheric corrosion products of zinc exposed to SO2 and NO2 using XPS and GIXD. J Mater Sci, Vol 42, pp. 9654–9662

[25] C. Chiavari, E. Bernardi, C. Martini, L. Morselli, F. Ospitali, L. Robbiola, A. Texier (2010). Predicting the corrosion behaviour of outdoor bronzes: Assesment of artificially exposed and real outdoor samples. Metal 2010: International Conference on Metal

Conservation (Charleston,South Carolina, USA). Edited by P. Mardikian, C. Chemello, C. Watters, P. Hull. pp. 160 –166

[26] S. Jouen, B. Hannoyer, A. Barbier, J. Kasperek, M. Jean (2004). A comparison of runoff rates between Cu, Ni, Sn and Zn in the first steps of exposition in a French industrial atmosphere. Materials Chemistry and Physics, Vol. 85, pp. 73–80

[27] H. Strandberg, L.G. Johansson, O. Lindqvist (1997). The atmospheric corrosion of statue bronzes exposed to SO_2 and NO_2. Materials and Corrosion, Vol. 48, pp. 1 – 19.

[28] L. Robbiola, K. Rahmouni, C. Chiavari, C. Martini, D. Prandstraller, A. Texier, H. Takenouti, P. Vermaut (2008). New insight into the nature and properties of pale green surfaces of outdoor bronze monuments. Appl. Phys. A 92, pp. 161–169

[29] WebCorr corrosion consulting services
http://www.corrosionclinic.com/types_of_corrosion/pitting_corrosion.htm

[30] A. Giusti, M. Matteini (1997). The gilded bronze paradise doors by Ghiberti in the Florence baptistery. Scientific investigation and problems of restoration Proceedings of the International Conference on Metal Restoration, German National Committee of ICOMOS, München, 1997, pp. 47–51

[31] L. Ghiberti, Opificio delle Pietre Dure (1986). L'oro del Ghiberti – Restauri alla Porta del Paradisio. Museo Opificio delle Pietre Dure e Laboratori du Restauro 7 dicembre 1985

[32] E. Mello (1986). The gilding of Lorenzo Ghiberti's Doors of Paradise. Gold Bulletin 19 (4), pp.123-126.

[33] G.P Bernardini, M.C. Squarcialupi, R. Trosti-Ferroni. (2002). The bronze doors of the baptistery in Florence: a comparative study of the bronze alloys and alteration products. Protection and conservation of the cultural heritage of the Mediterranean cities, Galán and Zezza Swets and Zeitlinger, Lisse, ISBN 90 5809 253 4

[34] Wikipedia
 https://en.wikipedia.org/wiki/Florence_Baptistery

[35] K. Anheuser (1997). The practice and characterization of historic fire gilding techniques. JOM November 1997, pp. 58-62

[36] S. Siano, R. Salimbeni, R. Pini, A. Giusti, M. Matteini (2003). Laser cleaning methodology for the preservation of the Porta del Paradisio by Lorenzo Ghiberti. Journal of cultural heritage, Vol. 4 pp. 140s-146s

[37] T. Kosec, A. Legat, I. Milošev (2010). The comparison of organic protective layers on bronze and copper. Progress in organic coating, Vol. 69, pp.199-206

[38] I. Constantinides, A. Adriaens, F. Adams. (2002). Surface characterization of artificial corrosion layers on copper alloy reference material. Applied surface science, Vol. 189, pp.90-101

[39] M.C. Bernard, E. Dauvergne, M. Evesque, M. Keddam, H. Takenouti (2205). Reduction of silver tarnishing and protection against subsequent corrosion. Corros. Sci., Vol. 47, pp.663

[40] T. Kosec, H. Otmačić Curkovic´, A. Legat (2010). Investigation of the corrosion protection of chemically and electrochemically formed patinas on recent bronze. Electrochimica Acta, Vol. 56, pp.722–731

[41] A. Balbo, C. Chiavari, C. Martini, C. Monticelli (2012). Effectiveness of corrosion inhibitor films for the conservation of bronzes and gilded bronzes. Corr. Sci., Vol. 59, pp.204-212

[42] S. Varvara, L. Muresan, K. Rahmouni, H. Takenouti. (2008). Evaluation of some non-toxic thiadiazole derivatives as bronze corrosion inhibitors in aqueous solution. Corr. Sci., Vol. 50, pp.2596–2604

[43] R. Bostan, S. Varvara, L. Găină, L. M. Mureşan (2012). "Evaluation of some phenothiazine derivatives as corrosion inhibitors for bronze in weakly acidic solution", Corros. Sci., Vol. 63, 275-286

[44] F. Zucchi, V. Grassi, A. Frignani, G. Trabanelli.(2004). Inhibition of copper corrosion by silane coatings. Corr. Sci., Vol. 46, pp.2853-2865

[45] E. P. Plueddemann (1991). Silane Coupling Agents. New York: Plenum Press

[46] W.J. Van Ooij,, D. Zhu, M. Stacy, A. Seth, T. Mugada, J. Gandhi, P. Puomi (2005). Corrosion Protection Properties of Organofunctional Silanes —An Overview. Tsinghua Science and Technology, 10(6), pp.639-665

[47] D. Zhu, W.J. van Ooij (2003). Corrosion Science, Vol. 45, pp. 2177–2197

[48] WR. Thompson, M. Cai, M.K. Ho, J.E. Pemberton (1997). Hydrolysis and Condensation of Self-Assembled Monolayers of (3Mercaptopropyl)trimethoxysilane on Ag and Au Surfaces. Langmuir, Vol. 13, pp.2291-2302

[49] H. Fan, S. Li, Z. Zhao, H. Wang, Z. Shi, L. Zhang (2011). Inhibition of brass corrosion in sodium chloride solutions by self-assembled silane films. Corrosion Science, Vol.53, pp.4273–4281

[50] A. Balbo, A. Frignani, C. Monticelli (2012). Influence of nanoparticles on the inhibiting efficiency of organosilane coatings on bronze. Part 1: Electrochemical characterization. Proceedings of Eurocorr 2012 (EFC Event n.330), 09-13/09/2012, Istanbul, Turkey (EFC, London, UK, CD-ROM) 1-8

[51] E. Cano, D. Lafuente, D. M. Bastidas (2010). Use of EIS for the evaluation of the protective properties of coatings for metallic cultural heritage: a review. J Solid State Electrochem, Vol. 14, pp.381–391

[52] M. Matteini, C. Lalli, I. Tosini, A. Giusti, S. Siano (2003). Laser and chemical cleaning tests for the conservation of the Porta del Paradiso by Lorenzo Ghiberti. Journal of Cultural Heritage, Vol. 4, pp.147s-151s

[53] S.Siano, F.Grazzi, V.A. Parfenov (2008). Laser cleaning of gilded bronze surfaces. J. Opt. Technol. 75, 7, pp.419-427

[54] L. Morselli, E. Bernardi, I. Vassura, F. Passarini, E. Tesini (2008). Long term monitoring of wet and dry depositions in a Po valley city (Bologna, Italy). Lyman G. Roglesfield (Ed.), Acid Rain Research Focus, Nova Science Publishers Inc., pp. 77–107.31.

[55] C.M. Grossi, P. Brimblecombe, R. Esbert, F.J. Alonso (2007). Color changes in architectural limestones from pollution and cleaning. Color Res. Appl., Vol. 32, pp.320 – 331.

[56] D. Zhu, W.J. van Ooij (2004). Corrosion protection of metals by water-based silane mixtures of bis-[trimethoxysilylpropyl]amine and vinyltriacetoxysilane. Progress in Organic Coatings, Vol. 49, pp.42–53

[57] Innovative methods for the conservation of gilded. Report on the 1st year activity of the research project PRIN 2009. University of Ferrara-Corrosion and Metallurgy Study Centre "A.Daccò" Politecnico of Milan-Dept. Chemistry, Materials and Chemical Engineering. University of Bologna-Dept. Metals Science, Electrochemistry and Chemical Techniques. CNR Firenze-Institute of Applied Physics "N.Carrara"

[58] S.Bassini (2012). Bronzi e bronzi dorati esposti all'azione della pioggia: corrosione ed inibizione. Doctoral thesis, University of Bologna

[59] L. Burgio, R. J.H. Clark (2001). Library of FT-Raman spectra of pigments, minerals, pigment media and varnishes, and supplement to existing library of Raman spectra of pigments with visible excitation. Spectrochimica Acta Part A, Vol. 57, pp.1491–1521

[60] J. Twu, C. J. Chuang, K. I Chang, C. H. Yang, K. H. Chen (1997). Raman spectroscopic studies on the sulfation of cerium oxide. Applied Catalysis B: Environmental, Vol. 12, pp. 309-324

[61] J.R. ShiU, X. Shi, Z. Sun, S.P. Lau, B.K. Tay, H.S. Tan (2001). Resonant Raman

studies of tetrahedral amorphous carbon films. Diamond and Related Materials, Vol. 10, pp.76-81

[62] ASM Handbook (1992). Au (Gold) Binary Alloy Phase Diagrams, *Alloy Phase Diagrams*, Vol 3, p 2.65–2.80

[63] G.Buccolieri, V. Nassisi, A. Buccolieri, F. Vona, A.Castellano (2013). Laser cleaning of a bronze bell. Applied Surface Science, Vol. 272, pp.55– 58

[64] R. Salimbeni, R. Pini, S. Siano (2013). A variable pulse width Nd:YAG laser for conservation. Journal of Cultural Heritage, Vol. 4, pp.72s–76s

[65] A. Kratschmer, I. Odnevall Wallinder, C. Leygraf (2002). The evolution of outdoor copper patina. Corrosion Science, Vol. 44, pp.425-450

[66] A. Mencaglia (2013), personal communication

[67] F. Tamassia (2013). Lecture of Spectroscopy and Cultural Heritage

[68] S. Daviero Minaud (2012). Lecture of Methodologies in inorganic chemistry

[69] HunterLab. June 5th 2011.
http://www.hunterlab.com/appnotes/an07_96a.pdf

[70] Wikipedia. June 6th 2011.
http://en.wikipedia.org/wiki/Color_difference

[71] C.M. Grossi, P. Brimblecombe, R. Esbert, F.J. Alonso (2007). Color changes in architectural limestones from pollution and cleaning. Color research and application, Vol. 32, pp.320 – 331.

[72] Wikipedia. June 1st. 2011.
http://en.wikipedia.org/wiki/Gloss_(material_appearance)

[73] M. Pollard, C. Heron (1996). Archaeological Chemistry. pp. 26 – 31

[74] Floréal Daniel
http://www.culture.gouv.fr/culture/conservation/fr/methodes/atome.htm

[75] D. Ciccarella (2009). Corrosione atmosferica del bronzo quaternario G85: Prove di invecchiamento artificiale. Alma Mater Studiorum – Università di Bologna, Facoltà di Chimica Industriale, pp. 132 – 139.

[76] S. Daviero Minaud (2012). Lecture of X-Ray Diffraction

Appendices A   Analytical techniques

Raman spectroscopy:

When an atomic or molecular sample is irradiated by an electromagnetic radiation, this can be absorbed if the energy carried by the radiation corresponds to the energy gap between two stationary levels of atoms or molecules.

If the energy radiation does not correspond to the energy gap, the radiation can be transmitted or scattered by the sample.

- If the collision between electromagnetic wave and the molecule is **elastic**, incident and scattered lights will have same frequency. It is the **Rayleigh scattering: $hv = hv_0$**.

- If the collision between the electromagnetic wave and the molecule is **anelastic**, there is a reemission, in every direction, of a very weak light (~10^{-8} times incident light intensity) that differs in energy from incident radiation. It is the **Raman scattering**.

In the Raman effect, the energies of the scattered photons are greater or lower of the incident energy and the difference corresponds to the differences between two ro-vibrational levels of the molecule.

It results in two different kind of lines:

- Stokes line: $hv = h(v_0 - v)$

- Anti-Stokes line: $hv = h(v_0 + v)$
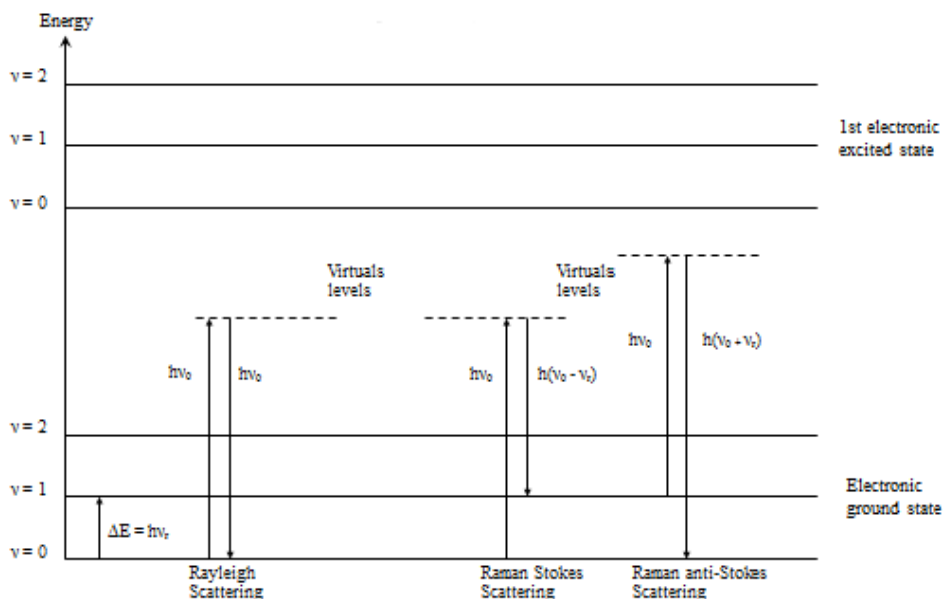
Figure 1: Rayleigh and Raman lines [67]
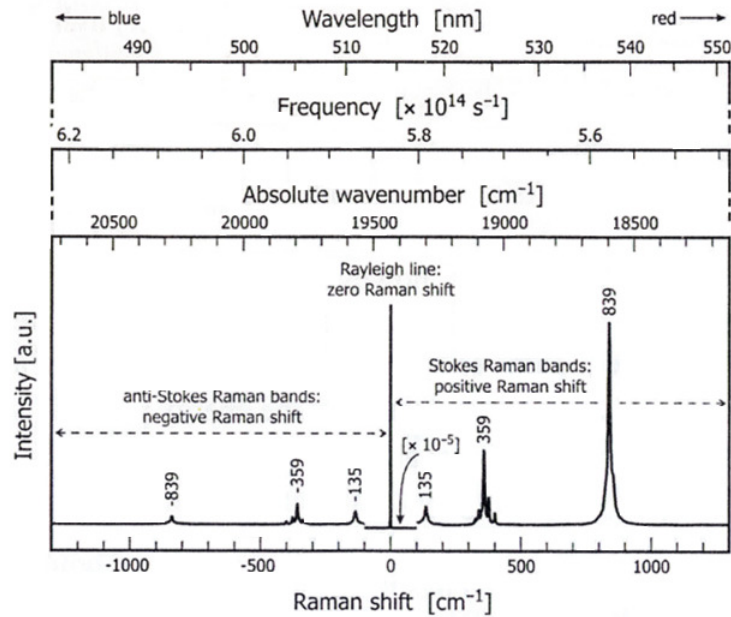
Figure 2: Raman and Rayleigh lines [67]

The stokes lines are more intense than Anti-Stokes lines because the initial state is more populated than in the case of Anti-Stokes lines. Thus, only the Stokes lines are taken into account when analysing a spectrum.

The Rayleigh line is the most intense line. A filter (like Notch filter) is used in order to cut it during the spectral acquisition.

In order for a molecular vibration to be Raman active, there must be a variation in the induced dipole moment resulting from a change in the polarizability α of the molecule.

Polarizability can be regarded as the measure of the flexibility of the electron cloud: the easiness with which the electron cloud of the molecule can be deformed or displaced to produce an electric dipole under the influence of the external electric field.

The classical theory of Rayleigh and Raman scattering is based on the concept that scattered light is generated by oscillating electric dipoles induced by the electric field of incident (exciting) radiation. The linear relation between the induced dipole moment vector μ_{ind} and the electric field vector $\boldsymbol{E}$ can be written:

$$\mu_{ind} = \alpha\boldsymbol{E}$$

Scanning electron microscopy + Energy dispersive spectroscopy:

The scanning electron microscope (SEM) scans a fine beam of electrons onto a specimen and collects the electrons scattered by the surface.

Electrons are reflected off the surface of the specimen as it has been previously coated by conductive material.

The reflected electron beams are focused on a fluorescent screen (or detector) in order to make up the image.

SEM principle:
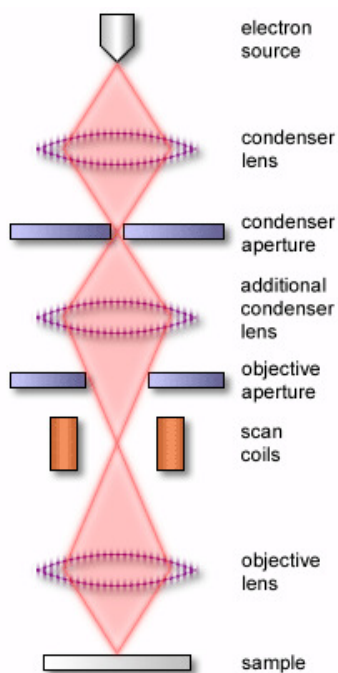
- An electron beam is produced at the top of the microscope by an electron gun.

- The electron beam follows a vertical path through the microscope, which is held into vacuum.

- The beam travels through electromagnetic fields and lenses which focus the beam down toward the sample.

- Once the beam hits the sample, electrons and X-rays are ejected from the sample.

Figure 3: SEM device [68]

Detectors collect these X-rays, backscattered electrons and secondary electrons. Then they convert them into a signal that is sent to a screen (example: computer screen). This produces the final image.
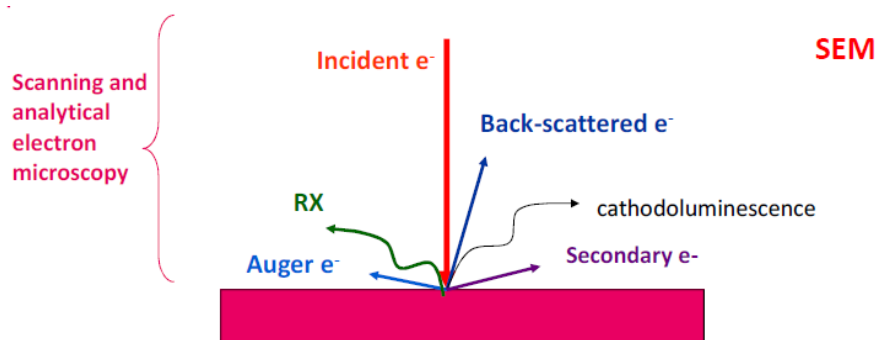
Figure 4 : interaction of light with the matter [68]

Some conditions are made on the sample in order to prevent its decomposition:

- It must be conductive to prevent charging

- It must be vacuum compatible

- It must not have a too high beam sensitivity

Signal detection: to be detected, the signal must not be absorbed.
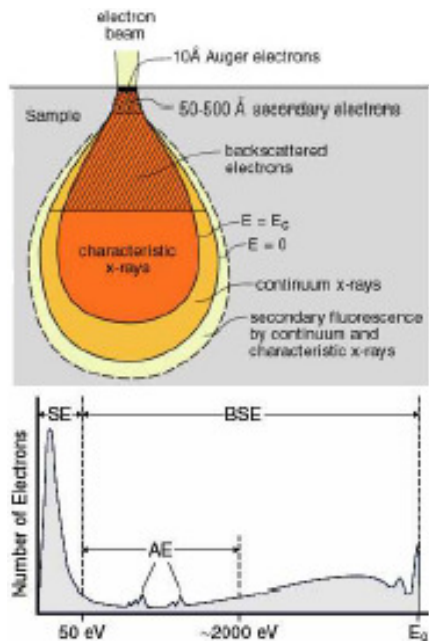
- Auger electrons emerge from a very thin region of the sample surface (maximum depth about 50Å).

- Secondary electrons (SE) form a large low-energy peak coming from the near surface.

- Backscattered electrons (BSE) come from a deeper region.

- Auger electrons (AE) produce relatively small peaks on the backscattered electron distribution.

Figure 6 : scheme of the signal detection [68]

Secondary electrons: it corresponds to the strongest peak in the electron energy spectrum (less than 50 eV). The electrons are generated throughout the region excited by the incident beam but only those that originate less than 1 nm deep in the sample can escape and be detected.

It is very sensitive to topography and can be used for surface images.

Backscattered electrons: they are very high energy primary electrons that suffer large angle (> 90°) scattering and re-emerge from the entry surface of a specimen. Their peak intensities are lower than the one of the primary electron beam.

They can be used for element scanning image where heavy elements will give a strong signal (light area) and weak ones will give a light signal (dark area).

CIELAB color scale and Gloss measurement:

The CIELAB scale is an approximately uniform color scale which is organized in a cube formed with three axes [69]:

- L* axis: A value of 100 represents a perfect reflecting diffuser, while 0 (zero) means black.

- a* axis: The more positive indicates more tendency to red; the more negative, to green.

- b* axis: The more positive indicates tendency to yellow; the more negative, to blue.

The color space of the CIELAB scale is illustrated in figure 7:
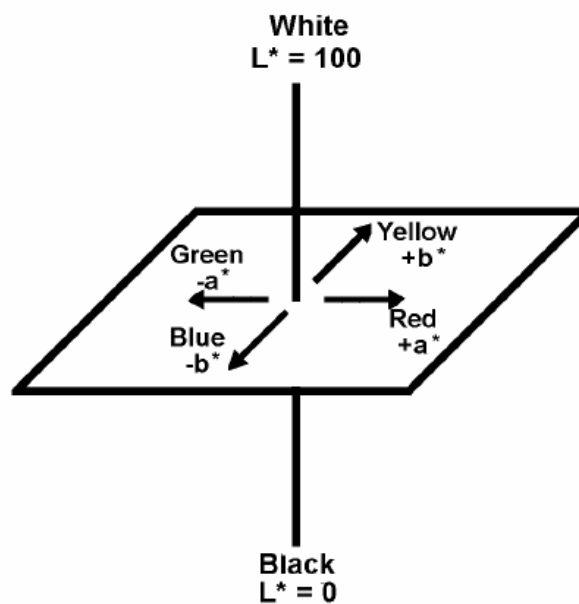
Figure 7: CIELAB color space [69]

The colour change can be expressed with the variable ΔE* which is the total colour difference. "E" means *Empfindung*, German for "sensation" [70]. ΔE* is calculated as:

$$\Delta E^* = \sqrt{(\Delta L*)^2 + (\Delta a*)^2 + (\Delta b*)^2}$$

It is a metric created by the International Commission of Illumination (CIE) which is used in certain fields where colour change is of importance. Moreover, the human eye is more sensitive to certain colours than others, which makes more critical the need for a metric to measure color change.

A value of ΔE* = 3 is considered as the "just noticeable difference" in the cultural heritage field [71], meaning that a value equal or over 3 represents a noticeable color change of the analyzed sample

Gloss measurement consists in determining the percentage of specularly reflected light after illuminating the surface with visible light at different angles (e.g. 20°, 60° and 85°). This percentage describes the ability of the surface to reflect light into the specular direction.
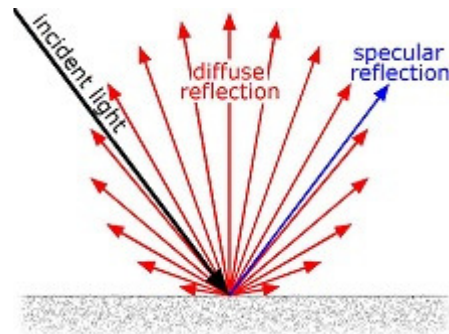
Figure 8: specular reflection scheme [72]

The specular reflection corresponds to the case where the angle of the incident light is equal and opposite to the angle of the reflected light.

The percentage of reflected light depends on the refractive index of the material, the angle of incident light and the surface topography. Materials with smooth surfaces appear glossy, while very rough surfaces reflect no specular light and therefore appear matt [72].

Atomic Absorption Spectroscopy (AAS):

The Atomic Absorption Spectroscopy studies the emissions or absorptions of light by a free atom (i. e. when its energy changes during the movement of one of its electron from an electronic orbital to another one).

AAS analysis is based on two main techniques which either use an arc or spark emission or use a flame. These techniques are used in analytical chemistry.

This technique requires samples in a liquid form and can only measure one element at a time. Moreover AAS analysis is an absorption technique and thus it is based on the Beer-Lambert law:

$$A= \varepsilon cl$$

Where:

- $A= \log(I_0/I)$

- I: transmitted light ($Js^{-1}cm^{-1}$)

- I_0: incident light ($Js^{-1}cm^{-1}$)

- ε: molar absorptivity coefficient ($Lmol^{-1}cm^{-1}$)

- c: concentration ($molL^{-1}$)

- l: path length through the atom cell (cm)

In figure 9, is a scheme of this analysis.
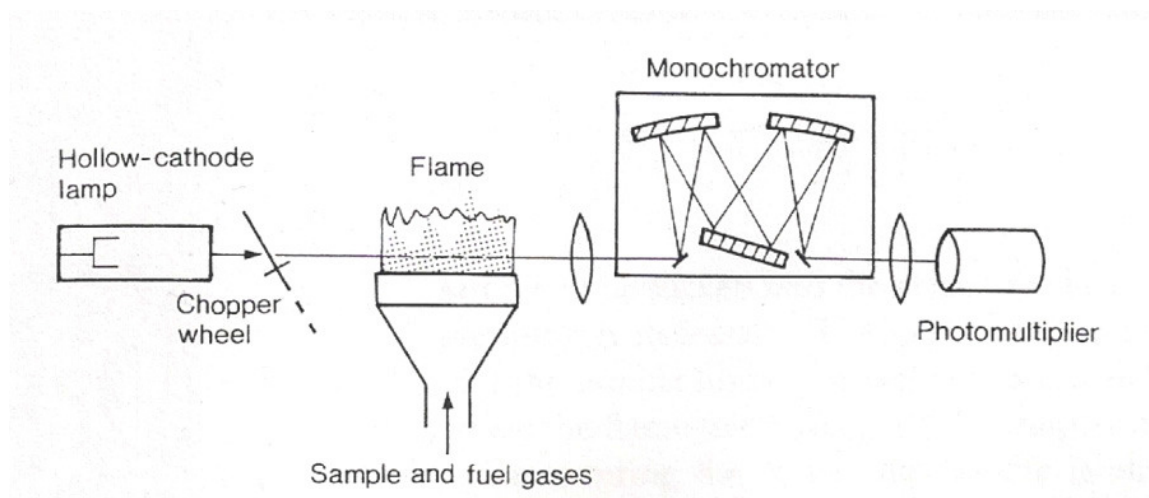
Figure 9: scheme of the AAS analysis [73]

It is composed of [74]:

- a source which is hollow-cathod lamp. It is made of a glass (or quartz) envelope filled with a noble gas at low pressure. Within the envelope, two electrodes (a wire and a hollow cup made from the element of interest) are present and are subjected to a potential difference of few hundred of volts resulting in the ionization of the noble gas. The created ions will interact with the cathode (the hollow cup) which begins to glow with the characteristic radiation of the element

- a nebulizer which spread a fog of the liquid solution into the burner

- a burner with a flame on the top. The spread solution enters the burner and then the flame. During this process, the solvent is eliminated and the remaining salts or solid particles are then melted, vaporized and atomized.

  Different kinds of flame exist such as the air/acetylene flame (which burns at about 2200 °C) or the N_2O/acetylene flame (which burns at around 3000 °C). Their use depends on the type of element to analyze since some elements need a higher temperature in order to ensure a complete atomization. Moreover, instead of a flame, a graphite furnace can be used for the atomization and sample analysis.

Figure 10: graphite furnace in the GF-AAS technique [20]

This graphite furnace is more sensitive than the flame and requires a lower quantity of sample to run the analysis [75].

- a monochromator which selects a particular wavelength for transmission onto the detector

- a detector which is a photomultiplier tube. The photomultiplier tube permits to convert the light emitted into an electric current signal

X-Ray Diffraction:

X-Ray photons are created by the interaction at the atomic level of high-energy beam of particles or photons with the matter.

The generation of characteristic X-Rays is based on the photoelectric effect:

- An incoming high-energy photoelectron dislodges a k-shell electron in the target atom. It results in a vacancy in the shell

- An outer shell electron jumps to fill the vacancy

- The jump energy results in the emission of a characteristic X-Ray
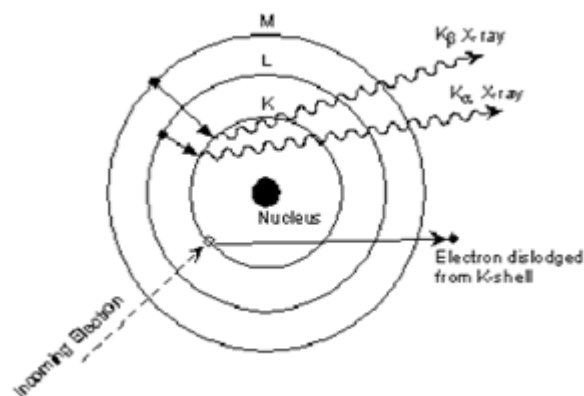
Figure 11: scheme of the characteristic X-Ray emission [76]

XRD is an important tool which permits to find the composition or the structure of a sample. One of its major domains of applications is the crystallography which is the study of solid samples as crystals.

Using X-Ray Diffraction, we can find the cell parameters of a crystal, and thus the Bravais lattice, but also the atomic positions of each atoms of the crystals.

The cell parameters can be find thanks to the Bragg's law:

$$2d\sin\theta = n\lambda$$

Where:

- d: distance between adjacent planes in the lattice

- θ: incident angle of the X-Ray beam

- n: integer

- λ: wavelength of the X-Rays
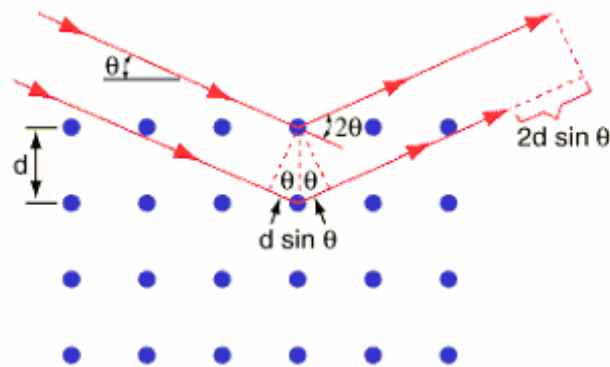
figure 12: description of the Bragg's law [76]

The diffraction condition is 2dsinθ = nλ.

2dsinθ corresponds to the path difference between ray 1 and ray 2 and the deviation is equal to 2θ.

We can notice that, in the Bragg's equation, the interatomic spacing along the plane does not appear in the equation but only the interplanar spacing d. Thus change in position or spacing of atoms along the plane should not affect Bragg's conditions.
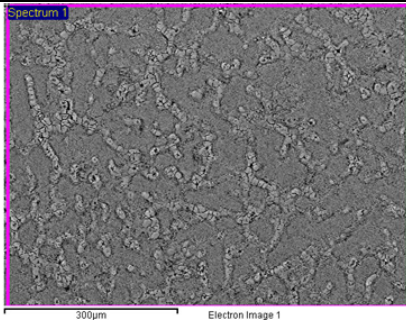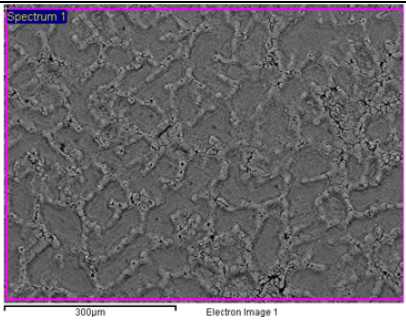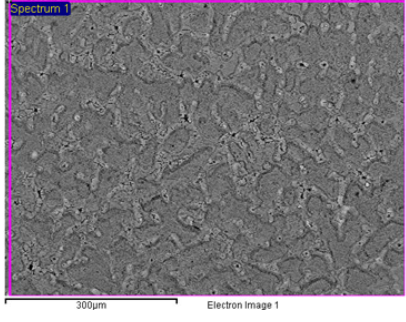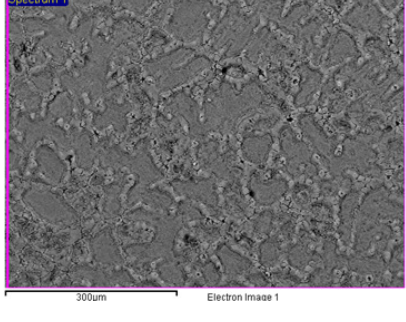
Bragg's law gives conditions needed for diffracting: X-Ray waves have to be in phase with each other (constructive interferences). If these conditions are not met there are destructives interferences which reduce the reflected intensity to zero.

For constructive interferences, the condition on the Bragg's law is that n is equal to an integer.
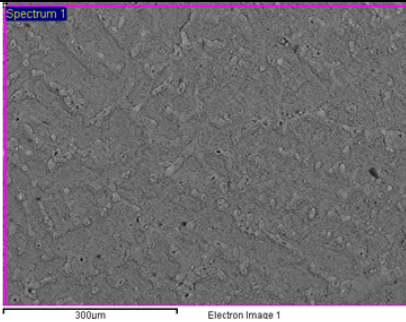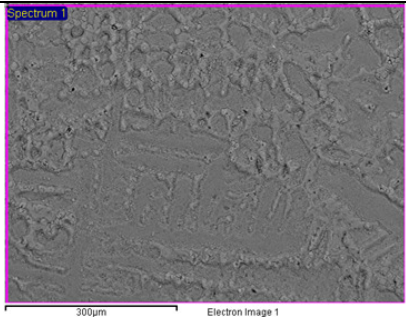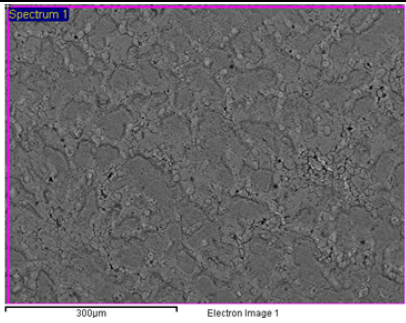
Appendices B   SEM-EDS analysis
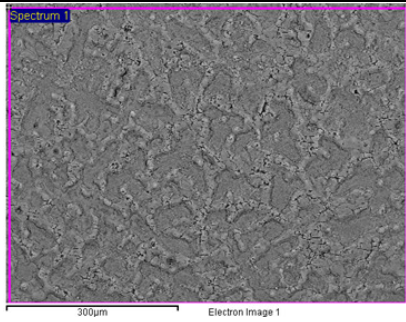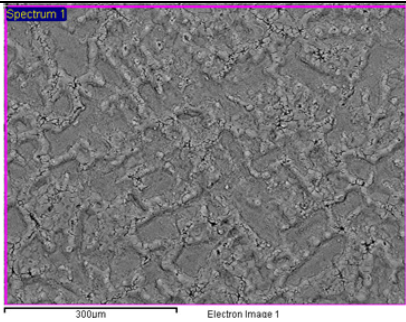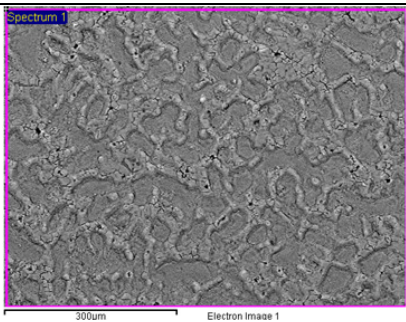
SEM-EDS analysis of non-gilded bronzes (section 1) :

Samples coated with PropS-SH+nanoparticles: 19 d TOW pre-patinated before coating		
sample	Site of interest	elements: Weight%
E		Element Weight% C K 3.29 N K 0.61 O K 21.61 Al K 0.25 Cl K 0.22 Cu K 57.47 Zn K 0.98 Sn L 14.11 Sb L 0.58 Pb M 0.89 Totals 100.00
		Element Weight% C K 3.67 N K -0.91 O K 25.87 Al K 0.40 Cu K 47.99 Zn K 0.81 Sn L 20.99 Pb M 1.18 Totals 100.00
		Element Weight% C K 4.18 O K 21.38 Cu K 58.29 Zn K 0.91 Sn L 14.19 Pb M 1.05 Totals 100.00
		Element Weight% C K 4.56 O K 23.81 Al K 0.28 Cu K 51.32 Zn K 0.91 Sn L 17.26 Sb L 0.76 Pb M 1.10 Totals 100.00
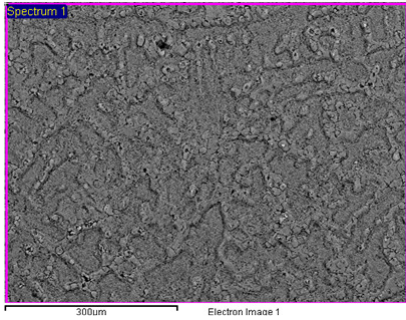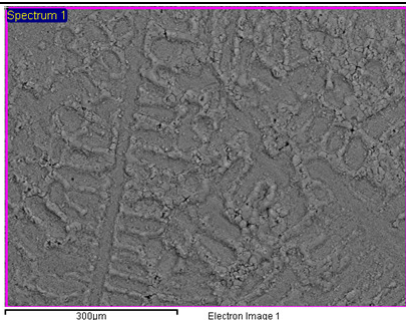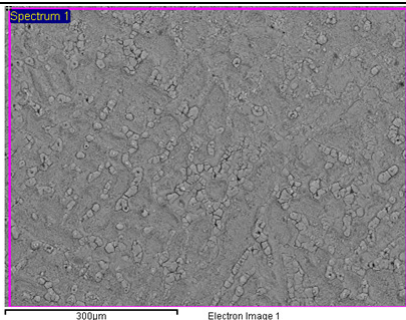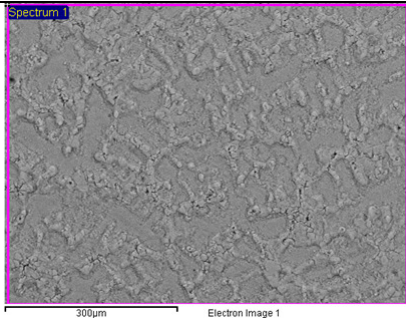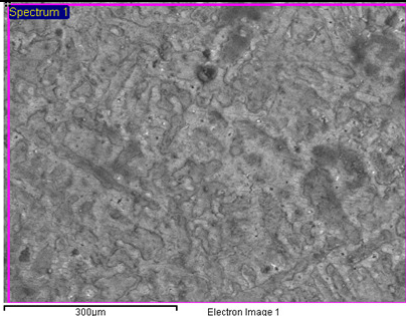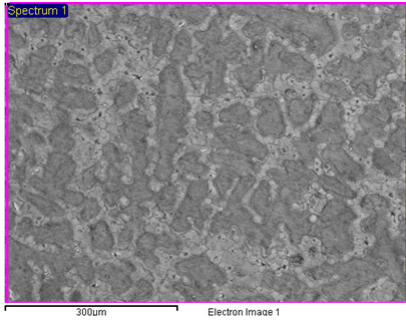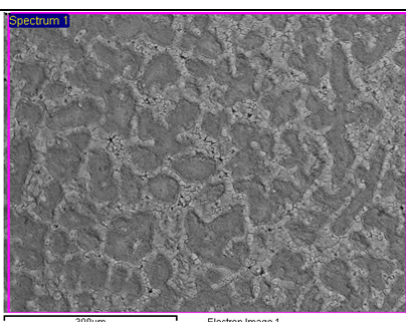
Samples coated with PropS-SH+nanoparticles: 19 d TOW pre-patinated before coating		
sample	Site of interest	elements: Weight%
F		Element / Weight% C K / 5.64 N K / -0.57 O K / 20.61 Al K / 0.26 Cl K / 0.24 Cu K / 59.54 Zn K / 0.92 Sn L / 12.42 Pb M / 0.93 Totals / 100.00
		Element / Weight% C K / 5.83 O K / 21.17 Cl K / 0.22 Cu K / 56.39 Zn K / 0.87 Sn L / 14.38 Pb M / 1.14 Totals / 100.00
		Element / Weight% C K / 4.07 N K / 2.69 O K / 21.64 Al K / 0.34 Cl K / 0.17 Cu K / 54.31 Zn K / 0.93 Sn L / 14.44 Sb L / 0.64 Pb M / 0.77 Totals / 100.00
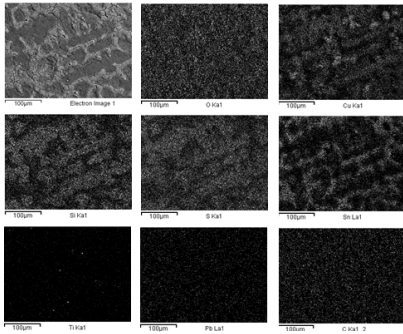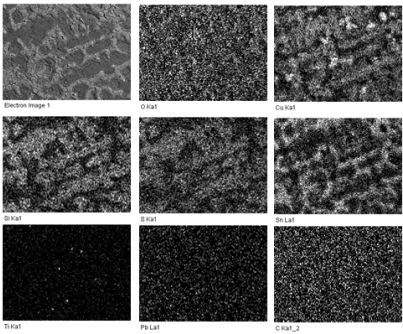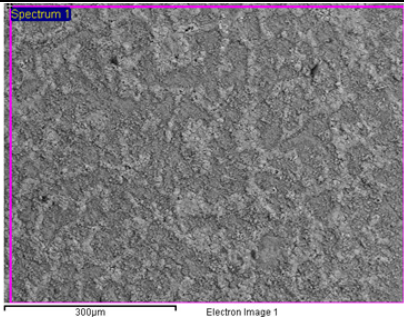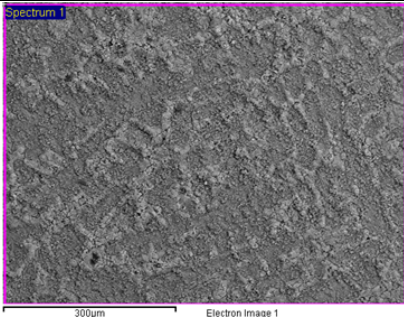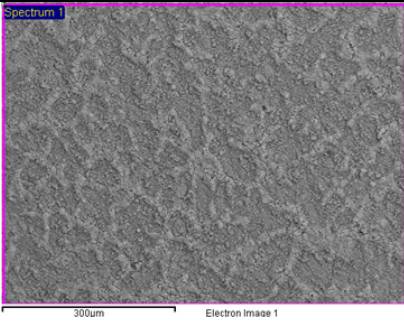
Samples coated with PropS-SH+nanoparticles: 19 d TOW pre-patinated before coating		
sample	Site of interest	elements: Weight%
G		Element	Weight%
		C K	4.48
		N K	2.92
		O K	24.82
		Cl K	0.22
		Cu K	46.49
		Zn K	0.72
		Sn L	18.68
		Sb L	0.69
		Pb M	0.98
		Totals	100.00

Spectrum 1 — Electron Image 1 — 300µm

Element	Weight%
C K	4.74
O K	24.38
Al K	0.21
Cl K	0.19
Cu K	49.08
Zn K	0.76
Sn L	19.36
Pb M	1.28
Totals	100.00

Spectrum 1 — Electron Image 1 — 300µm

Element	Weight%
C K	5.95
O K	22.70
Cl K	0.20
Cu K	52.48
Zn K	0.90
Sn L	16.79
Pb M	0.98
Totals	100.00

Spectrum 1 — Electron Image 1 — 300µm
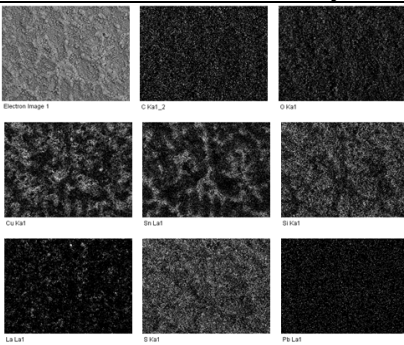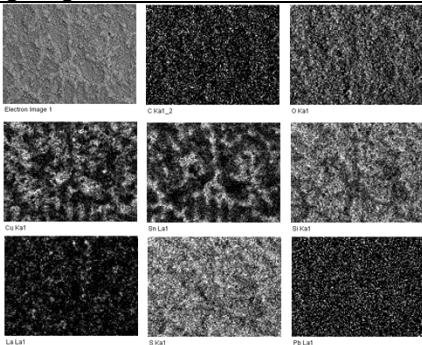
Samples coated with PropS-SH+nanoparticles: 22 d TOW pre-patinated before coating		
sample	Site of interest	elements: Weight%
F		Element | Weight% C K | 7.53 O K | 20.01 Cu K | 56.98 Zn K | 0.81 Sn L | 13.83 Pb M | 0.84 Totals | 100.00
		Element | Weight% C K | 6.50 O K | 22.27 Cl K | 0.23 Cu K | 53.43 Sn L | 16.51 Pb M | 1.06 Totals | 100.00
		Element | Weight% C K | 7.05 O K | 22.57 Al K | 0.30 Cu K | 51.56 Zn K | 0.70 Sn L | 16.80 Pb M | 1.03 Totals | 100.00
		Element | Weight% C K | 6.01 O K | 23.03 S K | 0.22 Cl K | 0.22 Cu K | 51.00 Zn K | 0.81 Sn L | 17.91 Pb M | 0.80 Totals | 100.00
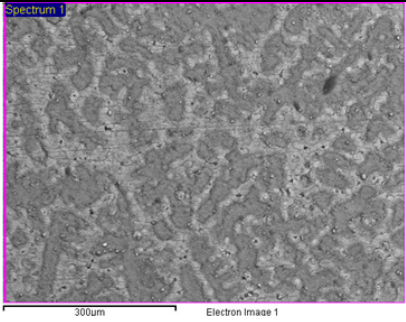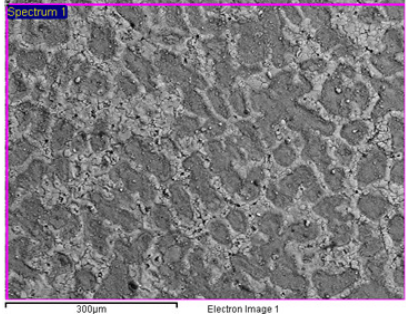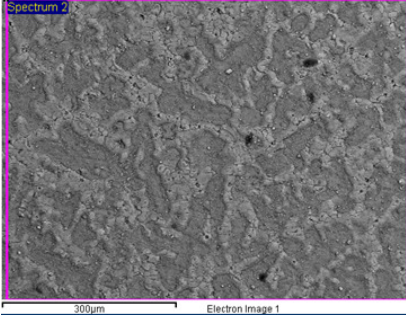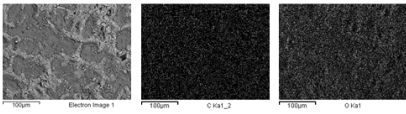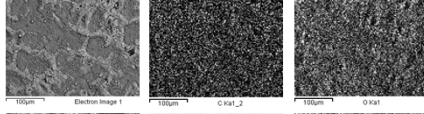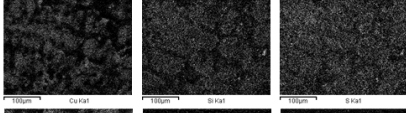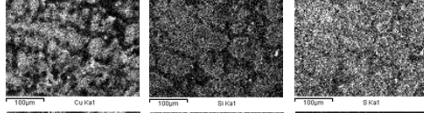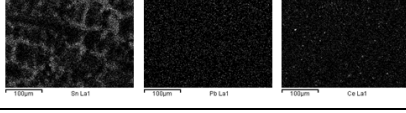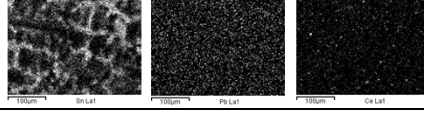
sample prepatinated and coated with PropS-SH+nanoparticles: 0d TOW-before cycle of ageing		
sample	Site of interest	elements: Weight%
E		Element / Weight% C K 18.73 O K 22.47 Si K 8.27 S K 7.62 Cl K 0.21 Ca K 0.34 Ti K 0.57 Cu K 32.07 Sn L 8.69 Sb L 1.03 Totals 100.00
		Element / Weight% C K 16.16 O K 23.67 Al K 0.24 Si K 7.63 S K 7.10 Ti K 0.44 Cu K 32.39 Sn L 10.85 Sb L 1.30 Pb M 0.21 Totals 100.00
		Element / Weight% C K 11.31 O K 27.91 Al K 0.27 Si K 4.48 S K 4.83 Cl K 0.21 Ti K 0.38 Cu K 32.51 Sn L 15.82 Sb L 1.96 Pb M 0.31 Totals 100.00
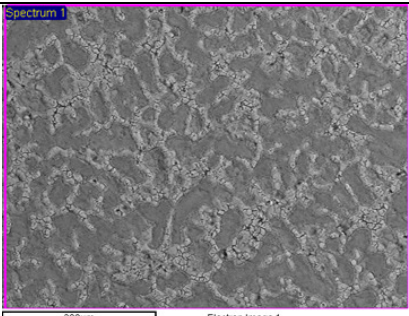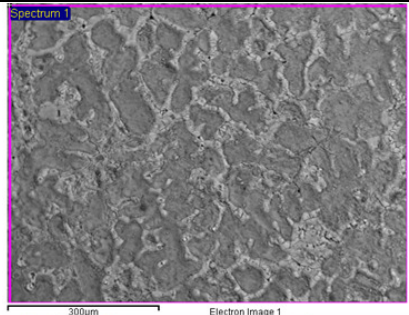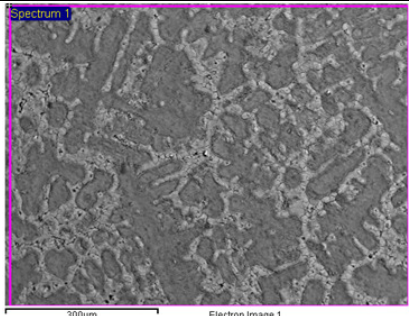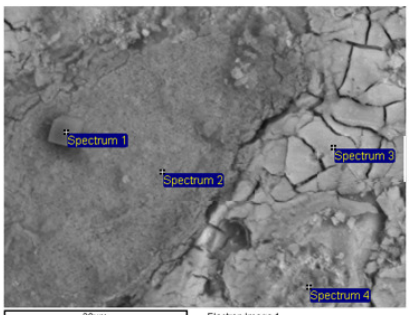
sample prepatinated and coated with PropS-SH+nanoparticles: 0d TOW-before cycle of ageing	
E	
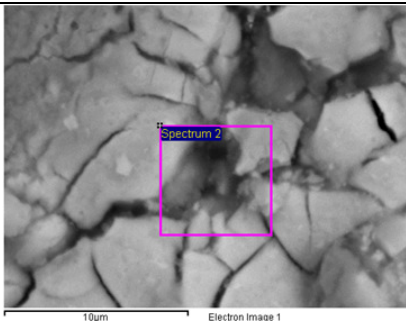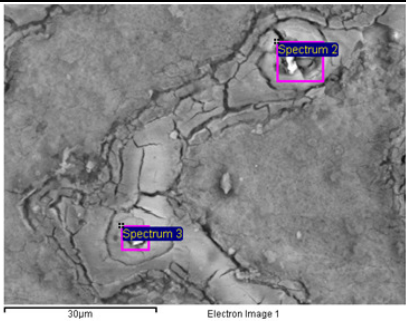
sample prepatinated and coated with PropS-SH+nanoparticles: 0d TOW-before cycle of ageing		
sample	Site of interest	elements: Weight%
F		Element Weight% C K 12.90 O K 30.49 Si K 5.87 S K 6.39 Cu K 24.87 Sn L 13.48 Sb L 1.72 La L 3.82 Pb M 0.47 Totals 100.00
		Element Weight% C K 13.99 O K 32.53 Si K 6.03 S K 6.74 Cu K 20.25 Sn L 15.09 Sb L 1.39 La L 3.63 Pb M 0.36 Totals 100.00
		Element Weight% C K 12.50 O K 32.63 Si K 5.69 S K 6.58 Cu K 20.69 Sn L 15.32 Sb L 1.58 La L 4.57 Pb M 0.46 Totals 100.00
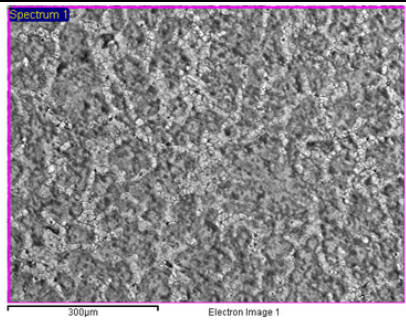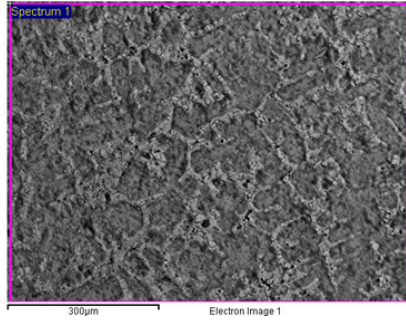
sample prepatinated and coated with PropS-SH+nanoparticles: 0d TOW-before cycle of ageing	
F	
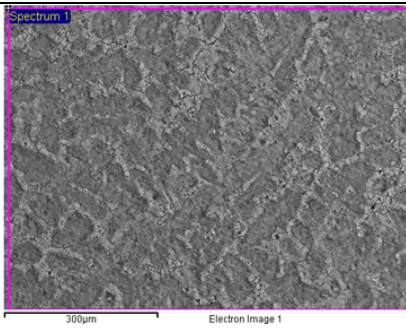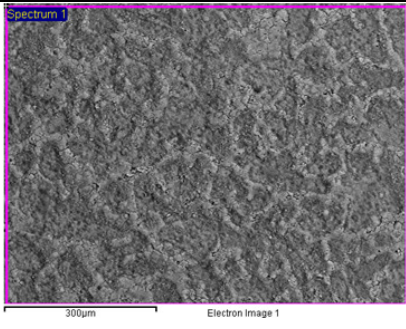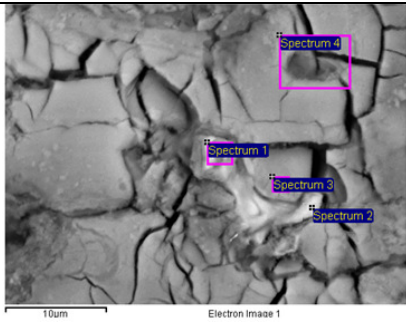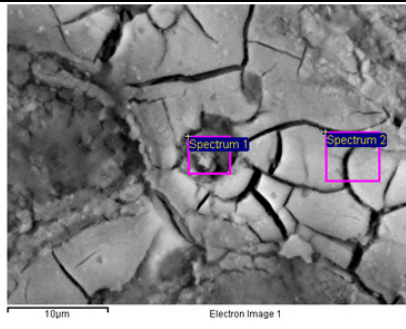
sample prepatinated and coated with PropS-SH+nanoparticles: 0d TOW-before cycle of ageing		
sample	Site of interest	elements: Weight%
G		**Element** — **Weight%** C K — 15.01 O K — 26.17 Si K — 7.55 S K — 7.24 Cu K — 30.39 Sn L — 12.55 Ce L — 1.10 Totals — 100.00
		Element — **Weight%** C K — 15.27 O K — 28.88 Si K — 5.80 S K — 5.87 Cl K — 0.16 Cu K — 26.53 Sn L — 14.62 Sb L — 1.69 Ce L — 1.09 Pb M — 0.09 Totals — 100.00
		Element — **Weight%** C K — 15.42 O K — 28.90 Si K — 5.34 S K — 5.38 Cl K — 0.13 Cu K — 27.97 Sn L — 13.91 Sb L — 1.61 Ce L — 1.03 Pb M — 0.30 Totals — 100.00
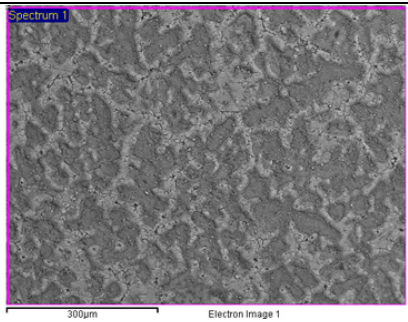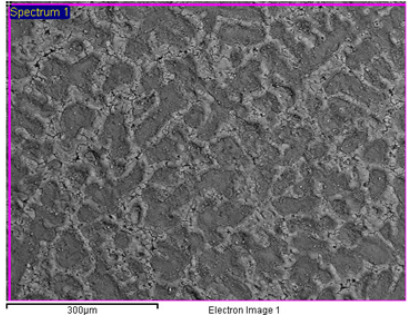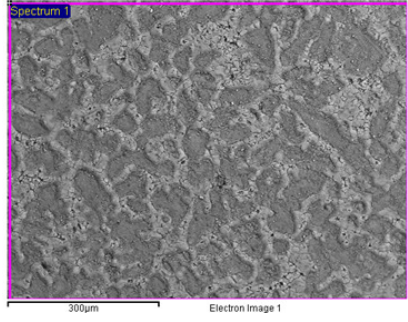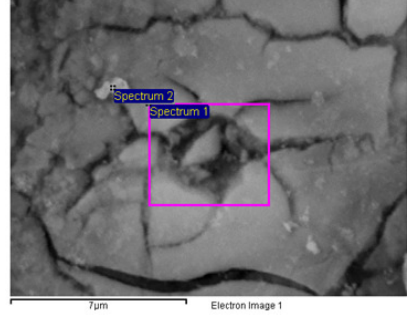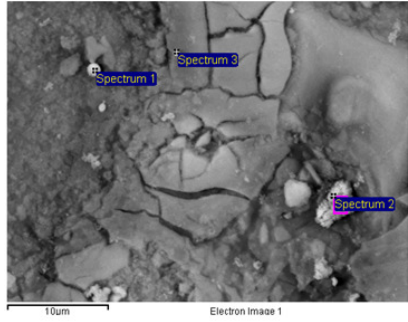
sample prepatinated and coated with PropS-SH+nanoparticles: 0d TOW-before cycle of ageing	
G	
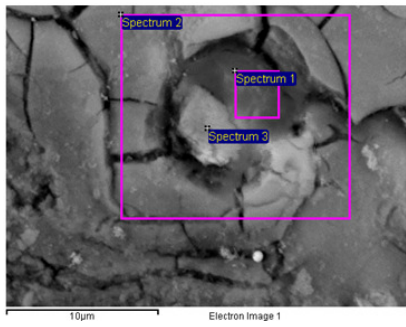
sample prepatinated and coated with PropS-SH+nanoparticles: 10d TOW- ageing		

sample	Site of interest	elements: Weight%

Element	Weight%
O K	26.05
Al K	0.23
Si K	5.50
S K	5.45
Ti K	0.28
Cu K	41.61
Sn L	20.81
Pb M	0.06
Totals	100.00

Element	Weight%
C K	11.49
O K	23.80
Al K	0.18
Si K	6.49
S K	6.34
Ti K	0.51
Cu K	38.23
Sn L	12.96
Totals	100.00

E

Element	Weight%
C K	11.60
O K	24.57
Al K	0.20
Si K	6.12
S K	6.15
Ti K	0.48
Cu K	36.96
Sn L	13.94
Totals	100.00

Element	Weight% Spectrum 1	Weight% Spectrum 2	Weight% Spectrum 3	Weight% Spectrum 4
C K	8.17	5.26		5.63
O K	47.37	16.74	31.62	19.85
Na K	1.93			
Al K	0.16			
Si K	3.33	7.63	2.38	8.08
S K	17.42	6.89	3.11	6.56
Ca K	13.07			
Ti K	0.39		0.09	1.42
Cu K	5.59	57.18	25.14	54.72
Zn K	0.04			
Sn L	2.53	5.67	36.50	3.54
Cl K		0.53	0.24	0.20
Pb M			1.02	
Totals	100.00	100.00	100.00	100.00
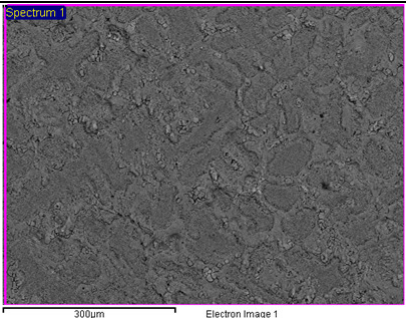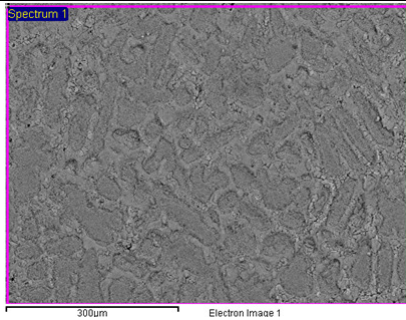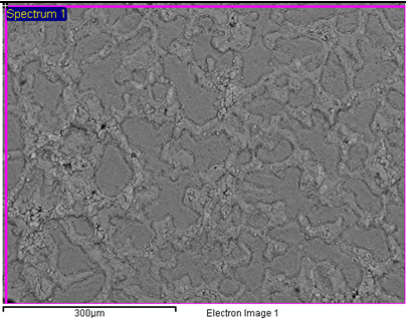
sample prepatinated and coated with PropS-SH+nanoparticles: 10d TOW- ageing		
sample	Site of interest	elements: Weight%
E		Element	Weight%
C K	9.91
O K	31.60
Al K	0.23
Si K	6.64
S K	7.69
Ti K	1.03
Cu K	15.26
Sn L	27.44
Pb M	0.20
Totals	100.00	

Sample E — first site

Element	Weight%
C K	9.91
O K	31.60
Al K	0.23
Si K	6.64
S K	7.69
Ti K	1.03
Cu K	15.26
Sn L	27.44
Pb M	0.20
Totals	100.00

Sample E — second site

Element	Weight% Spectrum 2	Weight% Spectrum 3
C K	12.11	9.09
O K	28.09	28.84
Al K		0.24
Si K	4.56	4.18
S K	5.04	4.75
Ti K	0.57	0.24
Cu K	23.71	27.79
Sn L	25.44	24.54
Pb M	0.47	0.34
Totals	100.00	100.00
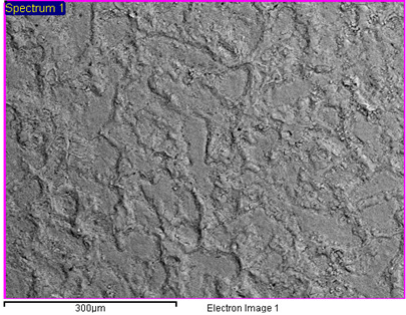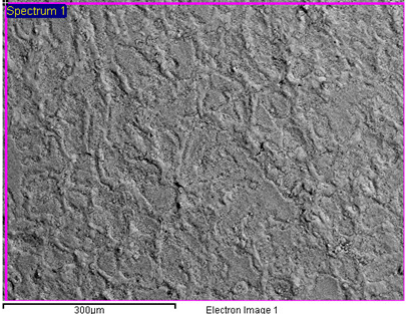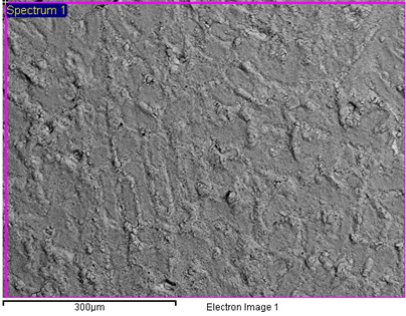
sample prepatinated and coated with PropS-SH+nanoparticles: 10d TOW- ageing	
sample	Site of interest / elements: Weight%

Sample F — first site

Element	Weight%
C K	13.21
O K	23.05
Si K	8.84
S K	8.26
Cu K	32.64
Zn K	0.04
Sn L	13.85
La L	0.11
Totals	100.00

Sample F — second site

Element	Weight%
C K	11.50
O K	21.34
Si K	8.04
S K	7.33
Ca K	0.12
Cu K	37.99
Zn K	0.06
Sn L	12.19
Sb L	1.38
La L	0.06
Totals	100.00

sample prepatinated and coated with PropS-SH+nanoparticles: 10d TOW- ageing		
sample	Site of interest	elements: Weight%

Element	Weight%
C K	12.53
O K	23.95
Al K	0.11
Si K	7.30
S K	6.98
Cu K	34.03
Sn L	14.98
La L	0.11
Totals	100.00

Element	Weight%
C K	12.07
O K	24.23
Si K	6.88
S K	6.79
Cu K	34.37
Zn K	0.07
Sn L	15.50
La L	0.09
Totals	100.00

F

Element	Weight% Spectrum 1	Weight% Spectrum 2	Weight% Spectrum 3	Weight% Spectrum 4
C K	9.07			7.85
O K	27.12	39.92	38.30	25.60
Si K	3.32	3.65	3.24	4.06
S K	3.16	4.17	3.68	4.61
Ca K	0.16			0.38
Cu K	25.25	23.90	14.19	22.19
Sn L	24.92	27.55	39.67	31.47
Sb L	6.71			3.34
Pb M	0.29	0.81	0.89	0.46
Zn K			0.01	0.04
Totals	100.00	100.00	100.00	100.00

Element	Weight% Spectrum 1	Weight% Spectrum 2
C K	10.84	10.28
O K	24.59	30.63
Si K	7.91	5.65
S K	8.34	5.97
Cu K	21.26	19.75
Sn L	26.86	27.31
Pb M	0.21	0.41
Totals	100.00	100.00

sample prepatinated and coated with PropS-SH+nanoparticles: 10d TOW- ageing		
sample	Site of interest	elements: Weight%

sample		
		Element	Weight%
		C K	12.22
		O K	28.59
		Si K	6.68
		S K	6.93
		Cu K	26.30
		Sn L	18.22
		Ce L	1.06
		Totals	100.00

Image 1 (Spectrum 1, scale 300µm, Electron Image 1):

Element	Weight%
C K	12.22
O K	28.59
Si K	6.68
S K	6.93
Cu K	26.30
Sn L	18.22
Ce L	1.06
Totals	100.00

Image 2 (Spectrum 1, scale 300µm, Electron Image 1):

Element	Weight%
C K	11.39
O K	28.03
Si K	5.84
S K	6.10
Cu K	30.93
Sn L	16.67
Ce L	1.05
Pb M	-0.01
Totals	100.00

Image 3 — sample G (Spectrum 1, scale 300µm, Electron Image 1):

Element	Weight%
C K	12.09
O K	27.30
Si K	5.81
S K	5.88
Cu K	32.31
Sn L	15.62
Ce L	0.90
Pb M	0.09
Totals	100.00

Image 4 (Spectrum 1, Spectrum 2, scale 7µm, Electron Image 1):

Element	Weight% Spectrum 1	Weight% Spectrum 2
C K	8.42	9.52
O K	28.00	23.11
Si K	5.11	6.04
S K	5.28	6.82
Cu K	23.29	30.84
Sn L	28.55	22.59
Ce L	0.90	0.68
Pb M	0.45	0.39
Totals	100.00	100.00

Image 5 (Spectrum 1, Spectrum 2, Spectrum 3, scale 10µm, Electron Image 1):

Element	Weight% Spectrum 1	Weight% Spectrum 2	Weight% Spectrum 3
C K	10.93	10.10	6.59
O K	29.62	22.39	20.26
Al K	1.75		
Si K	4.75	5.84	3.99
S K	4.16	5.75	5.11
Ti K	12.34		
Cu K	19.91	15.82	34.07
Sn L	4.81	4.73	29.11
Ce L	11.72	35.39	0.31
Pb M			0.57
Totals	100.00	100.00	100.00
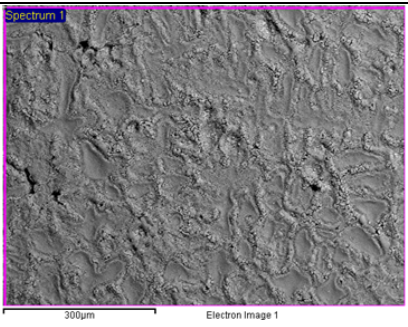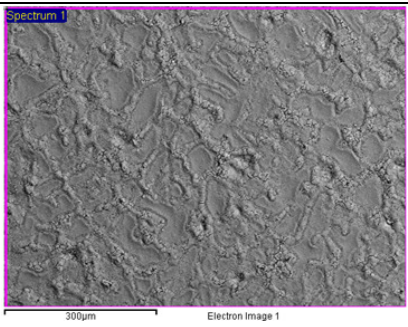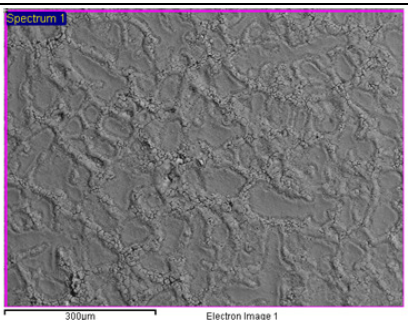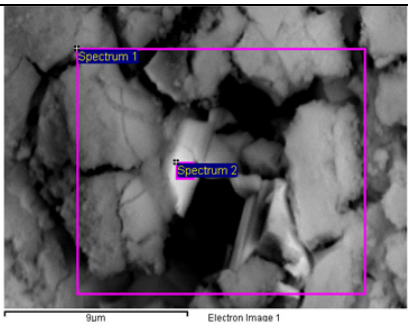
sample prepatinated and coated with PropS-SH+nanoparticles: 10d TOW- ageing			
sample	Site of interest	elements: Weight%	

Sample G

Element	Weight% Spectrum 1	Weight% Spectrum 2	Weight% Spectrum 3
C K	29.52	16.17	24.45
O K	18.31	25.22	29.06
Si K	2.42	2.98	2.60
S K	3.36	3.50	2.94
Ca K	0.15		
Cu K	25.43	25.46	14.64
Sn L	16.42	25.55	25.53
Sb L	3.97		
Ce L	0.34	0.58	0.50
Pb M	0.08	0.54	0.27
Totals	100.00	100.00	100.00
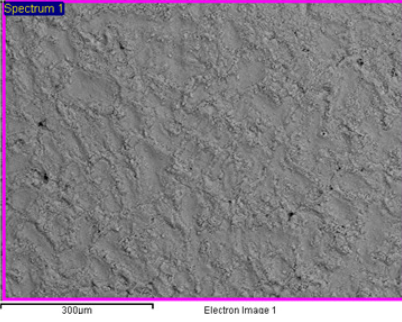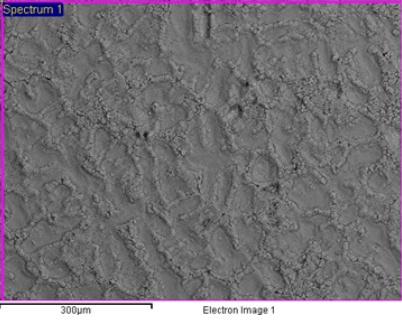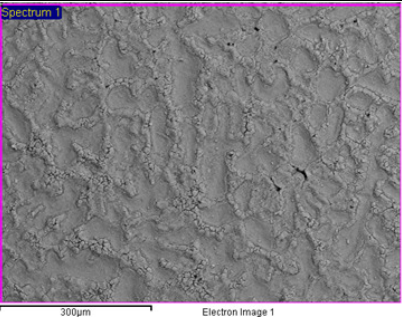
sample uncoated: 18d TOW-cycle of pre-patination		
sample	Site of interest	elements: Weight%

Sample H

Element	Weight%
C K	3.58
N K	4.03
O K	19.56
Cl K	0.24
Cu K	60.66
Zn K	0.58
Sn L	9.23
Sb L	1.41
Pb M	0.71
Totals	100.00

Element	Weight%
C K	4.19
O K	20.87
Cu K	60.82
Sn L	12.05
Sb L	1.37
Pb M	0.71
Totals	100.00

Element	Weight%
C K	3.91
N K	2.79
O K	21.75
Cl K	0.22
Cu K	56.83
Sn L	12.82
Sb L	1.66
Totals	100.00

sample uncoated : 22d TOW-cycle of pre-patination		
sample	Site of interest	elements: Weight%
H		Element	Weight%
		C K	7.42
		N K	3.02
		O K	24.39
		S K	0.09
		Cl K	0.29
		Cu K	52.81
		Zn K	0.45
		Sn L	9.49
		Sb L	1.30
		Pb M	0.74
		Totals	100.00

sample uncoated : 22d TOW-cycle of pre-patination

sample	Site of interest	elements: Weight%

Site 1 (sample H)

Element	Weight%
C K	7.42
N K	3.02
O K	24.39
S K	0.09
Cl K	0.29
Cu K	52.81
Zn K	0.45
Sn L	9.49
Sb L	1.30
Pb M	0.74
Totals	100.00

Site 2

Element	Weight%
C K	7.18
O K	21.99
Cl K	0.25
Cu K	58.82
Sn L	9.53
Sb L	1.50
Pb M	0.72
Totals	100.00

Site 3

Element	Weight%
C K	7.29
N K	1.39
O K	24.05
Cl K	0.20
Cu K	53.65
Sn L	11.42
Sb L	1.26
Pb M	0.73
Totals	100.00
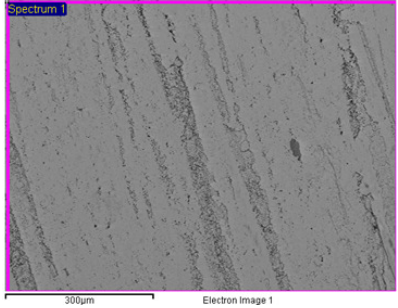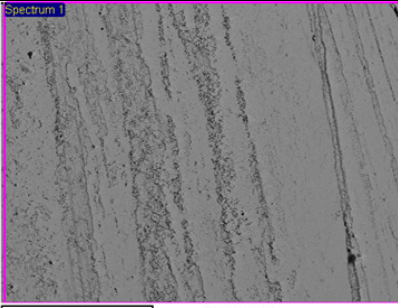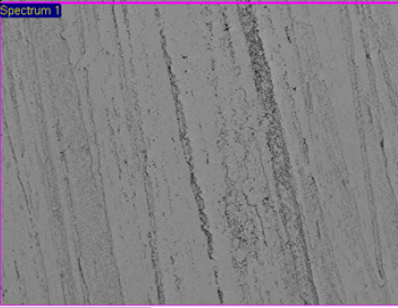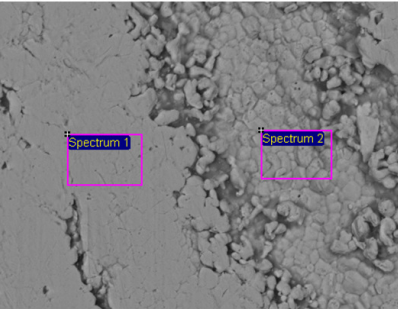
sample uncoated : 25d TOW-cycle of pre-patination			
sample	Site of interest	elements: Weight%	Elements: Weight% without C
H		Element	Weight% C K	6.66 O K	19.60 Cl K	0.20 Cu K	59.76 Zn K	0.63 Sn L	11.45 Sb L	1.70 Totals	100.00	Element	Weight% O K	20.42 Cl K	0.22 Cu K	64.30 Zn K	0.68 Sn L	12.53 Sb L	1.85 Totals	100.00

Site 1 (spectrum table):

Element	Weight%
C K	6.66
O K	19.60
Cl K	0.20
Cu K	59.76
Zn K	0.63
Sn L	11.45
Sb L	1.70
Totals	100.00

Element	Weight%
O K	20.42
Cl K	0.22
Cu K	64.30
Zn K	0.68
Sn L	12.53
Sb L	1.85
Totals	100.00

Site 2 (spectrum table):

Element	Weight%
C K	7.64
N K	0.00
O K	19.72
Cl K	0.26
Cu K	59.19
Zn K	0.54
Sn L	10.97
Sb L	1.68
Totals	100.00

Element	Weight%
N K	0.00
O K	20.53
Cl K	0.29
Cu K	64.53
Zn K	0.59
Sn L	12.20
Sb L	1.86
Totals	100.00

Site 3 (spectrum table):

Element	Weight%
C K	7.55
O K	18.89
S K	0.20
Cl K	0.19
Cu K	61.54
Zn K	0.68
Sn L	9.70
Sb L	1.25
Totals	100.00

Element	Weight%
O K	19.68
S K	0.23
Cl K	0.21
Cu K	66.99
Zn K	0.74
Sn L	10.77
Sb L	1.39
Totals	100.00
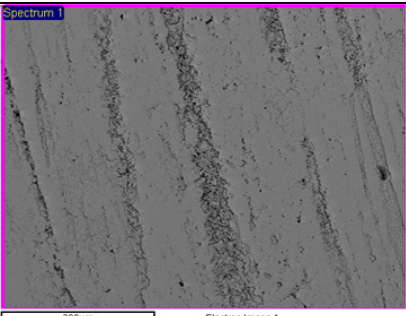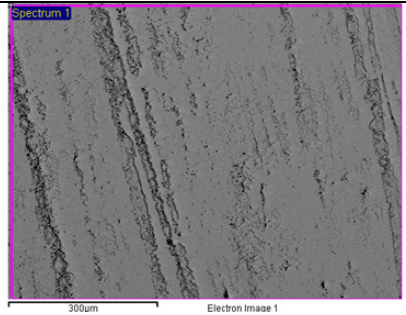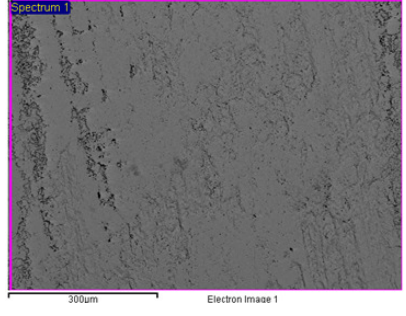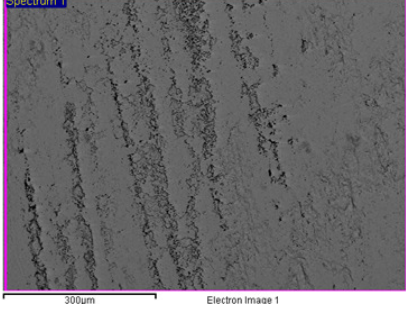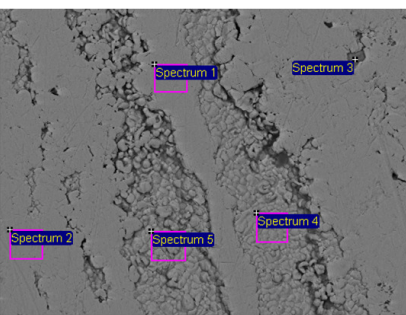
sample uncoated : 31d TOW-cycle of pre-patination		
sample	Site of interest	elements: Weight%

Element	Weight%
O K	26.15
S K	0.15
Cl K	0.24
Cu K	55.13
Sn L	17.48
Pb M	0.85
Totals	100.00

Element	Weight%
O K	25.64
S K	0.17
Cl K	0.29
Cu K	55.35
Sn L	17.64
Pb M	0.91
Totals	100.00

Element	Weight%
O K	27.08
S K	0.17
Cl K	0.24
Cu K	52.29
Sn L	19.33
Pb M	0.88
Totals	100.00

sample: H

Element	Weight% Spectrum 1	Weight% Spectrum 2
O K	25.30	6.42
S K	0.19	
Ca K	0.24	
Cu K	34.89	55.17
Sn L	32.84	24.73
Sb L	5.41	13.24
Pb M	1.12	0.44
Totals	100.00	100.00

sample uncoated : 10d TOW-ageing		
sample	Site of interest	elements: Weight%
H		Element / Weight% C K / 9.15 N K / 2.96 O K / 22.32 Cl K / 0.18 Cu K / 48.17 Zn K / 0.96 Sn L / 14.82 Sb L / 0.59 Pb M / 0.85 Totals / 100.00
		Element / Weight% C K / 9.32 N K / -0.99 O K / 25.96 Cu K / 42.72 Sn L / 21.87 Pb M / 1.12 Totals / 100.00
		Element / Weight% C K / 9.28 O K / 24.06 Cl K / 0.23 Cu K / 44.76 Zn K / 0.86 Sn L / 18.86 Sb L / 0.65 Pb M / 1.30 Totals / 100.00
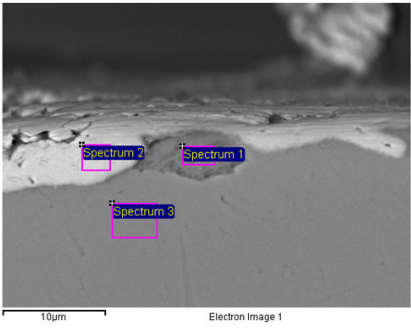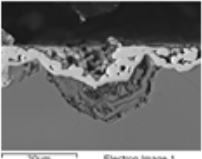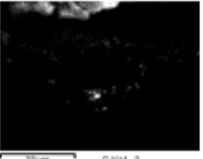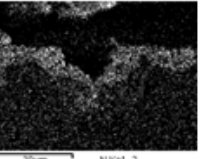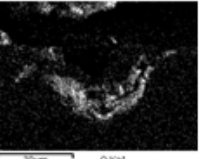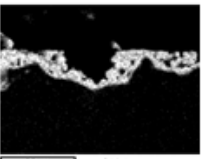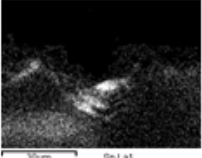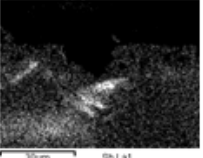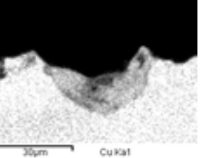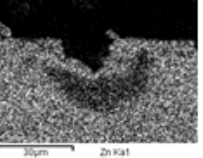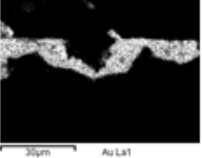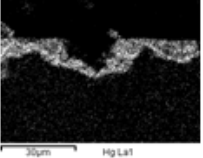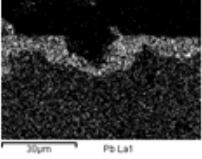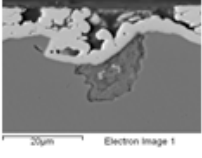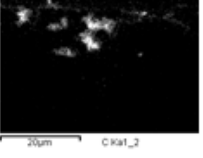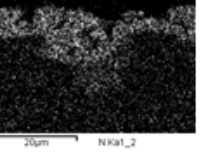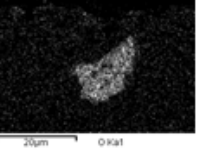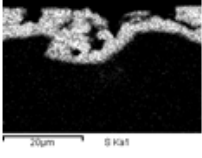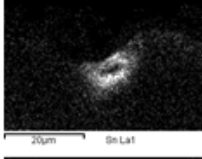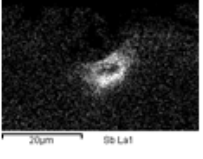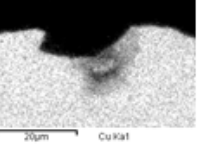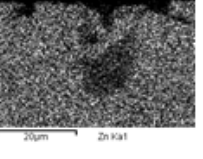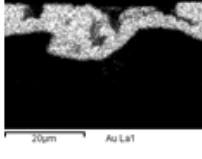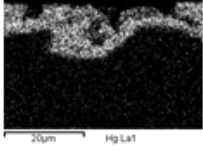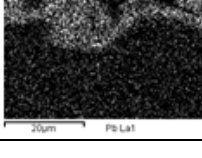
SEM- EDS analysis of gilded bronzes (section 2):
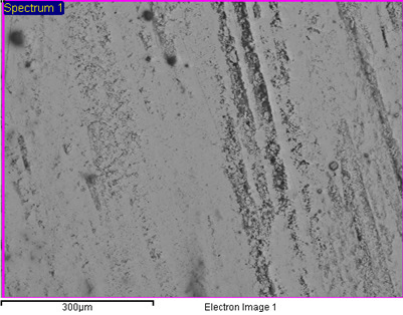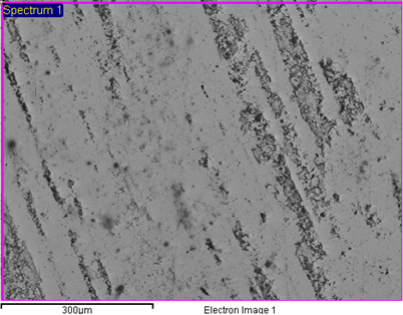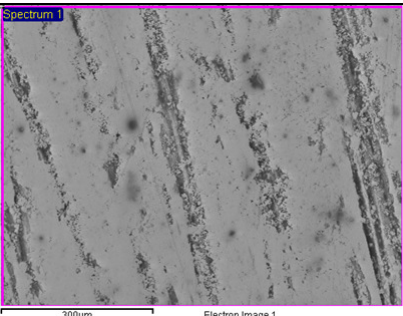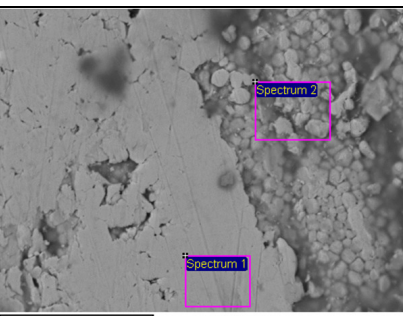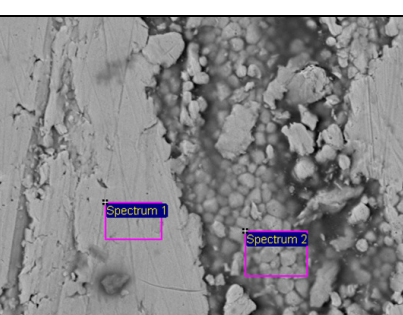
Samples uncoated: 0d TOW-before cycle of ageing		
sample	Site of interest	elements: Weight%
Uncoated		Element / Weight% C K 7.42 O K 1.82 Cu K 3.70 Au M 77.75 Hg M 9.31 Totals 100.00
		Element / Weight% C K 8.43 N K 3.98 O K 2.18 Cu K 3.96 Au M 72.63 Hg M 8.82 Totals 100.00
		Element / Weight% C K 8.29 O K 2.42 Cu K 8.88 Au M 72.26 Hg M 8.16 Totals 100.00
		Element / Weight% Spectrum 1 / Weight% Spectrum 2 C K 3.77 / 7.65 N K 4.32 / 4.18 O K / 3.26 Cu K 4.47 / 3.63 Au M 77.93 / 71.15 Hg M 9.51 / 10.14 Totals 100.00 / 100.00

	Samples uncoated: 10d TOW- ageing	
sample	Site of interest	elements: Weight%

Uncoated		Element / Weight% C K 7.40 O K 1.84 Cl K 0.15 Cu K 2.72 Sn L 0.04 Au M 78.65 Hg M 9.20 Totals 100.00

Element	Weight%
C K	7.40
O K	1.84
Cl K	0.15
Cu K	2.72
Sn L	0.04
Au M	78.65
Hg M	9.20
Totals	100.00

Element	Weight%
C K	6.00
Cl K	0.17
Cu K	1.87
Au M	82.09
Hg M	9.87
Totals	100.00

Element	Weight%
C K	7.43
O K	1.63
Cl K	0.07
Cu K	1.20
Sn L	0.05
Au M	80.12
Hg M	9.50
Totals	100.00

Element	Weight%
C K	6.81
Cl K	0.23
Cu K	1.26
Sn L	0.31
Au M	81.99
Hg M	9.39
Totals	100.00

Element	Weight% Spectrum 1	Weight% Spectrum 2	Weight% Spectrum 3	Weight% Spectrum 4	Weight% Spectrum 5
C K	3.30	5.32	1.53	6.21	8.32
O K			32.41		3.27
Mg K			0.42		
Al K			3.32		
Si K			4.46		
Cl K			0.01	0.14	0.16
Cu K	4.40	0.03	3.57	6.08	3.97
Sn L					0.39
Au M	82.06	80.37	47.07	78.08	74.56
Hg M	10.10	10.57	7.18	9.49	9.33
Totals	100.00	100.00	100.00	100.00	100.00

124

Samples uncoated: 10d TOW- ageing		
sample	Site of interest	elements: Weight%

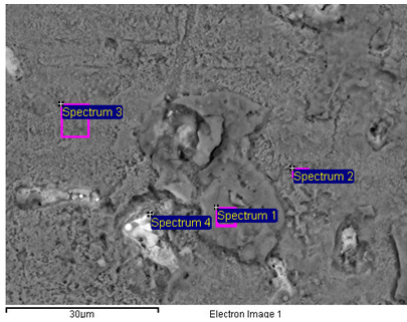| Element	Weight% Spectrum 1	Weight% Spectrum 2	Weight% Spectrum 3
C K	11.64		
O K	16.98		
Cl K	0.23		
Ca K	0.18		
Cu K	59.18	5.64	93.57
Sn L	8.67		3.35
Sb L	2.03		0.55
Pb M	1.08		
Zn K			2.52
Au M		80.55	
Hg M		13.81	
Totals	100.00	100.00	100.00
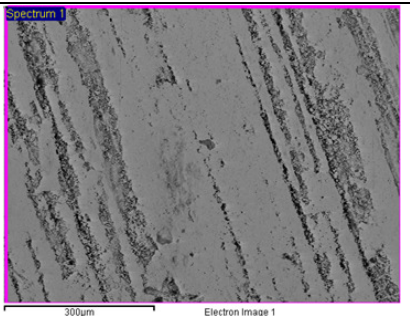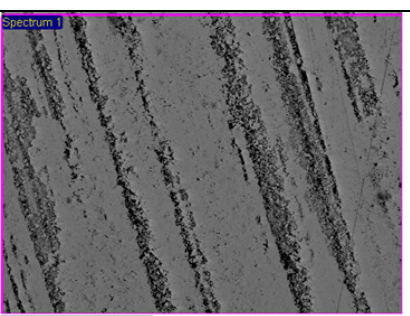
Uncoated

Samples coated with PropS-SH: 0d TOW-before cycle of ageing		
sample	**Site of interest**	**elements: Weight%**
PropS-SH		Element — Weight% C K — 11.04 N K — 3.31 O K — 8.87 Si K — 1.27 S K — 1.70 Cu K — 2.15 Au M — 63.65 Hg M — 8.00 Totals — 100.00
		Element — Weight% C K — 11.41 O K — 9.42 Si K — 1.40 S K — 1.82 Cu K — 1.81 Au M — 66.29 Hg M — 7.85 Totals — 100.00
		Element — Weight% C K — 11.77 O K — 11.95 Si K — 2.18 S K — 3.43 Cu K — 2.02 Au M — 61.00 Hg M — 7.66 Totals — 100.00

Site 1:

Element	Weight%
C K	11.04
N K	3.31
O K	8.87
Si K	1.27
S K	1.70
Cu K	2.15
Au M	63.65
Hg M	8.00
Totals	100.00

Site 2:

Element	Weight%
C K	11.41
O K	9.42
Si K	1.40
S K	1.82
Cu K	1.81
Au M	66.29
Hg M	7.85
Totals	100.00

Site 3:

Element	Weight%
C K	11.77
O K	11.95
Si K	2.18
S K	3.43
Cu K	2.02
Au M	61.00
Hg M	7.66
Totals	100.00

Site 4:

Element	Weight% Spectrum 1	Weight% Spectrum 2
C K	8.11	13.35
O K	5.06	14.00
Si K		2.78
S K		3.53
Cu K	7.84	3.49
Au M	69.18	55.13
Hg M	9.82	7.73
Totals	100.00	100.00

Site 5:

Element	Weight% Spectrum 1	Weight% Spectrum 2
C K	10.20	17.45
O K	5.98	14.23
Si K		2.91
S K		4.81
K K		0.23
Cu K	5.12	2.86
Au M	67.74	51.25
Hg M	10.96	6.27
Totals	100.00	100.00

Samples coated with PropS-SH:10d TOW- ageing		
sample	Site of interest	elements: Weight%

Element	Weight%
C K	12.82
O K	7.98
Si K	1.17
S K	1.48
Cl K	0.13
Cu K	1.71
Au M	65.99
Hg M	8.71
Totals	100.00

Element	Weight%
C K	10.96
O K	8.59
Si K	1.19
S K	1.25
Cl K	0.21
Cu K	2.36
Au M	66.24
Hg M	9.20
Totals	100.00

PropS-SH

Element	Weight%
C K	15.51
O K	12.85
Si K	3.31
S K	5.61
Cl K	0.02
Cu K	2.53
Au M	53.83
Hg M	6.34
Totals	100.00

Element	Weight% Spectrum 1	Weight% Spectrum 2	Weight% Spectrum 3
C K		14.82	26.70
O K	13.95	12.34	21.83
Si K	13.87	2.17	16.55
S K	24.41	3.17	22.03
Cl K	0.10	0.00	0.04
Cu K	1.67	1.75	0.95
Au M	41.62	58.68	11.90
Hg M	4.39	7.08	
Totals	100.00	100.00	100.00

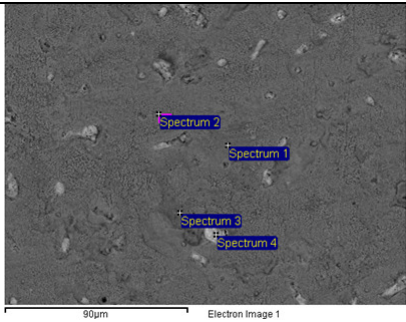| Element	Weight%
C K	6.25
O K	12.90
Cu K	72.17
Zn K	1.43
Sn L	4.97
Sb L	1.09
Pb M	1.18
Totals	100.00

127

Samples coated with PropS-SH:10d TOW- ageing		
sample	Site of interest	elements: Weight%

Element	Weight% Spectrum 1	Weight% Spectrum 2
C K	3.94	
O K	16.46	8.02
Cl K	0.17	0.00
Cu K	73.43	86.81
Sn L	4.63	4.08
Sb L	1.38	1.08
Totals	100.00	100.00

Element	Weight% Spectrum 1	Weight% Spectrum 2
C K	4.67	6.12
O K	13.54	17.96
Cl K	0.30	
Cu K	60.24	58.84
Zn K	1.89	2.02
Sn L	6.19	6.56
Sb L	1.15	1.74
Pb M	12.02	6.77
Totals	100.00	100.00
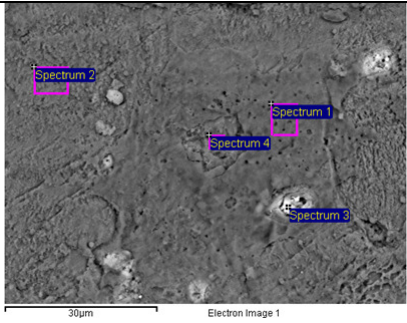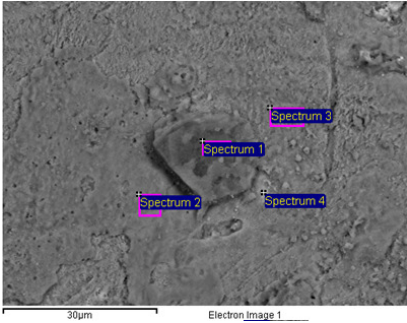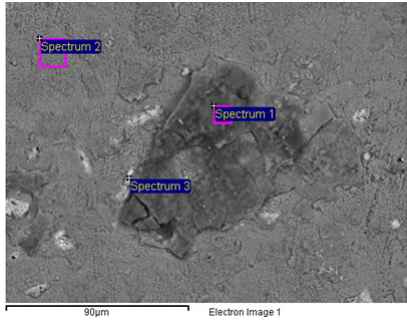
Sample: PropS-SH

Samples coated with PropS-SH+CeO$_2$: 0d TOW-before cycle of ageing		
sample	Site of interest	elements: Weight%

Element	Weight%
C K	9.35
O K	6.83
Si K	0.71
Cu K	3.04
Ce L	0.14
Au M	72.26
Hg M	7.66
Totals	100.00

Element	Weight%
C K	10.32
O K	9.91
Si K	1.12
Cu K	3.39
Ce L	0.26
Au M	67.55
Hg M	7.44
Totals	100.00

Sample: PropS-SH + CeO$_2$

Samples coated with PropS-SH+CeO₂: 0d TOW-before cycle of ageing		
sample	Site of interest	elements: Weight%

PropS-SH + CeO₂

Element	Weight%
C K	10.81
O K	9.86
Si K	1.12
Cu K	1.14
Ce L	0.29
Au M	69.72
Hg M	7.06
Totals	100.00

Element	Weight% Spectrum 1	Weight% Spectrum 2
C K	6.72	18.35
O K	3.04	14.03
Si K		2.05
K K		0.36
Cu K	5.33	2.86
Ce L	0.17	0.07
Au M	76.45	53.57
Hg M	8.30	8.72
Totals	100.00	100.00
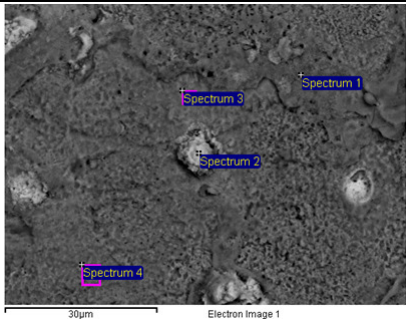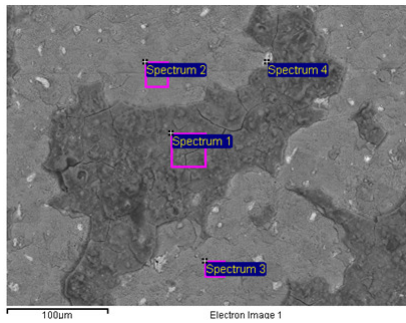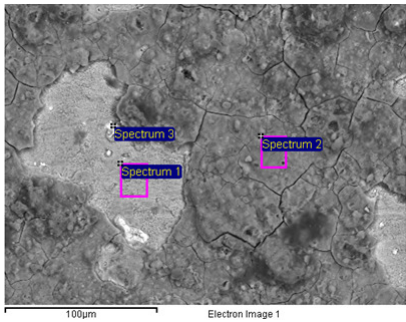
Samples coated with PropS-SH+CeO₂: 10d TOW- ageing		
sample	Site of interest	elements: Weight%

PropS-SH + CeO₂

Element	Weight%
O K	8.78
Si K	1.22
S K	1.41
Cl K	0.13
Cu K	4.08
Ce L	0.20
Au M	77.49
Hg M	6.68
Totals	100.00

Element	Weight%
C K	12.03
O K	7.29
Si K	0.91
S K	0.79
Cl K	0.12
Cu K	2.62
Sn L	0.32
Au M	69.04
Hg M	6.88
Totals	100.00

Samples coated with PropS-SH+CeO₂: 10d TOW- ageing		
sample	Site of interest	elements: Weight%

sample	Site of interest	elements: Weight%
PropS-SH + CeO₂		**Element — Weight%** O K — 9.41 Si K — 1.47 S K — 1.71 Cl K — 0.17 Cu K — 1.99 Sn L — 0.06 Ce L — 0.36 Au M — 77.86 Hg M — 6.96 Totals — 100.00
		Element — Weight% C K — 35.38 O K — 6.49 Cu K — 19.85 Sn L — 1.33 Sb L — 1.17 Hg M — 7.70 Pb M — 28.07 Totals — 100.00
		Element — Weight% C K — 13.88 O K — 20.14 Cl K — 0.25 Cu K — 45.83 Sn L — 16.18 Sb L — 3.73 Totals — 100.00

Element	Weight%	Weight%	Weight%	Weight%
C K	5.59		7.19	48.80
O K	18.83			23.95
Si K				2.51
S K				3.41
Cl K	0.39			
Cu K	60.13	91.57	3.90	2.58
Zn K		2.28		
Sn L	10.67	4.98		
Sb L	2.70	1.16		
Pb M	1.68			
Au M			76.66	18.74
Hg M			12.25	
Totals	100.00	100.00	100.00	100.00
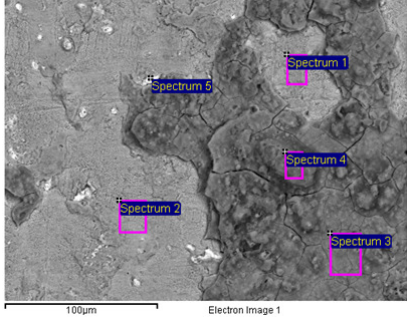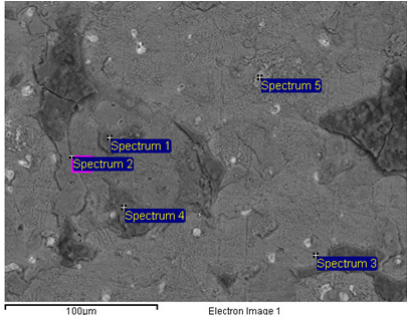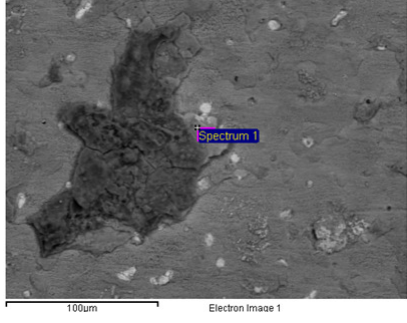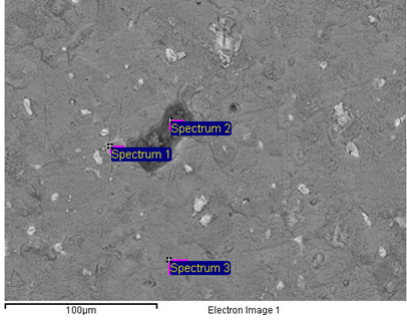
SEM-EDS analysis of samples from the laser treatment (section 3):

area	Site of interest	elements: Weight%			
		Laser treatment: post laser			

Area 1

Element	Weight% Spectrum 1	Weight% Spectrum 2	Weight% Spectrum 3	Weight% Spectrum 4
C K	4.59	4.58	4.79	
O K	22.95	2.81	3.93	4.66
P K	0.42			
S K	0.45			
Cl K	1.18	0.37		5.29
Ni K	0.96	0.78	0.48	
Cu K	41.15	84.58	84.55	14.43
Zn K	3.75	3.38	3.18	
Sn L	17.34	3.51	3.07	
Pb M	7.21			75.62
Totals	100.00	100.00	100.00	100.00

Area 2

Element	Weight% Spectrum 1	Weight% Spectrum 2	Weight% Spectrum 3	Weight% Spectrum 4
C K	4.30	4.10	5.83	3.24
O K	12.27	4.95	9.58	5.47
Cl K	1.16		1.66	0.84
Ni K	0.51	0.77		0.61
Cu K	77.31	84.67	9.14	84.39
Zn K	2.05	2.99		3.10
Sn L	2.40	2.53		2.34
Pb M			73.79	
Totals	100.00	100.00	100.00	100.00

Element	Weight% Spectrum 1	Weight% Spectrum 2	Weight% Spectrum 3	Weight% Spectrum 4
C K		3.89	3.78	4.46
O K	20.09	13.97	9.80	13.24
Si K	4.73			
S K	3.94			
Cl K	2.08	0.96	1.19	
Ni K	0.46	0.58	0.59	
Cu K	64.17	71.47	79.32	48.82
Zn K		1.89	2.61	1.36
Sn L	4.54	5.65	2.71	7.78
Pb M		1.59		23.94
P K				0.41
Totals	100.00	100.00	100.00	100.00

Area 3

Element	Weight% Spectrum 1	Weight% Spectrum 2	Weight% Spectrum 3
C K		6.18	
O K	35.01	6.50	2.97
Mg K	1.13		
Al K	2.37		
Si K	8.41		
S K	2.48		
Cl K	10.81	0.71	17.49
K K	1.56		
Ca K	1.47		
Cu K	33.33	80.66	30.12
Zn K		2.57	1.37
Sn L		2.71	
Pb M	3.43		48.05
Ni K		0.67	
Totals	100.00	100.00	100.00
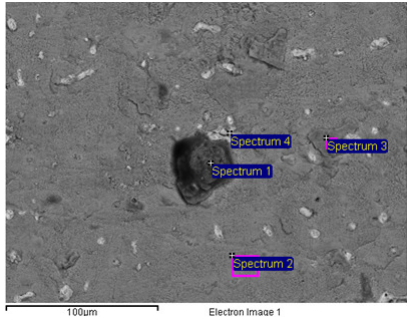
		Laser treatment: post laser			
area	Site of interest	elements: Weight%			

Area 4 (top image)

Element	Weight% Spectrum 1	Weight% Spectrum 2	Weight% Spectrum 3	Weight% Spectrum 4
C K	14.47	6.43		
O K	7.86	4.22	10.96	4.32
Cl K	0.76	0.78	10.44	13.01
Ni K	0.63	0.80	0.71	
Cu K	72.29	82.35	72.78	12.09
Zn K	2.13	2.80	2.45	
Sn L	1.86	2.62	2.66	
Pb M				70.58
Totals	100.00	100.00	100.00	100.00

Area 4 (bottom image)

Element	Weight% Spectrum 1	Weight% Spectrum 2	Weight% Spectrum 3	Weight% Spectrum 4
C K	3.60	12.87	4.02	3.38
O K	17.05	6.38	9.28	8.77
Cl K	1.48	14.44	0.32	0.52
Ni K	0.44		0.51	0.66
Cu K	66.65	12.41	77.00	77.72
Zn K	2.05		2.93	2.32
Sn L	6.30		5.93	6.64
Pb M	2.43	53.89		
Totals	100.00	100.00	100.00	100.00

Area 5

Element	Weight% Spectrum 1	Weight% Spectrum 2	Weight% Spectrum 3	Weight% Spectrum 4
C K		3.85	5.22	6.19
O K	24.36	10.70	4.75	9.38
Mg K	0.72			
Si K	3.16			
S K	1.88			
Cl K	7.54	1.24		11.56
Ca K	0.65			
Ni K	0.46	0.81	0.91	
Cu K	56.48	76.66	80.78	15.68
Zn K		2.69	2.69	1.46
Sn L		4.04	5.65	
Pb M	4.76			55.73
Totals	100.00	100.00	100.00	100.00

Area 6

Element	Weight% Spectrum 1	Weight% Spectrum 2	Weight% Spectrum 3
C K	6.00	10.36	
O K	5.71	26.45	6.46
Si K		1.89	
S K		1.29	6.29
Cl K	0.85	7.47	9.88
Ca K		0.28	
Ni K	0.69	0.40	
Cu K	80.06	44.20	23.31
Zn K	2.68	1.17	11.77
Sn L	2.95	0.62	
Pb M	1.06	5.87	42.28
Totals	100.00	100.00	100.00

	Laser treatment: post laser					
area	Site of interest	elements: Weight%				

Area 6

Element	Weight% Spectrum 1	Weight% Spectrum 2	Weight% Spectrum 3	Weight% Spectrum 4	Weight% Spectrum 5
C K	6.55	4.07			12.21
O K	15.00	7.86	26.74	37.33	13.61
Mg K				0.64	
Al K			0.68	0.47	
Si K			3.39	4.76	
S K			1.68	2.06	
Cl K	1.40	0.59	4.69	9.71	11.44
K K				0.71	
Ca K			0.49	5.57	
Ni K	0.45	0.63	0.46		0.54
Cu K	66.04	79.60	54.30	31.32	21.32
Zn K	2.14	2.78	1.42	1.64	0.98
Sn L	5.58	4.47	1.61		1.17
Pb M	2.84		4.56	5.80	38.72
Totals	100.00	100.00	100.00	100.00	100.00

Area 7

Element	Weight% Spectrum 1	Weight% Spectrum 2	Weight% Spectrum 3	Weight% Spectrum 4	Weight% Spectrum 5
C K		5.55	3.81	3.60	3.37
O K	22.98	23.93	6.40	23.16	7.93
Si K				0.33	
S K	0.68	0.60		0.74	
Cl K	5.90	4.06	0.33	4.31	3.56
Ni K	0.62	0.54	0.67	0.75	0.52
Cu K	57.93	56.17	82.61	56.21	66.24
Zn K	2.72	1.81	2.75	2.72	2.65
Sn L	5.98	4.66	3.44	5.75	3.94
Pb M	3.19	2.68		2.43	11.78
Totals	100.00	100.00	100.00	100.00	100.00

Element	Weight%
C K	6.57
O K	19.10
Cl K	2.66
Cu K	60.36
Zn K	1.71
Sn L	5.14
Pb M	4.45
Totals	100.00

Area 8

Element	Weight% Spectrum 1	Weight% Spectrum 2	Weight% Spectrum 3
C K	13.14		5.61
O K	15.88	37.40	2.94
Mg K		0.84	
Si K		1.05	
S K		2.35	
Cl K	9.90	4.24	0.80
K K		0.56	
Ca K		0.53	
Fe K		27.03	
Cu K	28.54	20.17	82.75
Zn K		1.78	2.56
Sn L	2.45		4.52
Pb M	30.10	4.04	
Ni K			0.81
Totals	100.00	100.00	100.00
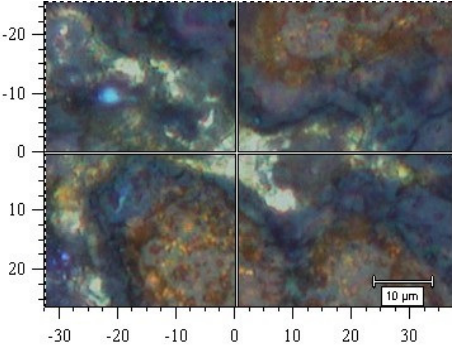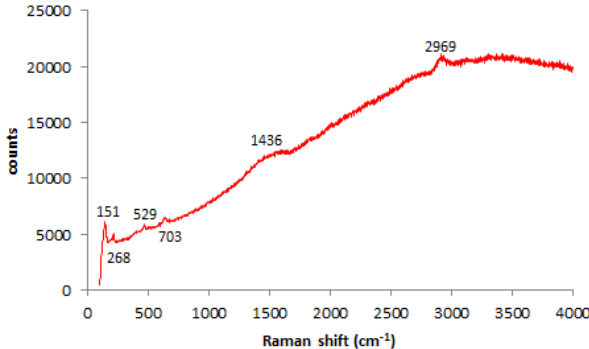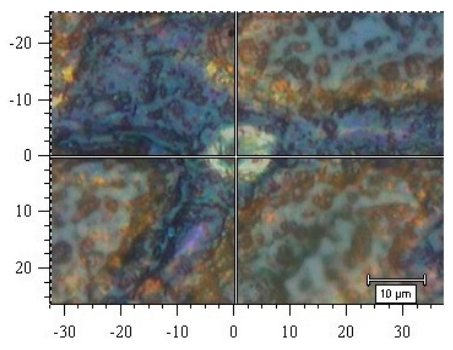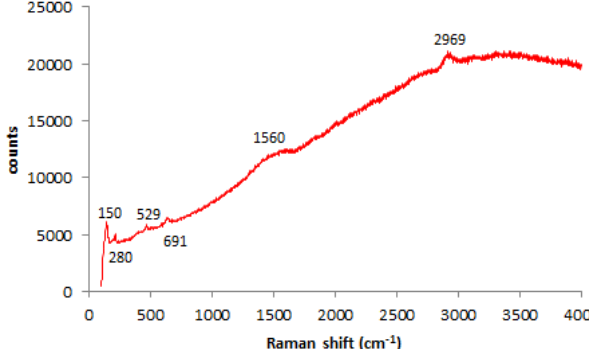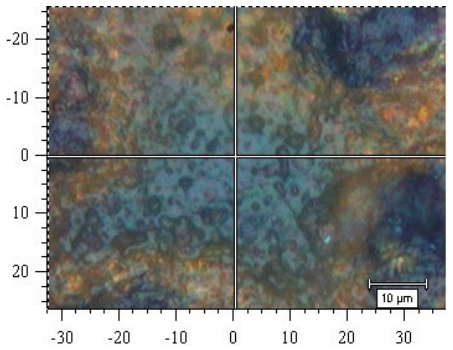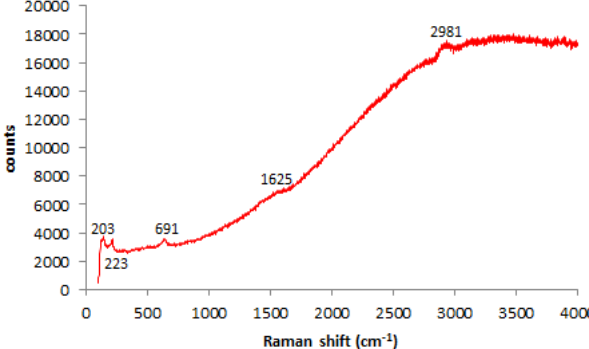
Laser treatment: post laser					
area	Site of interest	elements: Weight%			
8		Element	Weight% Spectrum 1	Weight% Spectrum 2	Weight% Spectrum 3	Weight% Spectrum 4
		C K		4.57		
		O K	35.75	5.64	16.47	10.91
		Si K	0.88			
		S K	1.89		0.48	
		Cl K	11.46	0.29	2.76	17.09
		K K	0.45			
		Ca K	0.68			0.40
		Ni K	0.60	0.88		
		Cu K	39.92	80.61	78.28	19.46
		Zn K	2.03	3.20		
		Sn L			2.00	2.33
		Pb M	6.35	4.81		49.81
		Totals	100.00	100.00	100.00	100.00

Appendices C   µ-Raman analysis

µ-Raman analysis of dropping test samples (section 1) after ageing (10d TOW)

Sample name	Picture of the area	Raman spectrum + compound name
E + TiO$_2$		Cuprite + PropS-SH
E + TiO$_2$		Cuprite + PropS-SH
G + CeO2		Cuprite + PropS-SH

Appendices D   XRD analysis

XRD analyses of dropping test samples (section 1) after ageing (10d TOW)